In–situ study of Real time Structural Evolution during Polymer/Fullerene Bulk Heterojunction Thin Film Formation

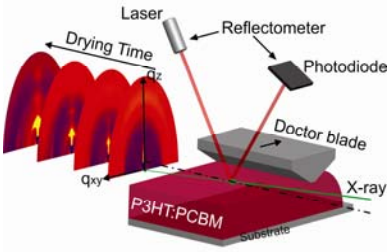

Monamie Sanyal

Stuttgart, 2011

MAX-PLANCK-GESELLSCHAFT

Max Planck Institut für Metallforschung, Stuttgart, Germany

Institut für Theoretische und Angewandte Physik der Universität Stuttgart, Germany

In–situ study of Real Time Structural Evolution during Polymer/Fullerene Bulk Heterojunction Thin Film Formation

Von der Fakultät Mathematik und Physik der Universität Stuttgart
zur Erlangung der Würde eines Doktors der Naturwissenschaften
(Dr. rer. nat.) genehmigte Abhandlung

Vorgelegt von

Monamie Sanyal

aus Bombay (India)

Hauptberichter: Prof. Dr. Helmut Dosch

Mitberichter: Prof. Dr. Jörg Wrachtrup

Tag der mündlichen Prüfung: 8 April 2011

Institut für Theoretische und Angewandte Physik
der Universität Stuttgart
Max-Planck-Institut für Metallforschung

Stuttgart 2011

You only control your Action
and not the Results;
So be not motivated
by Results,
nor be attached to
Inaction.

Bhagavad Gita 2:47

Contents

CHAPTER 1

Deutsche Zusammenfassung

1.1 Warum sind Polymersolarzellen so bedeutend?

Photovoltaik ist eine schnell wachsende Technologie, der eine grosse Rolle im Bereich der erneuerbaren Energien zukommt [1]. Mit wachsenden Kosten fossiler Rohstoffe und zunehmenden Bedenken gegenüber Treibhausgas Emission, die zur irreversiblen Klimaveränderung führen, stellen erneuerbare Energien, insbesondere solar Energie, das weltweite Hauptinteresse dar [2]. Ende 2009 lag der jährliche weltweite Öl Konsum bei 3882.1 Millionen Tonnen, 2653.1 Millionen Tonnen Öläquivalent Erdgas und 3278.3 Millionen Tonnen Öläquivalent Kohle und einem Gesamtäquivalent fossiler Energieträger von 11164.3 Millionen Tonnen Öl, was etwa 4.675×10^{16} J an Primärenergiebedarfs ergibt. [1]Die gesamte auf der Erde verfügbare Solarenergie beträgt jährlich näherungsweise 3.85×10^{24} J. Bei ausreichender Nutzung dieser Energie Resource könnte der Weltenergiebedarf gedeckt werden. Zurzeit basiert der Grossteil kommerziell erhältlicher Solarmodule auf kristallinem Silizium, was in einem kosten– und energieintensiven Verfahren hergestellt wird [3, 4]. Hingegen zeigen sog. organische "bulk–heterojunction" Solarzellen grosses Potential zur kostengünstigen Nutzung solarer Energie [5]. Dabei werden lösliche, organische Halbleiter verwendet, die grossflächig, in sogenannten Rolle–zu–Rolle Beschichtungsverfahren, kostengünstig hergestellt werden können [6–9]. Dabei werden energieaufwändige Hochtemperatur– und Vakuumschritte vermieden. In dieser Arbeit werden flüssig prozessierbare organische Solarzellen basierend auf Polymer/Fulleren Schichten als photoaktive Schicht behandelt. Polymersolarzellen haben nicht nur ein grosses Potential zur kostengünstigen Herstellung von Solarzellen, sondern sind auch sehr dünn ($< 1\mu$m), besitzen damit ein sehr geringes Gewicht und sind mechanisch flexibel. Die dabei verwendeten konjugierten Polymere und Fullerene sind vergleichsweise günstig in der Herstellung, haben einen

[1]Statistical Review of World Energy 2010 by British Petroleum

hohen Absorptionskoeffizienten und lassen sich grossflächig als Lösung bei Umgebungsdruck und nahe Raumtemperatur auf Kunststoffsubstraten beschichten. Dies stellt einen grossen Vorteil gegenüber der Wafer basierten Herstellung von Silizium Photovoltaik dar. Die höchsten, publizierten Effizienzen von Polymersolarzellen liegen bei etwa 7% [10–12], wobei bereits 8.13% von NREL zertifiziert wurden. Demzufolge stellt nicht nur die kostengünstige Produktion sondern auch die starke Leistungssteigerung die Bedeutung dieser Technologie in Ergänzung zu etablierten anorganischen Solarzellen dar.

1.2 Struktur von P3HT: PCBM — ein etabliertes fotoaktives Stoffsystem

Das gängigste fotoaktive Stoffsystem in einer Polymer/Fulleren bulk–heterojunction Solarzelle besteht aus einem konjugiertem, p–halbleitenden und Elektronen liefernden (Donor) Polymer, wie zum Beispiel poly–(3–hexylthiophene) (P3HT) und einem n–halbleitenden, Elektronen aufnehmenden (Akzeptor) Fulleren Derivat, wie zum Beispiel [6,6]–phenyl–C_{61}–butyric–acid–methyl–ester (PCBM). Diese beiden organischen Materialien sind von zwei unterschiedlichen Elektroden eingeschlossen, von denen eine transparent für Sonnenlicht und elektrisch leitend ist, wie zum Beispiel das Metalloxid Indium Zinn Oxid (ITO). Dadurch können die eingestrahlten Photonen die aktive Schicht der Solarzelle erreichen und dort absorbiert werden. Um die Energieniveaus an der Grenzfläche zwischen Elektrode und aktiver Schicht zu optimieren, wird dort ein transparente, lochleitende Polymerschicht eingebracht, wie zum Beispiel poly–(styrenesulfonate) dotiertes poly–(3,4–ethylenedioxythiophene) (PEDOT: PSS). PEDOT: PSS verstärkt die lichtinduzierte Lochextraktion an der Anodengrenzfläche und glättet die Oberfläche der rauen ITO Schicht. In der Regel werden Metalle, wie Aluminium, Gold, Silber, Kalzium, Barium und Magnesium als Kathodenmaterialien und sehr dünne Metallhalogenide, wie Lithiumfluorid als kathodisches Grenzflächenmaterial verwendet. Die direkte Mischung des Donor und Akzeptor Materials, bereits in Lösung vor der Beschichtung, führt zur Bildung eines feinen interpenetrierenden Netzwerkes der sog. bulk–heterojunction der fertigen Schicht. In dieser Dissertation wurde die Nanomorphologie des Stoffsystems P3HT und PCBM mit einem für dieses System üblichen Lösungsmittel 1,2–Dichlorbenzol (DCB) während des Trocknungsvorgangs in–situ mittels Röntgenstreuung untersucht (Figure 1.1). Bislang existiert nur empirisches Wissen über den Zusammenhang zwischen der Leistung einer Solarzelle und den Prozessparametern für die Herstellung der fotoaktiven Schicht. In dieser Arbeit wurde der Einfluss verschiedener Prozessparameter, wie die Trocknungstem-

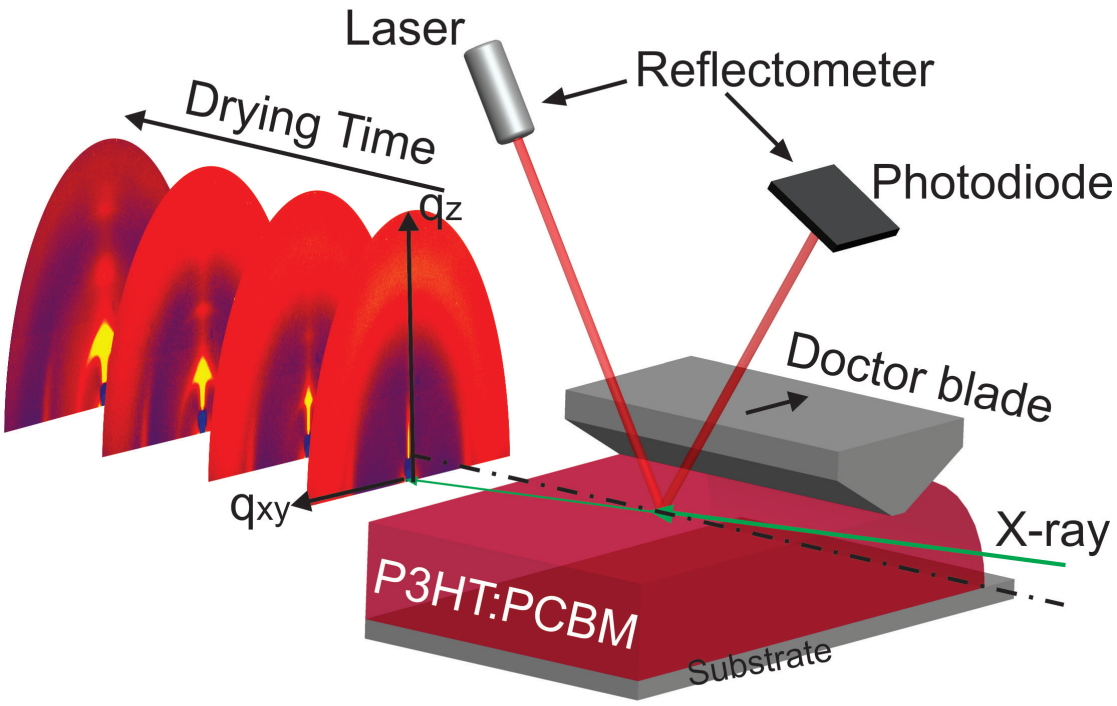

Figure 1.1: (a) Schematische Darstellung des experimentellen Aufbaus der in–situ Trocknungs–Untersuchung von P3HT: PCBM Schichten mittels Röntgenbeugung im streifenden Einfall und Laser–Reflektometrie.

peratur, das Donor–Akzeptor–Verhältnis, die Verwendung von Lösemittelgemischen und Additiven auf die Strukturbildung von P3HT: PCBM–Schichten untersucht. Dazu konnte unmittelbar nach dem Beschichtungsvorgang die Entstehung der Filmstruktur und – morphologie während der Lösungsmittelverdunstung in Echtzeit mittels in–situ Röntgenbeugung verfolgt werden, was die fundamentale Neuigkeit dieser Arbeit ist.

1.3 Zusammenfassung der Ergebnisse

Echtzeit Untersuchungen mittels Röntgenbeugung an P3HT: PCBM Schichten während der Trocknung dünner Schichten lieferten neuartige Einblicke in die Kristallisation und der damit verbundenen elastischen Eigenschaften des Films während der Film Formation. Die Mikrostruktur des Gemisches durchläuft einen flüssig kristallinen, smektischen Zustand während der Trocknung. Das Kompressionsmodul und die Biegesteifigkeit des Films wurden für verschiedene Zeitpunkte des Trocknungsvorgangs aus der Analyse diffuser Röntgenstreuung bestimmt. Dies ermöglichte erstmalig die direkte Bestimmung der Materialeigenschaften des Gemisches während der Trocknung. Diese Entdeckung eröffnet Möglichkeiten ein mikroskopisches Verständnis der nanoskali-

gen Anordnung von Polymer/Fulleren Schichten in "bulk–heterojunction" Solarzellen zu schaffen. In dem Zusammenhang wurde der Einfluss der Phasengleichgewichte und des Trocknungsverhaltens auf die Selbstanordnung untersucht, was eine Schlüsselrolle in der Kontrolle der nanoskaligen Struktur optimierter Solarzellen einnimmt. Die Trocknungstemperatur wurde dabei als einflussreiche Grösse für die Strukturbildung während dem Übergang vom nassen zum festen Film in gerakelten P3HT: PCBM Schichten ermittelt. Die Trocknung der fotoaktiven P3HT: PCBM Schicht bei niedrigen Temperaturen, wie zum Beispiel 10°C, zeigte eine vermehrte π–π Stapelung der P3HT Ketten, sowie eine verbreiterte Verteilung der Orientierung der P3HT Kristallite bedingt durch eine langsame Kristallisationskinetik und eine unterdrückte Phasenseparation zwischen P3HT und PCBM aufgrund der erhöhten Viskosität und geringerer molekularer Mobilität. Insgesamt führte dies zu einer leistungsstärkeren Nanomorphologie mit einem feineren, interpenetrierenden Netzwerk. Obwohl bereits zuvor eine gesteigerte Effizienz aufgrund niedrigerer Trocknungstemperatur auf empirische Weise beobachtet wurde, waren die Morphologie und die Mechanismen, die zu einer gesteigerten Effizienz führten, noch ungeklärt. Die in dieser Arbeit durchgeführten Untersuchungen belegen, dass das Absenken der Temperatur während der Beschichtung und Trocknung eine einfache Methode zur Optimierung der Effizienz gerakelter Polymersolarzellen darstellt.

Das Mischungsverhältnis von P3HT: PCBM ist essenziell für die Leistungsfähigkeit organischer Solarzellen. Die Strukturbildung von P3HT: PCBM Schichten wurde in Abhängigkeit vom Mischungsverhältnis der beiden Komponenten in–situ untersucht und zeigte ebenfalls eine starke Abhängigkeit vom Donor–Akzeptor–Verhältnis. Es konnte in dieser Arbeit gezeigt werden, dass die Mosaizität (Mass für die Verkippung der Kristallite) von P3HT mit steigendem Anteil PCBM abnimmt. Das weist auf eine gleichmässigere Ausrichtung innerhalb der Faltungsebene (sog. interlayer stacking) des Polymers bei steigendem PCBM–Anteil hin. Dagegen verringert sich der Anteil an π–π gestapelten (sog. interchain stacking) Polymer Ketten mit zunehmendem PCBM–Anteil. Ausserdem konnte erstmalig die Bildung einer komplexen P3HT–PCBM Struktur gezeigt werden, die zuvor für andere Polymer/Fulleren Systeme beobachtet wurden.

Das in dieser Dissertation Überwiegend verwendete halogenierte Lösungsmittel DCB ist nicht für die grosstechnische Herstellung von organischer Photovoltaik geeignet. Allerdings zeigt DCB insgesamt sehr gute Eigenschaften, da die damit hergestellten Solarzellen die vergleichsweise höchste Leistungsfähigkeit aufweisen. Daher ist man auf der Suche nach einem alternativen Lösungsmittel, welches die gleiche Nanostruktur von P3HT: PCBM im Vergleich zu DCB erzeugt und gleichzeitig unbedenklich für

den grosstechnischen Einsatz ist. Unter diesem Aspekt ist das Lösemittel Indan und seine Mischung mit o–Xylol oder Toluol ein guter Ersatz für DCB. Erste Versuche, die am Holst Centre (Eindhoven, Niederlande) durchgeführt wurden, ergaben ähnlich effiziente Solarzellen für die weniger gesundheitsschädlichen Lösemittelgemische im Vergleich zu DCB. In dieser Arbeit konnte gezeigt werden, dass die Auffaltung der P3HT Ketten (interchain stacking) normal zum Substrat und die π–π Stapelung (interlayer stacking) parallel zum Substrat vergleichbar gut ausgeprägt ist, wie zuvor für die mit DCB hergestellten P3HT: PCBM Schichten beobachtet wurde. Dies bestätigt die Ersetzbarkeit des idealen, aber gesundheitsschädlichen Lösemittels DCB und unterstützt die weitere Suche und Optimierung alternativer Lösemittel und Gemische für die umweltfreundliche, grosstechnische Herstellung organischer Photovoltaik.

Eine weitere Möglichkeit zur Beeinflussung der P3HT: PCBM Schichtstruktur ist die Zugabe des Additivs Oktandithiol, was für unterschiedliche Trocknungstemperaturen erstmalig in dieser Arbeit bearbeitet wurde. Dabei wurde der Zusammenhang zwischen dem kombinierten Einfluss der Temperatur und des Additivs auf die Schichtstruktur untersucht. Die Zugabe von Oktandithiol veränderte nicht die Struktur innerhalb der P3HT Faltungsebene entlang q_z Richtung senkrecht zur Substrat Ebene, im Vergleich zu den Strukturänderung durch den alleinigen Temperatureinfluss. Allerdings zeigte sich eine deutliche Verbesserung der P3HT π–π Stapelung innerhalb der P3HT: PCBM Schicht durch Verwendung des Additivs bei allen Temperaturen, was den Vorteil der Verwendung von Additiven verdeutlicht.

In all den im Rahmen dieser Dissertation durchgeführten Arbeiten, zeigte sich eine sehr sensible π–π Stapelung zwischen den P3HT Ketten entlang des Substrates. Diese ist von der Trocknungstemperatur, dem Mischungsverhältnis von P3HT und PCBM und der Art des verwendeten Lösungsmittels und der zusätzlichen Verwendung von Additiven abhängig. Andererseits ist die Anordnung der P3HT Ketten in [100] Richtung, senkrecht zur Substrat Oberfläche, vergleichsweise unbeeinflusst von den genannten Einflüssen. Die Kristallinität in diese Richtung bildet sich bereits in einer frühen Phase des Trocknungsprozesses aus und ist bei höheren Trocknungstemperaturen stärker ausgeprägt. Auch die Phasentrennung von P3HT und PCBM in deren Mischung begünstigt die Kristallinität dieser Richtung. Die Segregation des P3HT von PCBM bewirkt bei einer zu groβskaligen Phasenseparation einen Verlust der nanoskaligen Mischung und damit eine Verringerung des Wirkungsgrades der Solarzelle. Die Elastizität in [100] Richtung des P3HT senkrecht zum Substrat wurde hier nach den Konzepten diffuser Streuung flüssig kristalliner Phasen untersucht. Die Ergebnisse dieser Arbeit zeigen deutlich, dass während der Filmtrocknung die P3HT Kristallinität in [100] Richtung senkrecht zum Substrat zuerst gebildet wird, gefolgt von der zu einem späteren

Zeitpunkt ausgebildeten π–π Ordnung des P3HT parallel zum Substrat. Die P3HT: PCBM Schichten verhalten sich wie flüssig kristalline Schichten mit einer weitreichenden Ordnung senkrecht und keiner Ordnung parallel zum Substrat. Die P3HT Ordnung in π–π Richtung entlang des Substrates bildet sich in einer späten Phase der Trocknung, wobei der (020) Bragg Peak nur auftritt, sofern das Mischungsverhältnis von P3HT: PCBM und die Trocknungstemperatur entsprechend gewählt wurden. Weiterhin wurde in dieser Arbeit für P3HT: PCBM Schichten mit höherer Mosaizität des P3HT (100) Peaks und schärferem (020) Peak eine Rotverschiebung des Absorptionsspektrums mit stärker ausgeprägten vibratorischen Schultern bewirkt. Es konnte gezeigt werden, dass diese Schultern mit den P3HT π–π Wechselwirkungen zusammen hängt, deren stärkere Ausprägung zu effizienteren Solarzellen führt.

CHAPTER 2

Introduction to polymer solar cells

2.1 Why are polymer solar cells important ?

Photovoltaics is a fast growing technology playing an important role in renewable energy supply [1]. With increasing price of fossil fuels and concerns over vast amounts of green house gases emanating from them leading to irreversible global climate change, renewable energy sources, particularly solar energy, is of major interest to the world today [2]. At the end of 2009, the world consumed 3882.1 million tonnes of oil, 2653.1 million tonnes oil equivalent of natural gas and 3278.3 million tonnes oil equivalent of coal and a total of 11164.3 million tonnes oil equivalent of fossil fuels which generates about 4.675×10^{16} J of energy for primary consumption.[1] The total solar energy available to the earth is approximately 3.85×10^{24} J. So if harnessed properly, solar energy can be used to satisfy the energy needs of mankind. Presently, much of the commercial solar energy is based on crystalline silicon, which is a very expensive technology [3, 4]. However, polymer solar cells based on bulk heterojunction technology, could make solar energy affordable, [5, 13–16] as it uses organic semiconductors, which are low–cost materials and roll–to–roll coating, which are low–cost manufacturing techniques — this aspect will be elaborated later on in the thesis.

2.2 Polymer solar cells — the future of organic solar cell industry

In this thesis, solution processed organic solar cells based on polymer/fullerene blend films have been discussed. Polymer solar cells have great potential as ultra–low cost devices [3, 4, 17, 18]. Figure 2.1 a shows a photograph of a typical polymer solar cell;

[1] Statistical Review of World Energy 2010 by British Petroleum

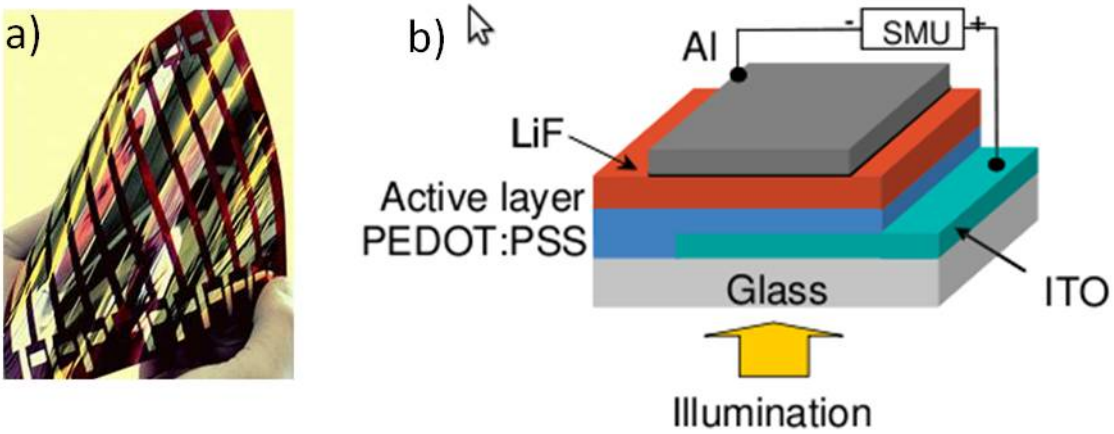

Figure 2.1: (a) Photo of a thin, light–weight, flexible polymer solar cell developed by Siemens AG (b) Schematic of a polymer solar cell indicating the various constituent layers within [19].

they are thin, light–weight and flexible. The materials used to manufacture polymer solar cells are conjugated polymers and fullerene–derivatives. They are cheap, have very high optical absorption coefficients, are compatible with plastic substrates and can be fabricated at low temperature using high throughput processes such as low cost roll–to–roll manufacturing unlike the more expensive wafer based production techniques associated with crystalline silicon. The best performing polymer solar cells have efficiency 7% [10–12]. This is an emerging technology which requires less capital investment than fabrication techniques for silicon based devices. Hence, polymer solar cells are unrivalled in terms of processing cost, processing speed, processing simplicity and thermal budget offering a convincing solution to the problem of high cost commonly encountered for photovoltaic technologies. A typical polymer/fullerene bulk heterojunction solar cell, consists of an electron–donating conjugated polymer such as poly–(3–hexylthiophene) (P3HT) as the donor and and a buckminsterfullerene derivative such as [6,6]– phenyl– C_{61}– butyric– acid– methyl– ester (PCBM) as the acceptor in the photoactive layer sandwiched between two different electrodes, one of which should be a transparent conducting oxide, such as indium tin oxide (ITO), in order to allow the incoming photons to reach the photoactive layer. In order to make an optimal interface between the organic photoactive layer and the electrodes, a thin transparent conducting polymer such as poly–(styrenesulfonate) doped poly–(3,4–ethylenedioxythiophene) (PEDOT:PSS) is coated as an interfacial layer on the adjacent ITO. PEDOT:PSS enhances the photoinduced hole–extraction on the anode interfacial layer and promotes planarization of the indium tin oxide surface. Generally metals such as aluminum, gold, silver, calcium, barium, magnesium are used as the cathode and very thin metal–halides such as lithium fluoride are used as cathodic interfacial materials. A schematic diagram of a polymer solar cell is shown in the Figure 2.1 b.

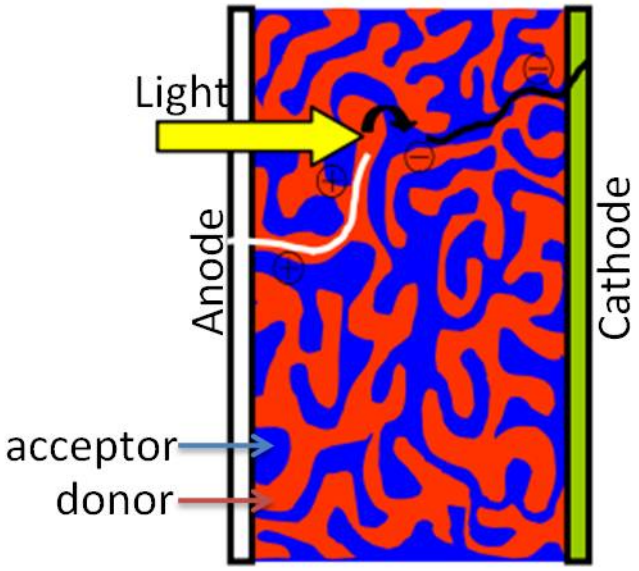

Figure 2.2: Schematic of the photoactive bulk heterojunction inside a polymer solar cell showing the formation and transport of charge carriers towards the respective electrodes when light is incident [19].

The intimate mixing of donor and acceptor materials leads to the formation of bulk heterojunction schematically shown in Figure 2.2. The nanostructure and nanomorphology of a bulk heterojunction will be discussed later in this chapter.

2.3 How do polymer solar cells work ?

In a polymer solar cell, the electron donor is an electron–rich, semiconducting polymer such as poly–(3,4 hexylthiophene) (P3HT) and the electron–acceptor is a electron–deficient, semiconducting fullerene–derivative such as [6,6]– phenyl– C_{61}– butyric– acid– methyl– ester (PCBM) processed from a common organic solvent such as 1,2–dichlorobenzene (DCB) [20] forming bulk heterojunction, shown in Figure 2.2, which involves intimate mixing of donor and acceptor materials leading to nanoscopic phase separation between them [17, 18, 21–23]. The π–electrons of the conjugated polymers used are delocalized within the polymer chain, and the overlap of these delocalized π–electrons between neighboring molecules (Figure 2.3) determine the transport properties of the polymer. The overlapping π–orbitals of double bonded carbon atoms provide a continuous path for electron transport along the polymer backbone. This overlapping of orbitals creates a degeneracy which leads to the formation of filled and unfilled bands called the highest occupied molecular orbitals (HOMO) and the lowest unoccupied molecular orbitals (LUMO). In the case of a large number of electrons, the HOMO and LUMO levels broaden into continuous bands, with the HOMO/LUMO en-

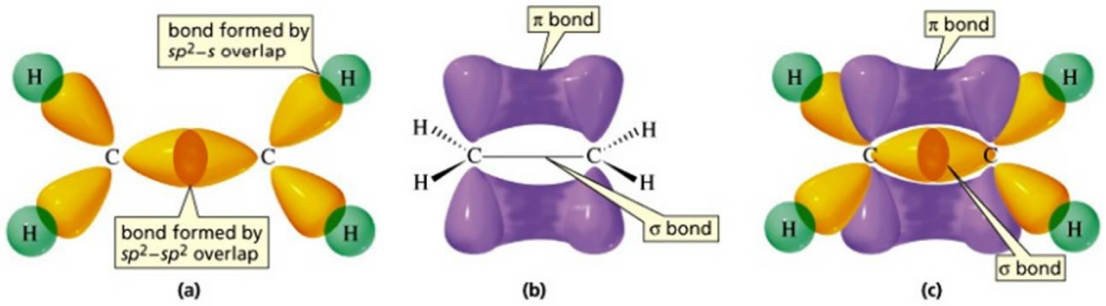

Figure 2.3: Orbital structure of conjugated sp^2 hybridized carbon atoms in ethene [24]. (a) Overlapping of σ orbitals (b) Overlapping and delocalization of π orbitals (c) Complete orbital structure.

ergy gap becoming analogous to the valence/conduction band gap of inorganic semiconductor materials. These filled and unfilled bands result in organic materials behaving as semiconductors. The donor and acceptor materials in a polymer solar cell have different electron affinity i.e. different LUMO levels and are sandwiched between two metal electrodes. The material with highest LUMO level is called donor and the semiconductor with the highest electron affinity is called the acceptor.

Upon absorption of light, the photoactive polymer/fullerene blend produces a neutral mobile excited state called exciton in the polymer. Since the binding energy of this exciton is typically 0.2 to 0.8 eV, which is much higher than the thermal energy at room temperature [25–27], excitons can dissociate into free charge carriers at the donor/acceptor interface to escape from their Coulomb attraction [28]. When an exciton reaches the donor/acceptor interface, the electron will transfer to the material with the larger electron affinity and the hole will be accepted by the material with the lower ionization potential. Due to the low exciton diffusion lengths (1 nm to 10 nm) in polymeric materials [29–33], nanoscopic phase separation between the donor and acceptor materials in a bulk heterojunction ensures that every exciton can reach the interface where dissociation into free electrons and holes is possible. Percolating pathways facilitate hole and electron transport to corresponding electrodes. Charge separation occurs at the interface between conjugated polymers as a donor and fullerene (or its derivative) as an acceptor. Electron transport occurs through the fullerene derivatives and hole transport is along the conjugated polymer. Thus all absorbed photons in the vicinity of a donor/acceptor interface can contribute to the generated photocurrent. Due to the presence of a built–in electric field provided by the asymmetrical work functions of the electrodes, these charges are transported and collected by the external circuit. This process is schematically shown in the Figure 2.4 The complete process, enumerated below, starting from an absorbed photon and ending up with charges collected at the electrodes is depicted in the Figure 2.5

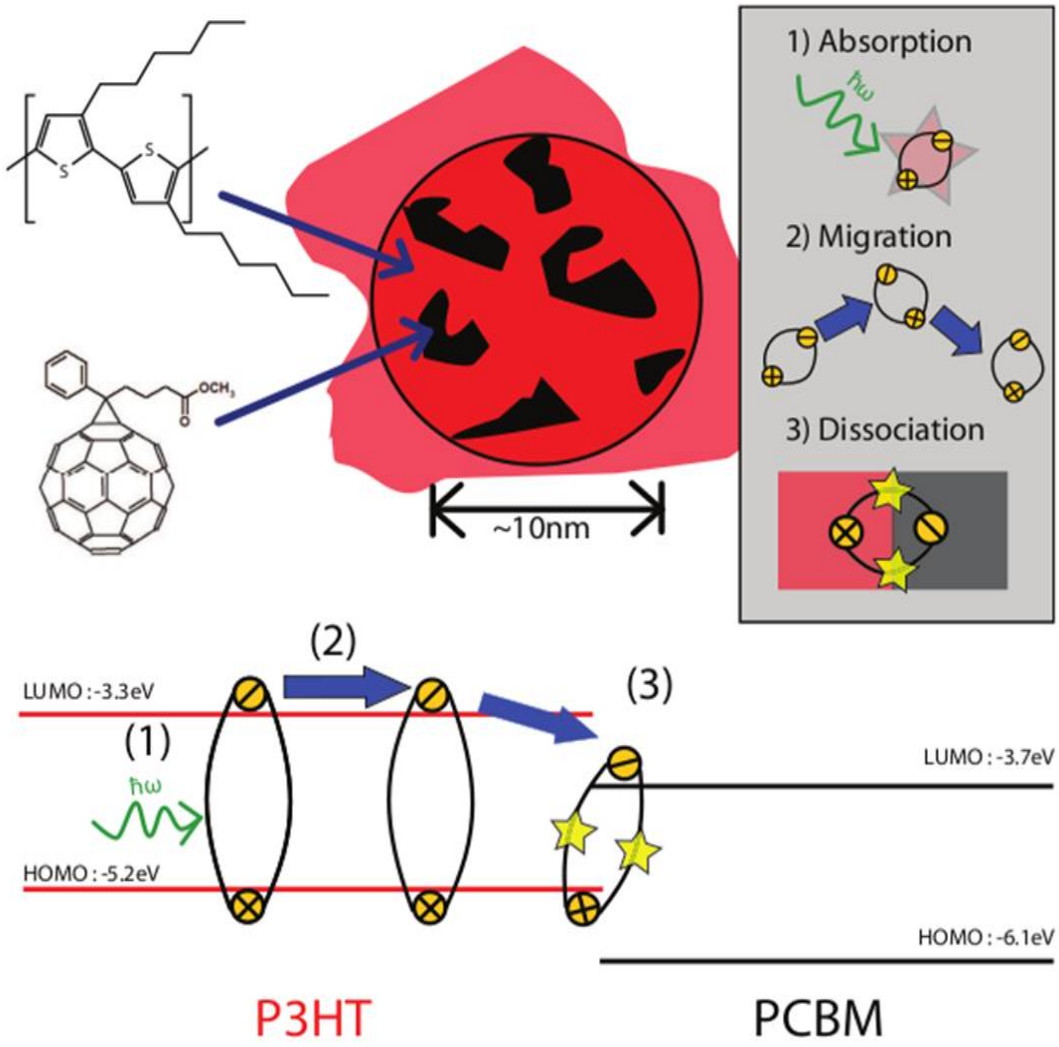

Figure 2.4: Schematic diagram of a bulk heterojunction assisted exciton dissociation. The electron–donor polymer P3HT and the electron acceptor PCBM is shown on the left. The charge generation is schematically shown on the right. A band–level diagram shows the energetic landscape in which heterojunction dissociation takes place [34].

(a) A photon is absorbed by the donor material after which an exciton is created.

(b) This exciton diffuses towards a donor/acceptor interface.

(c) At the donor/acceptor interface, the electron is transferred to the acceptor material. Even though the hole and electron are now on different materials they are still strongly bound by Coulomb interaction.

(d) The hole and electron need to be dissociated into free charge carriers.

(e) They are transported to the respective phases.

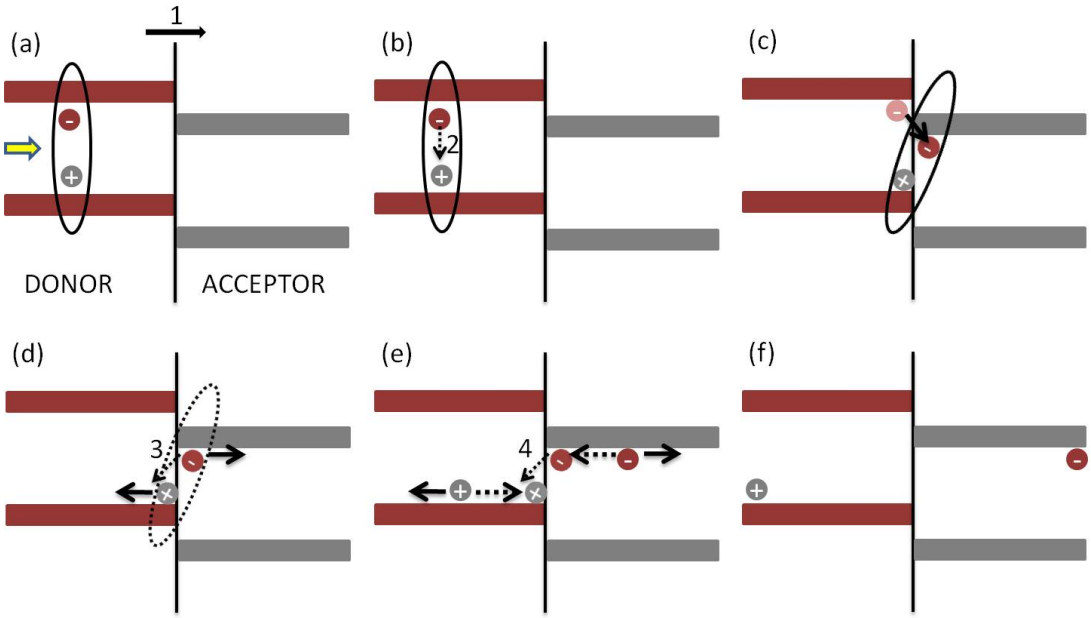

Figure 2.5: Charge generation in a polymer/fullerene bulk heterojunction solar cell. (a) absorption of a photon resulting in an exciton (b) diffusion of exciton towards donor/acceptor interface (c) electron transfer from donor to acceptor (d) dissociation of the bound electron–hole pair into free charge carriers (e) transport of free carriers towards the electrodes (f) collection at the electrodes. Loss mechanisms are indicated by (1) non–absorbed photons (2) exciton decay (3) geminate recombination of the bound pair (4) bimolecular recombination.

(f) They are collected at the electrodes.

During the above mentioned processes, conversion efficiency of photon energy to charge collection at the electrodes gets lower as enumerated below.

1. Not all photons are absorbed by the active layer because the band–gap is larger than the energy of the photons.

2. Excitons will decay when created far away from the donor/acceptor interface.

3. After electron transfer, geminate recombination of the bound electron hole pair can occur.

4. Bimolecular recombination of the free charge carriers during transport to the electrodes.

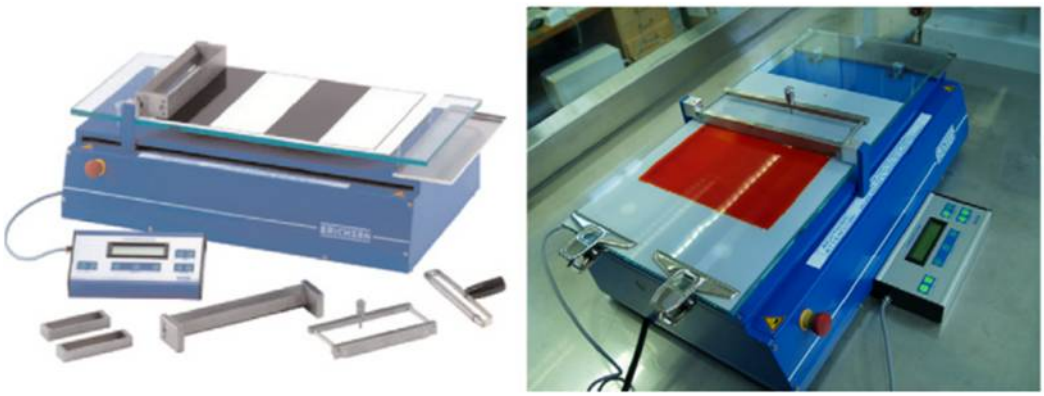

Figure 2.6: Picture of the Erichsen Coatmaster 509 MC-I that can be used for doctor blading (left) and a photograph showing doctor blading of a polymer (right).

2.4 Fabrication of polymer solar cells

Large scale production of polymer solar cells involve high volume and large area manufacturing which is possible through batch processing techniques such as roll–to–roll coating where the photoactive blend is soluble in common solvents [6–8, 35]. In the case of a solar cell fabricated from the photoactive blend of P3HT: PCBM, PCBM has solubilizing butyric acid methyl ester group and the donor P3HT has alkyl–side chains that facilitate processing from solution. However, most of the reported studies conducted in research laboratories on polymer/fullerene active blend have used blends processed using the technique of spin–coating which is not directly transferable to roll–to–roll coating since the shear forces involved in coating and the solvent evaporation time involved in drying of the polymer/fullerene blend after roll–to–roll coating is not the same as in spin–coating. Hence the knowledge advanced so far in the understanding of processing–structure–properties relationship for spin–coated polymer/fullerene photoactive blend films is not directly transferable to an industrially relevant process of roll–to–roll coating. But the process of doctor–blading is a laboratory scale fabrication method which is directly scalable to roll–to–roll processing. Doctor–blading is essentially a knife coating technique whereby a knife homogeneously spreads ink (in this case, a polymer/fullerene photactive blend in an organic solvent) as the blade is drawn over a substrate. Doctor–blading is fully compatible with roll–to–roll processing. Ink formulation for doctor blading is quite comparable to that for spin coating. Four parameters determine the film formation: the concentration (responsible for the viscosity of the ink), the temperature of the solution, the speed of the blade and the distance between the blade and the substrate (the volume of ink being deposited). Figure 2.6 shows a photograph of a typical doctor–blading apparatus. In this thesis, only doctor–blading has been used to process P3HT: PCBM blend films.

2.5 Challenges in polymer solar cells

The efficiency of polymer solar cells is low when compared to silicon or compound semiconductor technologies. Polymer solar cells would be suitable for commercial purposes when their efficiencies surpass 10% [5]. The current drawbacks of polymer solar cells are enumerated below.

1. The photoactive layer of polymer solar cells have narrow absorption of the incoming solar spectrum. Most semiconducting organic polymers have band–gap larger than 1.9 eV, covering only $\sim$ 24% of the air mass 1.5 global solar photon flux, which is the intensity of insolation equivalent to the Sun shining through the atmosphere to sea level, with oxygen and nitrogen absorption, at an oblique angle 48.2° from the zenith), while a bandgap of 1.1 eV can cover $\approx$ 63% of the AM 1.5G solar photon flux, assuming ideal absorption of the solar photon flux by the materials.

2. The short–circuit current of polymer solar cells need to be increased through photo–absorption enhancement in the infra–red region by using low band–gap organic material and active acceptor materials and by improving the charge mobility and charge collection efficiency [36]. The short–circuit current in polymer/fullerene bulk heterojunction photovoltaic devices can be improved through interface and surface engineering at the electrodes, through surface plasmons at the anode surface [37], efficient electron–blocking/hole–transporting anode interfacial layers and tandem cell architecture/multi–junction solar cell [38, 39].

3. Polymer solar cells have short–term stability. Device degradation should be minimized through device design, materials engineering and improved encapsulation method [9].

2.6 Structure of P3HT: PCBM blend — a typical photoactive blend in a polymer solar cell

During the last five years, research efforts have focused on poly–(alkylthiophenes) and in particular on poly–(3–hexylthiophene) (P3HT) (Figure 2.7 a) and [6,6]–phenyl–C_{61}–butyric–acid–methyl–ester (PCBM) (Figure 2.7 b) in a blend in solvent ortho– dichlorobenzene (DCB) (Figure 2.7 c). The distance between the polymer chains in a–direction (along the side–chain) is determined by the length of the side–chains. The distance between the polymer chains in the stacking direction (b–direction) is determined by interaction between neighbor thiophene rings. Finally, the parameter c is simply the

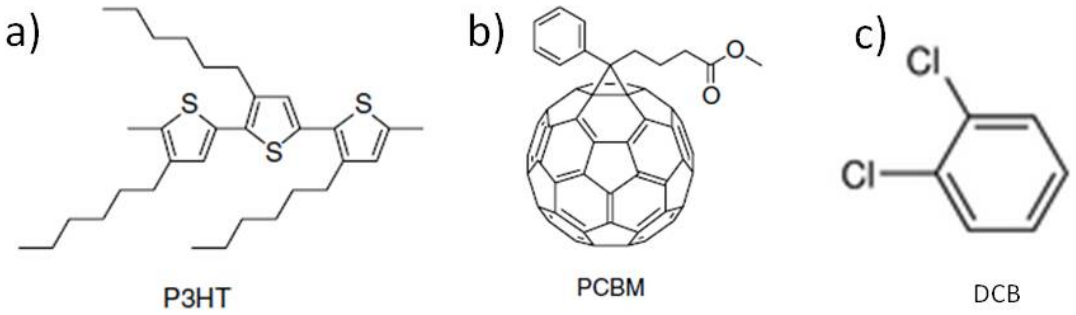

Figure 2.7: Chemical structure of (a) P3HT (b) PCBM (c) DCB.

The P3HT crystallite has lattice constants $a = 16.8\,\text{Å}$, $b = 7.6\,\text{Å}$ and $c = 7.6\,\text{Å}$ [40–50].

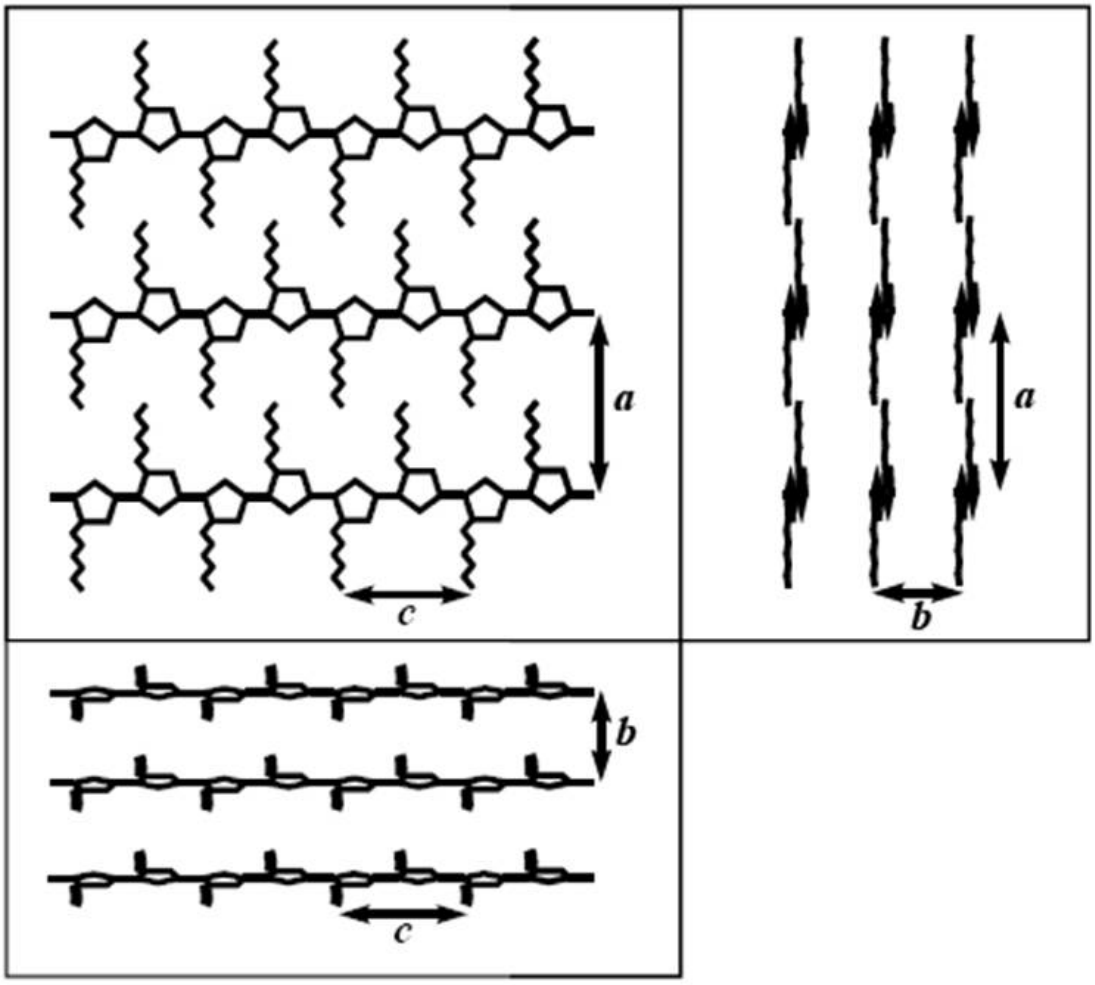

Figure 2.8: P3HT crystal along different projections [51].

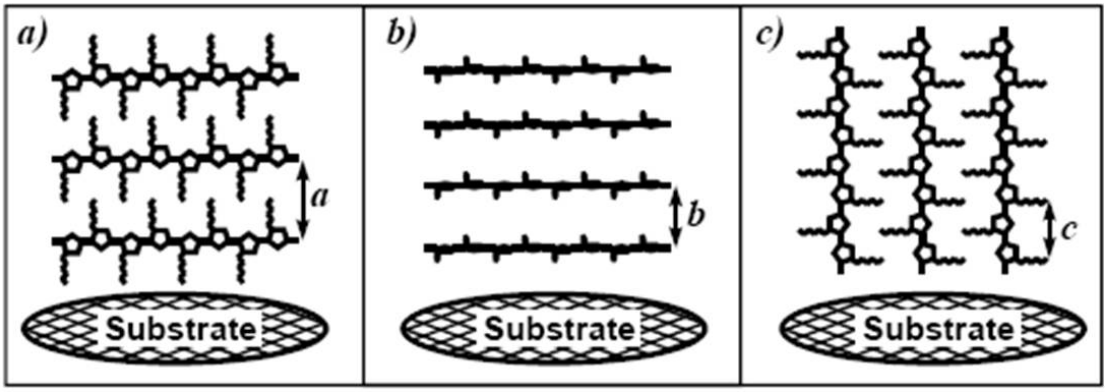

Figure 2.9: (a) *a*– (b) *b*– and (c) *c*–axis orientations of P3HT crystal with respect to the substrate. The orientation of P3HT in (a) is known as "edge–on" and in (b) is known as "face–on" [51].

length of the repeating unit. P3HT crystals along different directions is shown in Figure 2.8. In *a*–axis oriented crystallites the polymer backbone is oriented parallel and the alkyl side–chains perpendicular to the substrate, respectively. In *b*–axis oriented crystallites both polymer backbone and side–chains are parallel to the substrate, whereas in *c*–axis oriented crystallites the backbone is perpendicular to the substrate (Figure 2.9).

2.7 Importance of controlling the nanomorphology of the photoactive blend in a polymer solar cell

The device performance of the polythiophene/fullerene blend solar cell is critically dependent on the processing condition, which influences the polymer self–organization and thereby the nanostructure and nanomorphology of the blend film ultimately affecting the corresponding optical and electrical properties [10, 52, 53]. Controlling the nanomorphology of the bulk heterojunction photoactive blend ensures maximum exciton dissociation at the interface between the donor and the acceptor and an efficient charge carrier extraction leading to the fabrication of high performing solar cells. The following sections will elaborate how the nanomorphology and nanostructure of the photoactive blend of a polymer solar cell changes upon different processing conditions.

2.7.1 Effect of annealing the photoactive blend

Annealing in polymer solar cells can be divided into two categories: thermal annealing [54–61] and solvent annealing [62–66]. Both improve the nanoscale lateral phase separation of the crystalline P3HT aggregates and PCBM domains, cause the films to get rougher than as–cast films and improve the device performance.

1. **Effect of thermal annealing** — Thermal annealing can be applied either on the final device (post–annealing) or on the polymer film only (pre–annealing). The annealing temperature, time, solvent and electrodes are the deciding parameters in this technique which affect the ultimate device performance, attributed to an enhancement of the charge carrier transport, by a larger hole mobility, reduced dispersivity and a reduced recombination kinetics [54, 55, 55–61, 67–71]. Morphological studies have revealed that the organization of the P3HT: PCBM is modified upon annealing, [69, 72] with fibrillar–like P3HT crystals embedded in a matrix of mostly PCBM nanocrystals and amorphous P3HT [69]. The crystallinity of P3HT is observed to increase by thermal annealing; P3HT forms crystallites with the conjugated chain parallel to the substrate (a–axis orientation) [54]. The improved crystallinity enhances the near–infrared region absorption and the hole mobility, and reduces charge recombination due to the improved percolation pathway, all of which lead to better device performances.

2. **Effect of solvent annealing** — The solvent annealing approach controls the polymer nanomorphology through the solvent removal speed [73–75]. A systematic study of the spin–coating time reveal the advantage of solvent annealing over thermal annealing by sustaining the P3HT ordered structure upon higher PCBM loadings [76, 77]. Controlling the solvent evaporation rate improved the molecular ordering of the P3HT chains as the packing of the polymer chain is strongly affected by the solvent removal rate [78]. Fast solvent removal leads to not only the reduction of P3HT crystallinity, but also increases the interlayer distance of the polymer in the blend film. With carrier transport occurring through a hopping model in the interlayer direction, a fast solvent removal rate is not preferred. The inherent low hole mobility is usually the bottleneck of carrier transport in polymer solar cells, which limits device performance.

Various annealing processes can dramatically improve the crystallinity, resulting in higher hole mobility; thus to date annealing has become the most commonly used method for device-performance improvement.

2.7.2 Effect of the molecular weight of the polymer

Lower molecular weight P3HT has inferior mobility as main–chain defects develop along with the growth of crystalline fibrils during annealing, leading to a large number of small crystals, while higher molecular weight P3HT stays amorphous [56–58, 79]. Very high molecular weights of P3HT produce highly entangled polymer networks, rendering annealing either impossible or requiring higher temperatures and/or longer

annealing times [63]. The ideal morphology forms when P3HT has an average molecular weight between 30000 to 70000 and polydispersity ≈ 2, which enables a mixture of highly crystalline regions formed by low molecular weight P3HT embedded in and interconnected by a high molecular weight P3HT matrix [56, 64].

2.7.3 Effect of the polymer regioregularity

The influence of the regioregularity of the polymer, defined as the percentage of monomers adopting a head–to–tail configuration, rather than a head–to–head is critical. A specific threshold for the regioregularity, about 95% is necessary to get better performing solar cells because of better transport properties of highly regioregular P3HT [62, 65, 66].

2.7.4 Effect of the photoactive blend composition

Polymer/fullerene binary displays simple eutectic behavior and the optimum composition for photocurrent generation after thermal annealing is related to the composition of P3HT at the eutectic point but displaced to higher fullerene–derivative contents in order to achieve balanced transport that depends on the polymer crystallinity [80]. In only polymer binaries, there is a strong tendency of macromolecules to phase separate in the liquid state that complicates the formation of the desired interpenetrating microstructure of their blends. In mixtures of small molecules like fullerene–derivatives, interpenetrating network formation is hindered because only one of the two constituents in such binaries will form primary crystals which promote percolation. In this case, conventional processing routes are likely to generate transport pathways for only one type of charge carrier. Efficient charge transport for both electrons and holes may, however, be induced by directional eutectic solidification of the active photoactive layer. So the blend composition of the P3HT: PCBM binary system is critical for designing and processing effective solar cells. It has been reported that the ideal blend composition ratio for P3HT: PCBM is $\approx 1 : 0.7$ [80]. In this thesis, unless otherwise mentioned, the P3HT: PCBM blend composition ratio has been kept as $1 : 0.8$.

2.7.5 Effect of processing solvents on the photoactive blend

Solution processing allows the freedom to control phase separation and molecular self–organization during solvent evaporation and film treatment. The solvent establishes the film evolution environment and thus has impact on the final film morphology [62, 81, 82]. Solvent properties, such as boiling point, vapor pressure, solubility, and polarity, also have considerable impact on the final film morphology. The type of sol-

vent used determines the final morphology and structure of the dried blends. Ma et al. observed that P3HT: PCBM polymer films were smoother and more uniform when chloroform was replaced with chlorobenzene [72]. The high efficiency is the result of improved morphology, crystallinity, and cathode contact due to better choice of solvent as well as post–annealing treatment. The nanomorphology of P3HT: PCBM blends can be controlled by the addition of "non–solvents" into solution. This phenomenon is attributed to the aggregation of the polymer into nanoparticulates. Addition of nitrobenzene to a P3HT: PCBM solution in chlorobenzene allows an increase in the volume fraction of P3HT aggregates from 60% to 100%. Photovoltaic devices from P3HT: PCBM mixtures with nitrobenzene as additive allowed the manufacture of devices with efficiencies as high as 4% without thermal annealing. These experiments proved that a good part of the thin-film morphology can already be introduced on the solution level [83]. Slow drying of the solvent during processing of the photoactive layer of solar cells improves the structural order in P3HT blends with PCBM [74]. The improved order has been reflected in higher hole mobility of the processed solar cells [68, 75, 84].

2.7.6 Effect of processing additives on the photoactive blend

Additives in the photoactive P3HT: PCBM blend films have been observed to create better structural order. Oleic acids and alkylthiols of different lengths, like n–hexylthiol, n–octylthiol, or n–dodecylthiol when added to P3HT: PCBM solutions allow the formation of thin films with enhanced hole mobility and significantly enhanced charge–carrier lifetimes because of the formation of enlarged P3HT domains with higher crystallinity [85–88]. P3HT has an intrinsic property to self–organize into microcrystalline domains even without any additive. However the addition of additives lead to the loss of P3HT ordering and to PCBM being finely dispersed at a molecular level between P3HT chains, preventing P3HT crystallization, and thereby redistributing PCBM and P3HT in the composite film. Additives should have the following properties:

1. It must have lower vapor pressure (or higher boiling point) than the primary solvent at room temperature.

2. It must have lower solubility of PCBM than the primary solvent.

3. It must be miscible with the primary solvent.

4. Its boiling point cannot be too high as then the additive will not be removed from the film during doctor–blading or spin–coating and thermal treatment would be required to remove the residue.

Dissimilar solvent mixtures facilitate PCBM cluster formation and leads to intelligent phase separation of the active layer into an optimum morphology.

2.7.7 Effect of processing microemulsions on the photoactive blend

When a mixture of P3HT in water, surfactants and a solvent is rigorously sonicated before allowing the solvent to evaporate, it forms a dispersion which typically has particle distribution sizes between 70 to 200 nm and forms homogeneous films upon spin–coating [89]. Field–effect transistor mobilities for such films were found to be on the order of 10^{-4} to 10^{-3} $cm^2V^{-1}s^{-1}$. Solar–cell fabrication with dispersion is difficult and there are no known well–performing, water–soluble fullerenes [90–92]. So solar cells fabricated with microemulsions are not a viable option.

CHAPTER 3

Outline of thesis

In this thesis, the evolution of the morphology and the structure of the blend of electron – rich, semiconducting conjugated polymer poly(3 – hexylthiophene) (P3HT) with the electron – deficient, semiconducting fullerene – derivative [6,6] – phenyl – C_{61} – butyric – acid – methyl – ester (PCBM) in a common solvent 1,2 – dichlorobenzene (DCB) has been studied in-situ using x-ray scattering techniques during the formation of ultra-thin films through solvent drying process. The effect of different technologically relevant processing parameters on the structural and morphological evolution of P3HT: PCBM blend has been investigated in this thesis work. The processing parameters, such as the drying temperature, blend composition, solvent mixture and additives in the primary solvent DCB have been seen to affect the performance of the solar cells. The processing parameters affect the nanomorphology and nanostructure of P3HT: PCBM blend films during drying and that in turn affects the performance of solar cells made with these blend films. Only empirical knowledge exists about this process (refer to the schematic diagram shown in Figure 3.1). The aim of this thesis work is to develop microscopic understanding of this technologically important process. The outline of

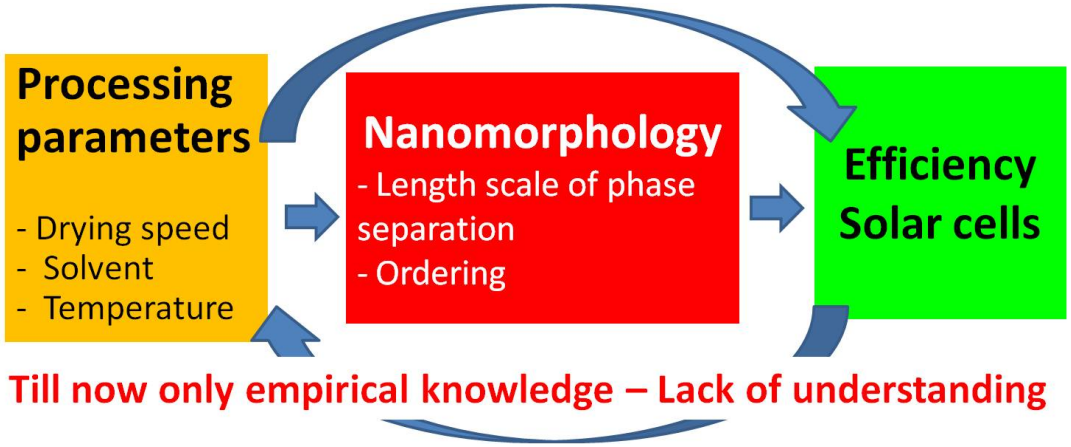

Figure 3.1: Schematic showing the present status of research in polymer solar cells.

this thesis has been enumerated below.

1. The importance of studying polymer solar cells has been described briefly in chapter 2. The different characteristics and properties of the photoactive blend in a polymer solar cell and its effect on the performance of the polymer solar cell has been briefly described in this chapter.

2. The theory behind the various experimental techniques used in this thesis has been described in chapter 4.

3. A description of the various experimental set–ups used in this thesis has been given briefly in chapter 5.

4. The real–time in–situ structural evolution of P3HT: PCBM blend coated on silicon dioxide substrate during evaporation of the solvent DCB has been studied using real–time x–ray scattering in chapter 6. In this chapter, it has been shown for the first time that the P3HT: PCBM blend undergoes solidification from a smectic liquid crystalline state during solvent evaporation. The in–situ evolution of the elastic constants, namely the bulk modulus and the bending rigidity modulus, using diffuse x–ray scattering analysis of the P3HT: PCBM blend as the solvent evaporates, is the novelty of this chapter. In this chapter, a novel method has been developed to probe the material properties of the blend film while it is being processed from solution.

5. The effect of drying temperature on the real–time in–situ structural evolution of P3HT: PCBM blend coated on industrially relevant PEDOT:PSS/ITO/Glass substrates has been studied using x–ray scattering in chapter 7. The study showed for the first time that the effect of drying temperature on the ordering of P3HT in the out–of–plane direction, along q_z, and in–plane direction, along q_{xy}, is different. The x–ray scattering data was complemented with optical absorption data and atomic force microscopy data. This chapter provides a nanostructural and nanomorphological reason to show why solar cells fabricated at low temperatures have better performance.

6. The effect of P3HT: PCBM composition ratio on its structural evolution has been studied in–situ using real–time x–ray scattering in chapter 8. In this chapter, it has been demonstrated that the composition ratio of the blend dictates the final dried blend structure and that by increasing the content of PCBM in P3HT: PCBM blend, new features of both P3HT and PCBM are observed.

7. Preliminary studies on the effect of a new primary solvent indane and its mixture

with other solvents has been studied on the dried P3HT: PCBM blend structure using ex–situ x–ray scattering in chapter 9.

8. The combined effect of drying temperature and additives on the dried P3HT: PCBM blend structure has been studied using ex–situ x–ray scattering in chapter 10.

9. The salient results of this thesis work has been concisely summarized in chapter 11 where few open questions regarding the topic of this thesis have also been posed.

CHAPTER 4

Experimental Methods

Precise characterization of structural and morphological properties of a material is only possible using complementary techniques. This chapter provides a short theoretical overview of the different experimental techniques used in this thesis to gain accurate information of the overall polymer thin film structure.

4.1 X-ray Reflectivity

A treatise on this topic is written by Warren, Guinier and Holy et al. [93–95]. The elastic scattering length of electrons is called Thomson scattering length, which is the classical electron radius denoted by r_e. For elastic scattering, the incoming and outgoing wave of wavelength λ has equal magnitude of wave vector ($k_i = k_f = \frac{2\pi}{\lambda}$); the wave vector transfer $\mathbf{q}$ in the scattering is $\mathbf{q} = \mathbf{k_f} - \mathbf{k_i}$ where λ is the wavelength. The components of the wave vector transfer $\mathbf{q}(x, y, z)$ are (Figure 4.1)

$$q_x = \frac{2\pi}{\lambda}(cos\alpha_f cos\phi - cos\alpha_i) \tag{4.1.1}$$

$$q_y = \frac{2\pi}{\lambda}(cos\alpha_f sin\phi) \tag{4.1.2}$$

$$q_z = \frac{2\pi}{\lambda}(sin\alpha_i + sin\alpha_f) \tag{4.1.3}$$

Assuming kinematic approximation where absorption and multiple scattering effects are neglected, the scattering length of an atom is

$$f_0(\mathbf{q}) = r_e \cdot \int \rho(\mathbf{r}) e^{i\mathbf{q}\cdot\mathbf{r}}\, d^3r \tag{4.1.4}$$

where $f_0(\mathbf{q})$ is the Fourier transform of the distribution of a continuous electron density $\rho(\mathbf{r})$ around a nucleus within an atom, also known as the atomic form factor. $\mathbf{q}\cdot\mathbf{r} = (\mathbf{k_f} - \mathbf{k_i})\cdot\mathbf{r}$ is the phase shift between waves scattered from different volume elements. It is to be noted here that Equation 4.1.4 is not only valid for scattering of

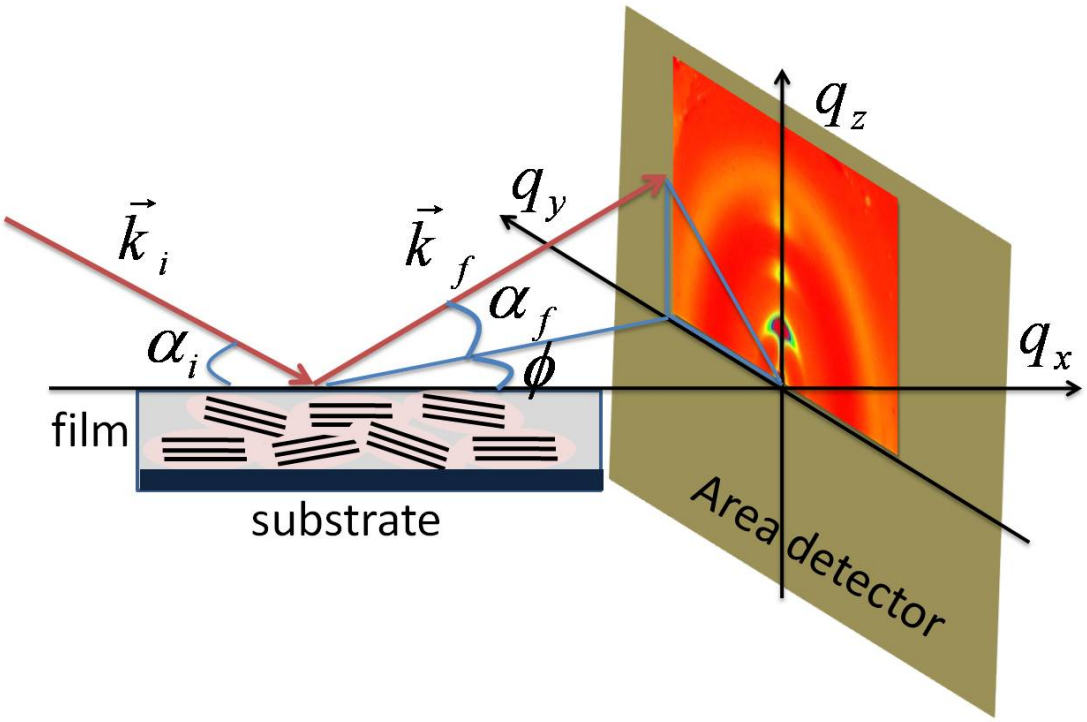

Figure 4.1: Schematic of the x–ray scattering geometry used in this thesis work. The components of the wave vector transfer $\mathbf{q}(x, y, z)$ are $q_x = \frac{2\pi}{\lambda}(cos\alpha_f cos\phi - cos\alpha_i)$, $q_y = \frac{2\pi}{\lambda}(cos\alpha_f sin\phi)$ and $q_z = \frac{2\pi}{\lambda}(sin\alpha_i + sin\alpha_f)$.

electrons in one atom but also for any system where one can define a general electron density $\rho(\mathbf{r})$. It should also be mentioned here that atomic scattering factor $f_0(\mathbf{q}$ gets modified due to electron nucleus interaction that give rise to atomic levels, the expression for form factor contains two additional energy dependent terms called dispersion and absorption correction factors, resulting in

$$f(\mathbf{q}, E) = f_0(\mathbf{q}) + f'(E) + f''(E) \tag{4.1.5}$$

The structure factor of a single molecule is the sum of the atomic form factors given by

$$F_{mol}(\mathbf{q}) = \Sigma_j f_j(\mathbf{q}) e^{\mathbf{q}\cdot\mathbf{r_j}} \tag{4.1.6}$$

where f_j is the atomic form factor for each atom and $\mathbf{r_j}$ is the respective atomic position. Atomic positions of a crystalline solid depends on the space group of the material and can be found in the International Tables of X–ray crystallography. The structure factor of the unit cell of a crystalline solid is the sum of molecules k given as

$$F_{unitcell}(\mathbf{q}) = \Sigma_k F_{k,mol}(\mathbf{q}) e^{i\mathbf{q}\cdot\mathbf{r_k}} d^3r \tag{4.1.7}$$

The structure factor of a crystal lattice is the sum of n unit cells resulting in

$$F_{crystal}(\mathbf{q}) = \Sigma_n F_{n,unitcell}(\mathbf{q}) e^{i\mathbf{q}\cdot\mathbf{r_n}} d^3r \tag{4.1.8}$$

Presuming that the crystal has n unit cells, the scattered intensity which is proportional to the modulus square of the structure factor of the crystal can be written as

$$I(\mathbf{q})_{crystal} \propto |F(\mathbf{q})_{crystal}|^2 . \frac{sin^2(N_x \mathbf{q}\cdot\mathbf{a_x}/2)}{sin^2(\mathbf{q}\cdot\mathbf{a_x}/2)} \frac{sin^2(N_y \mathbf{q}\cdot\mathbf{a_y}/2)}{sin^2(\mathbf{q}\cdot\mathbf{a_y}/2)} \frac{sin^2(N_z \mathbf{q}\cdot\mathbf{a_z}/2)}{sin^2(\mathbf{q}\cdot\mathbf{a_z}/2)} \tag{4.1.9}$$

where N_x, N_y and N_z are the number of unit cells and $\mathbf{a_x}$, $\mathbf{a_y}$, $\mathbf{a_z}$ the lattice vector in the three crystallographic directions. Hence, the intensity pattern for a crystalline solid having large number of unit cells give rise to sharp peaks at specific $\mathbf{q}$ (q_x,q_y,q_z) position that satisfies the Laue condition $\mathbf{q}\cdot\mathbf{a_x} = \mathbf{q}\cdot\mathbf{a_y} = \mathbf{q}\cdot\mathbf{a_z} = 2\pi$. The intensity is proportional to the square modulus of the structure factor hence depending on the molecular arrangement within the unit cell and its associated electron density. It should be noted here that for nanomaterials having small number of unit cells will increase the width of these diffraction peaks and will be discussed later. From Equation 4.3.9, the scattered intensity of a one dimensional crystal is

$$I(\mathbf{q})_{crystal} \propto |F(\mathbf{q})_{crystal}|^2 . \frac{sin^2(N_z q_z a_z/2)}{sin^2(q_z a_z/2)} \tag{4.1.10}$$

when q_x and q_y are set to zero. At the position of the principal maxima, the momentum transfer equals the reciprocal lattice vector $a_z^* = 2\pi/a_z$. The peak intensity at the maxima are proportional to ${N_x}^2 {N_y}^2 {N_z}^2$. The distance between minima of adjacent side peaks Δq_z determines the crystal size or in the case of a film its coherent thickness $D_{coh} = 2\pi/\Delta q_z$. These results can be extended to three dimensions.

The index of refraction n of a material in the x–ray region can be expressed as

$$n = 1 - \delta_d + i\beta_a \tag{4.1.11}$$

where $\delta_d = \lambda^2 r_e \rho/2\pi$ is the dispersion and $\alpha_{f_a} = \lambda\mu_a/4\pi$ is the absorption, r_e is the Thomson scattering length, ρ is the electron density and μ_a is the absorption coefficient of the respective material. The Equation 4.1.11 is only valid in the condition when x–ray energies are far from absorption edges otherwise one has to consider anomalous scattering terms given in Equation 4.1.5. In this thesis work, all data were collected far away from the absorption edges and hence anomalous factors can be neglected here.

For incidence angles α_i below the critical angle $\alpha_{crit} = \sqrt{2\delta_d}$, x–rays undergo total external reflection as $n < 1$. Almost all incoming radiation is reflected (there are small losses due to absorption) since the x–rays do not penetrate into the medium. With increasing incident angle, however, the reflectivity R is

$$R \approx (\frac{\alpha_{crit}}{2\alpha_i})^4 for\, \alpha_i > 3\alpha_{crit} \tag{4.1.12}$$

deduced from the Fresnel equations.

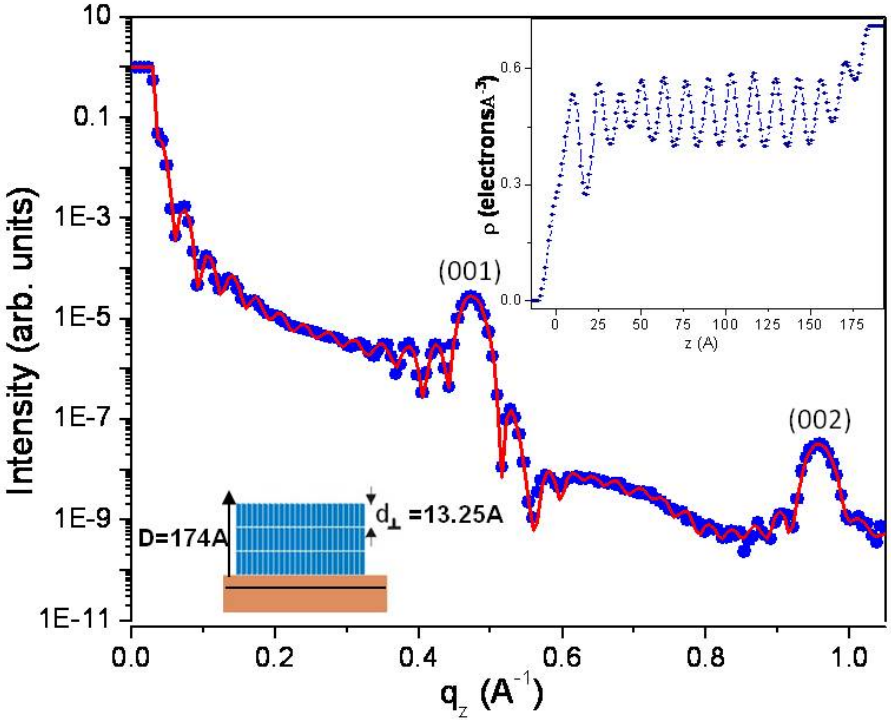

Figure 4.2: Specular x–ray diffraction data (dots) and fit with Parratt algorithm (line) from cobalt phthalocyanine (CoPc) film on silicon dioxide [96]. The bottom inset shows the schematic of the investigated film structure and the top inset shows the electron density profile. The total thickness of the film is 174 Å, and the interlayer spacing is 13 Å.

Consider a system of two perfect layers with two interfaces where one layer represents the substrate and the second layer represents a homogeneous film which has an internal periodic modulation of the electron density. Periodic oscillations called Kiessig fringes appear due to the interference of x–rays scattered at the vacuum/film and film/substrate interface. The width Δq_z of each oscillation is related to the film thickness D as $D = 2\pi/\Delta q_z$ with $q_z = 4\pi sin\alpha/\lambda$ being the momentum transfer perpendicular to the surface for equal incident and exit angles α_i and α_f. Additional peaks visible in the intensity pattern called Bragg peaks (Figure 4.1) arise when the Bragg condition $2dsin\alpha = N\lambda$; here N is an integer and d is the film periodicity. The reflected intensity has information about the projection of the electron density along the surface normal $\rho(z)$ which is directly related to the projected crystalline structure in this direction. Structural information such as of a complex layered of a thin film of cobalt phthalocyanine (CoPc) system (Figure 4.2) can be obtained from a fit of the x–ray reflectivity data. For this analysis, an adequate structure model of the electron density

has to be proposed for which the x–ray intensity has to be calculated and compared to the experimental one. One of the methods of this type of calculation is called the Parratt formalism where the electron density profile is obtained by dividing the film into a series of slabs with $N+1$ slabs having well defined interfaces, each slab corresponding to a layer in the film [97].

4.2 Grazing Incidence X–ray Diffraction

A treatise on this topic has been written by Dosch [98]. In grazing incidence x–ray diffraction (GIXD) techniques, one extracts the in–plane structural information of a film. The sensitivity of this technique is enhanced by choosing the grazing angle of incidence α_i below the critical angle α_{crit} the totally reflected wave is accompanied by an evanescent wave field which travels parallel to the film–surface. The amplitude of the evanescent wave is exponentially damped according

$$A_{eva} \propto e^{i\mathbf{k}_{||}\cdot\mathbf{r}_{||}} \cdot e^{-z/\Lambda} \tag{4.2.1}$$

and propagates perpendicularly in the range of a few nanometers [99]. $\mathbf{k}_{||}$ denotes the wave vector parallel to the surface and $\mathbf{r}_{||}$ the plane parallel to the surface. z is the direction normal to the surface and Λ the penetration depth into the medium at which the amplitude of the wave has decreased to $1/e$. The high surface sensitivity of evanescent waves makes it possible to reveal lateral structural properties since the momentum transfer is mainly determined by the component $q_{||}$ in the plane as can be seen from the scattering geometry in Figure 4.1. By varying the incidence and scattering angles α_i and α_f depth dependent structural studies can be performed. Note that the organic films examined in this thesis exhibit randomly oriented crystalline domains which implies that the in–plane structure is a two dimensional powder. Therefore all GIXD scans were performed by rotating the detector around the fixed sample shown in Figure 4.1.

4.3 Off–Specular Diffuse Scattering

Rough surfaces reduce specularly reflected intensity considerably; giving rise to enhanced diffuse scattering at exit angles $\alpha_f \neq \alpha_i$, i.e. in off–specular directions. The specular reflectivity is sensitive only to the vertical density profile $\rho(z)$ of a sample. On the other hand, measurement of diffuse scattering help us to understand the lateral fluctuations of a surface and gives in–plane correlations [100–103]. Detailed discussion on off–specular diffuse scattering has been done by Tolan and Daillant and Alba [104, 105].

In the kinematical approximation, only single scattering events are taken into account ("weak scattering regime"). So the scattering function $S(\mathbf{q})$ is the modulus squared of the spatial Fourier transform of the scattering length density $\rho(\mathbf{r})$, which is

$$S(q) = \iint \rho(r)\rho(r')exp(iq(r-r'))\,dr\,dr' \tag{4.3.1}$$

where the vectors $\mathbf{r} = (x, y, z)$ and $\mathbf{r}' = (x', y', z')$ are independent spatial coordinates and $\mathbf{q} = (q_x, q_y, q_z)$ is the scattering vector. The expression can be simplified for an interface by considering the fact that height–difference correlation function can uniquely characterize an interface as

$$g(\mathbf{r}) = \langle [h(\mathbf{r}) - h(\mathbf{0})]^2 \rangle \tag{4.3.2}$$

where $h(\mathbf{r})$ is an interfacial displacement at any lateral position $\mathbf{r}(x, y)$ relative to some arbitary origin and $\langle\rangle$ denotes the ensemble average. The height–height correlation function $\langle h(\mathbf{r})h(\mathbf{0})\rangle$ is related to the height difference correlation function as $g(\mathbf{r}) = 2\sigma^2 - \langle h(\mathbf{r})h(\mathbf{0})\rangle$ where σ^2 is the total intrinsic mean–square interfacial displacement with "roughness" parameter σ. The $g(\mathbf{r})$ for various surfaces and interfaces can be approximated with a variety of functions. For solid surfaces, the height–height correlation function decays to zero above a $\mathbf{r}(x, y)$, known as "correlation length" and as a result below a certain q_{xy} scattering become prodominantly specular in nature. Then one can separate out the specular component from the total scattering and one can extract the in–plane averaged electron density profile as a function of depth from specular scattering data. For a liquid surface, the height–height correlation function can be approximated with a Bessel function $K_0(x)$ using the theory of capillary waves and this function goes to zero only when $\mathbf{r}(x, y) \to \infty$. This implies that unlike solid surfaces, specular and diffuse scattering components cannot be separated out and one has to calculate the total scattering cross–section from

$$g(\mathbf{r}) = 2\sigma^2 - BK_0(Kr) \tag{4.3.3}$$

where

$$B = \frac{k_B T}{\pi\gamma} \tag{4.3.4}$$

γ being the surface tension of the interface at temperature T. Here σ^2 is the total intrinsic mean–square interfacial displacement given by

$$\sigma^2 = \frac{k_B T}{4\pi\gamma} ln[\frac{{q_u}^2 + K^2}{K^2}] \tag{4.3.5}$$

where $K = \sqrt{\frac{\Delta\rho g}{\gamma}}$ is the gravitational cut–off with $\Delta\rho$ being the difference in mass density across the interface, g the acceleration due to gravity and q_u is the upper wave–vector cut–off determined by the molecular dimensions. The cross–section and hence

the scattered intensity is proportional to $S(\mathbf{q})$. Assuming that $z(x,y) - z(x',y')$ is a Gaussian random variable depending only on the distances $X = x - x'$ and $Y = y - y'$, the structure factor becomes

$$S(q) = \frac{(\Delta\rho)^2}{{q_z}^2} exp(-{q_z}^2\sigma^2) \iint exp({q_z}^2 C(x,y)) \times exp(-i(q_x X + q_y Y))\, dX\, dY \qquad (4.3.6)$$

where σ is the rms roughness of the interface and $C(X,Y) = \langle h(\mathbf{r})h(\mathbf{0})\rangle$ is the height–height correlation function. Adapting to experimental conditions with wide–open slits in the out–of–plane y direction and an inclusion of the q_x resolution δ_{q_x} with a real–space cutoff function $R(X) = exp(-4\pi^2 X^2/L^2)$ where $L = 2\pi/\delta_{q_x}$, yields the kinematical scattering function

$$S(q_x,q_z) = \frac{(\Delta\rho)^2}{{q_z}^2} exp(-{q_z}^2\sigma^2) \times \int_0^\infty exp({q_z}^2 C(X)) exp(-4\pi^2 X^2/L^2) cos(q_x X)\, dX \qquad (4.3.7)$$

Considering height–height correlation of a liquid surface (refer Equation 4.3.3 and note $g(\mathbf{r}) = 2\sigma^2 - 2C(r)$) that can be written as

$$C(X) = \frac{B}{2} K_0(q_{l,c} X) \qquad (4.3.8)$$

is inserted in Equation 4.3.7 a separation between a delta–like purely specular part and a diffuse contribution would indeed be possible since $K_0(q_{l,c}X) \longrightarrow 0$ for $X \longrightarrow \infty$ and $B = \frac{k_B T}{\pi\gamma}$. However, since the cut–off $q_{l,c} = K = \sqrt{\frac{\Delta\rho g}{\gamma}} \backsim 10^{-7}$–$10^{-8}$ Å^{-1} is very small for bulk liquids, where γ is surface tension and in practice $q_{l,c} \ll \delta_{q_x}$ is generally fulfilled, $K_0(q_{l,c}X)$ is approximated by its leading term $K_0(q_{l,c}X \approx -ln(q_{l,c}X/2) - \gamma_E$, which is valid in the experimentally accessible q range. After inserting the logarithmic correlation function in Eq. 4.3.7 and multiplying by the respective transmission functions $|t_i(\alpha_i)|^2 |t_f(\alpha_f)|^2$ to account for dynamical scattering effects, the following result was obtained by Sanyal et al. for the observed intensity $I(q_x,q_z)$ recorded in a detector as

$$I(q_x,q_z) = I_0 (\frac{q_c}{2q_z})^4 \frac{sin\alpha_i + sin\alpha_f}{2\sqrt{\pi} sin\alpha_i} exp(-q_z^2\sigma_{eff}^2) \Gamma[\frac{1-\eta}{2}]_1 F_1[\frac{1-\eta}{2}; \frac{1}{2}; \frac{-q_x^2 L^2}{4\pi^2}] |t_i(\alpha_i)|^2 |t_f(\alpha_f)|^2 \qquad (4.3.9)$$

where I_0 is the incident beam intensity, $q_c = 2ksin\alpha_c$ is the wave–vector corresponding to the critical angle α_c, $\Gamma(x)$ is the Gamma function, ${}_1F_1(x;y;z)$ is the Kummer function, and L is the effective coherence length along the surface. Using the effective surface roughness σ_{eff} and $\eta(q_z) = \frac{k_B T}{2\pi\gamma} q_z^2 = \frac{1}{2} B q_z^2$ in the specular case, $\alpha_i = \alpha_f (q_x = 0)$, Equation 4.3.9 may be simplified to $I(0,q_z) = I_0 R_F exp(-q_z^2\sigma_{eff}^2)$, where R_F is the Fresnel reflectivity. Equation 4.3.9 is also the expression for the diffusely scattered intensity. For $q_x \gg \delta_{q_x} = 2\pi/L$ and fixed q_z, an expansion of the Kummer function yields

$$I_{diff}(q_x,q_z) \sim q_x^{\eta(q_z)-1} \qquad (4.3.10)$$

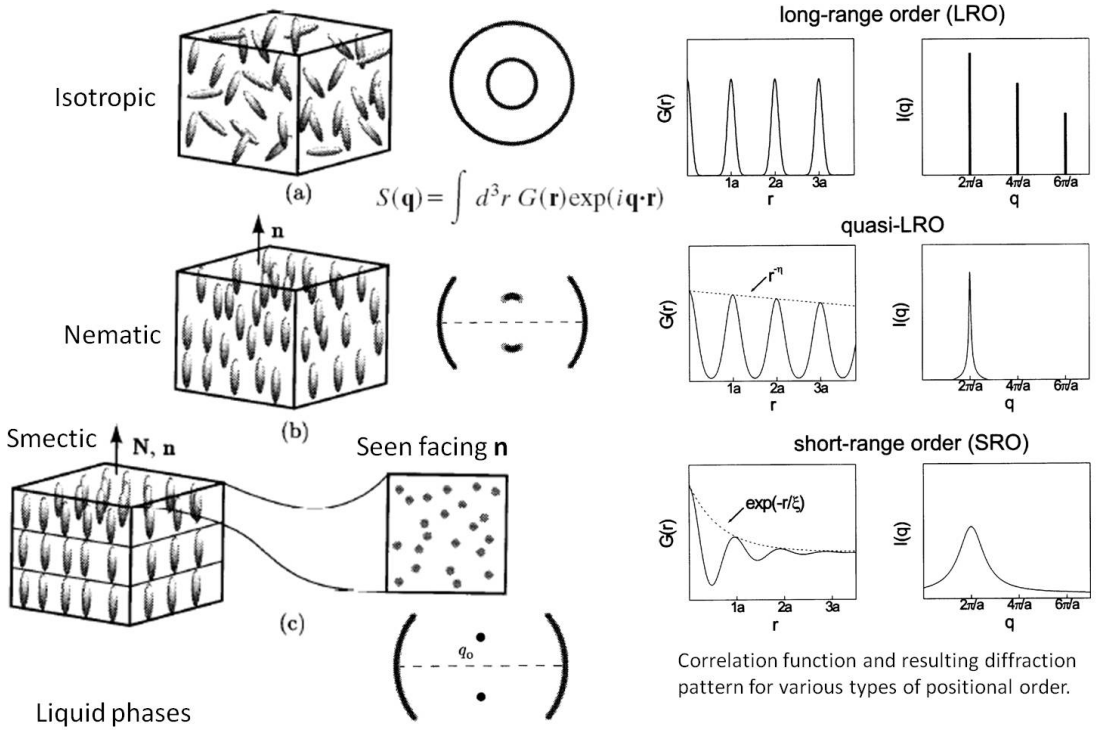

Figure 4.3: Schematic representation of the position and orientation of anisotropic molecules in (a) isotropic (b) nematic (c) smectic phases. The direction of the average molecular alignment in all but the isotropic phase is specified by a unit vector **n**. The layer normal in the smectic phases is indicated by the unit vector **N**. In the smectic phase, **n** is parallel to **N** (smectic–A phase). Here **N** is parallel to the z–axis. The arrangement of molecules in the smectic planes is also shown [108]. In the right, the Fourier transform of the density–density correlation function corresponding to each phase is plotted along with the corresponding diffraction pattern [107].

Capillary wave fluctuations on soft matter surfaces yield power laws for diffuse scattering. The power $\eta - 1$ depends on the vertical momentum transfer q_z. The first experimental proof of this prediction was given by Sanyal et al. in 1991 for liquid surface. The Kummer function provides a smooth transition between the Gaussian–like "specular" part and the power–law tails with q_z–dependent exponents.

A similar line shape is also observed for liquid crystal systems [107] (Figure 4.3). Strong thermal fluctuations lead to this characteristic features in the line shape in the diffuse x–ray scattering of liquid crystals. The details of this line shape was calculated by Caille and experimentally observed by Als-Nielsen et al.. The line shape of the diffuse scattering of liquid crystals exhibit similarity to that observed in liquid surface. The central gaussian portion goes into power law decay of intensity along $q_{x,y}$ with exponent $\eta - 1$ in this geometry. The exponent η for a liquid crystalline system depends on elastic constants associated with compression and undulation of the layers which shall

be discussed in detail in chapter 6. Extensions to the case of thin films can be made by replacing the gravitational cut–off $q_{l,c} = q_g$ by the much larger van der Waals cut–off $q_{l,c} = q_{vdW}(d) = a/d^2$, with length $a \backsim 5 - 10$ Å. In general $q_{vdW}(d)$ is larger than the resolution and so a specular part is contained and a separation into specular and diffuse scattering is possible. Thus for thin films the replacement of the Bessel function $K_0(q_{l,c}X)$ by the logarithm is not valid for all q_x and the integral has to be evaluated numerically with the correlation function $C(X) = \frac{B}{2}K_0(q_{l,c}X)$ for the fluid interface. However, the logarithmic expansion of $K_0(q_{l,c}X)$ is still valid for $q_{l,c}X \ll 1$ and a similar calculation to that given above for bulk liquid surfaces yields

$$I_{diff.}(q_x, q_z) \backsim q_x^{\eta(q_x)-1} \, for \, q_x \gg q_{l,c} = q_{vdW}(d) \tag{4.3.11}$$

Hence, the same power law is expected for large q_x. In the region $\delta_{q_x} < q_x < q_{l,c}$ a more complicated expression is found that is dominated by higher order terms of $K_0(q_{l,c}X)$

Like the specular reflectivity, the diffuse–scattering cross–section is proportional to the scattering length density contrast at an interface. Hence to obtain measurable x–ray diffuse scattering profiles, one needs to have electron density contrast at interfaces. Off–specular x–ray scattering provide us information regarding in–plane correlation at surfaces and interfaces. It should be emphasized here that in–plane correlation of buried interfaces are not accessible by other techniques such as atomic force microscopy, scanning tunneling microscopy that probe only the morphology of the exposed surface. In this thesis, it has been demonstrated that grazing incidence x–ray scattering techniques like off–specular diffuse scattering and grazing incidence diffraction can provide information regarding surfaces and buried interfaces at various mesoscopic to microscopic length scales in the same experiment.

4.4 Measurement of Diffracted x–rays

4.4.1 Area Detector

The area detector configuration enables rapid collection of scattered data from a large range of scattering angles while compromising on resolution and accuracy. The area detector is usually a charge–coupled detector (CCD) array, gas proportional counter array or an image plate. In this thesis, only CCD arrays have been used as a detector. The collimated beam interacts with the film sample and the area detector "takes a picture" of the scattered x–rays. Since a large number of scattering angles are collected simultaneously, the area detector configuration can capture rapidly scattered data from exposures that are often less than a minute long. The time of exposure to capture data depends on the type of detector used, the intensity of the source, the thickness of the

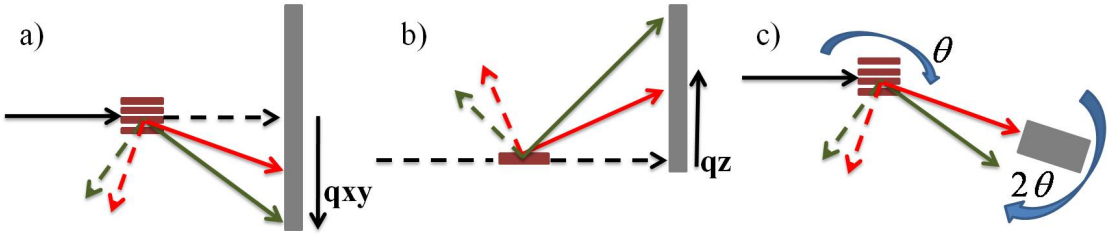

Figure 4.4: Common geometries for GIXD assuming a horizontal angle sample. (a) Top view and (b) side view of two dimensional detector geometry illustrating how the orientation of the scattering vector, **q**, (dashed arrow) varies with the scattering angle. (c) Top view of the point detector geometry illustrating how the sample is rotated at half the angular velocity of the detector to maintain the scattering vector at a constant in–plane sample orientation.

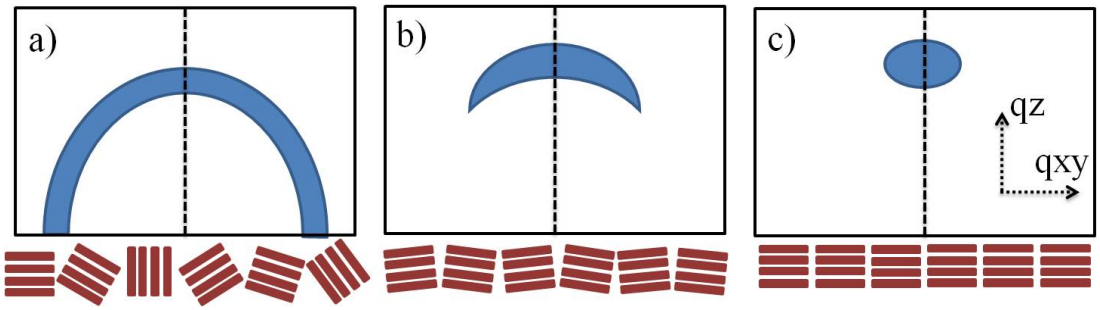

Figure 4.5: Illustrations of example diffraction patterns for different microstructures. (a) Randomly oriented films produce a sharp ring, (b) oriented films with broad orientation distribution produce an arc, and (c) highly oriented films produce an ellipse. The crystal orientation distribution that produced the pattern is shown below each pattern.

film being investigated and crystalline quality of the film being investigated. The quick measurements reduce the effects of beam damage and allow time–resolved measurements such as in–situ drying or in–situ heating. The resolution of the scattering angle is primarily determined by the size of the illuminated area of the sample relative to the distance between the sample and detector. Illumination over a large area produces conditions where x–rays diffracted at different spots on the sample with the same scattering angle will hit different pixels on the detector and x–rays diffracting from different spots on the sample with different scattering angles can hit the same pixel. This results in significant peak broadening and poor resolution.

Another significant limitation of the area detector in GIXD configuration arises from the fixed incidence angle and sample orientation (Figure 4.4 a,b). Specular scans solely along q_z with $q_{xy} = 0$, are impossible to collect in this geometry as the specular condition $\alpha_i = \alpha_f$ is satisfied only in one point in the detector. So this method of scattered data collection does not measure the diffraction of planes parallel to the substrate. The

apparently out–of–plane data on the area detector obtained through the vertical section through the beam center are not specular diffraction; the measured planes can deviate from a few, up to ten degrees from perpendicular within the substrate. This deviation increases with increasing scattering angle and is approximately equal to half of the scattering angle (assuming incidence angles $<<$ scattering angle). A similar problem occurs with the in–plane sample orientation for films with a high degree of in–plane orientation (such as single crystals or aligned films). However, this problem is irrelevant for films with isotropic in–plane orientation [111–113].

Usually polymer–based organic electronics do not have sufficient number of peaks to uniquely solve the full unit cell but only interplanar spacings can be obtained. Since the direction of the reciprocal lattice vectors are defined by the crystallographic planes, the diffraction pattern reveals the orientation of the diffracting crystals. For a film with isotropic crystal orientation, the diffraction will result in a uniform ring on the detector (Figure 4.5 a). For a film with a preferred out–of–plane orientation and isotropic in–plane orientation, the diffraction pattern will consist of spots for each crystallographic plane for a narrow orientation distribution and arcs for a broader orientation distribution (Figure 4.5 b,c). For a biaxially oriented film (e.g. having two distinct orientation axes and out–of–plane orientation with orientation in–plane), only a small number of diffraction spots (or none at all) will show up for a given sample rotation angle, because the sample must be rotated such that the Bragg condition is met. The integrated intensity of a diffracted spot is proportional to the amount of crystalline material in the x–ray beam. In principle, this integrated intensity can be used to calculate the absolute film crystallinity. The relative crystallinity can be obtained by integrating over all orientations the diffraction of the chosen peak. For a line–scan measurements such as the typical specular scan done on a lab source with a point detector, an observed difference in peak intensity does not necessarily indicate that the crystallinity is different; the line scan only measures the scattered intensity for one specific scattering vector orientation (typically normal to the sample plane). Any difference in scattering intensity could also arise from a difference in the orientation distribution. A film in which the crystals shift from randomly oriented to highly aligned with respect to the surface normal would exhibit a substantial increase in the scattering intensity in a specular scan, even if the crystallinity remained the same. To definitely determine a change in crystallinity, a pole figure, or the orientation distribution function that measures the diffraction intensity of one specific diffraction peak as a function of all sample orientations must be obtained. In this thesis, the two dimensional area detectors used were round MAR–CCD detectors.

4.4.2 Point Detector

In the point detector configuration (Figure 4.4 c), a detector with collimating slits is positioned at one specific scattering angle and the collimating slits allow x–rays with only this specific scattering angle to reach the detector. The point detector provides high accuracy and high resolution which allow the accurate determination of the film reciprocal lattice vectors and the diffraction peak width, which in turn are related to the film defect densities. The primary limitation of the point detector is that the measurement is slow because each scattering angle and direction must be separately measured. Due to time limitations and beam damage from the long exposure times, only a small fraction of the reciprocal space volume is measurable. Much lower background and better resolution allow cross–checking of some of the data collected using MAR–CCD detector with point detector at ANKA synchrotron.

4.5 Scanning Probe Microscopes

4.5.1 Atomic Force Microscope

Atomic Force Microscope (AFM) (Figure 4.6) is a method that uses a sharp (typical radius of curvature ~ 5 nm) tip attached to a probe called cantilever with elastic constant K to scan across the sample surface at small distances to obtain a high–resolution topographical map. A piezoelectric scanner is either moving the tip across the sample or the sample across a fixed tip. Deflections of the cantilever, arising from interaction forces between the sample and tip are usually measured by focusing a laser beam on the cantilever. The reflected beam from the top side of the cantilever is collected by a position sensitive photodiode. However, as soon as the tip "feels" a force, there will be a deflection of the cantilever. As a result, the reflected laser beam is changing its position on the photodiode generating now a different photocurrent. If the photodiode contains four independent segments it is possible to distinguish between deflection and torsion of the cantilever. In response to the normal force F_z the cantilever is bending down in z direction according to Hook's law $F_z = K\Delta z$ inducing a vertical displacement Δz. Torsions, however, lead to a lateral movement of the reflected laser beam on the photodiode. The tip–sample force as a function of distance does not follow a monotonic behaviour which makes it difficult to operate the AFM with a stable feedback loop. Thus, different modes are present to overcome this difficulty which basically can be divided into contact mode and dynamic (resonant) modes. For organic electronic films, it is most common to use a resonant mode, where the tip taps on the surface of the film at a few hundred kHz. Resonant modes reduce the lateral shear that occurs as the tip

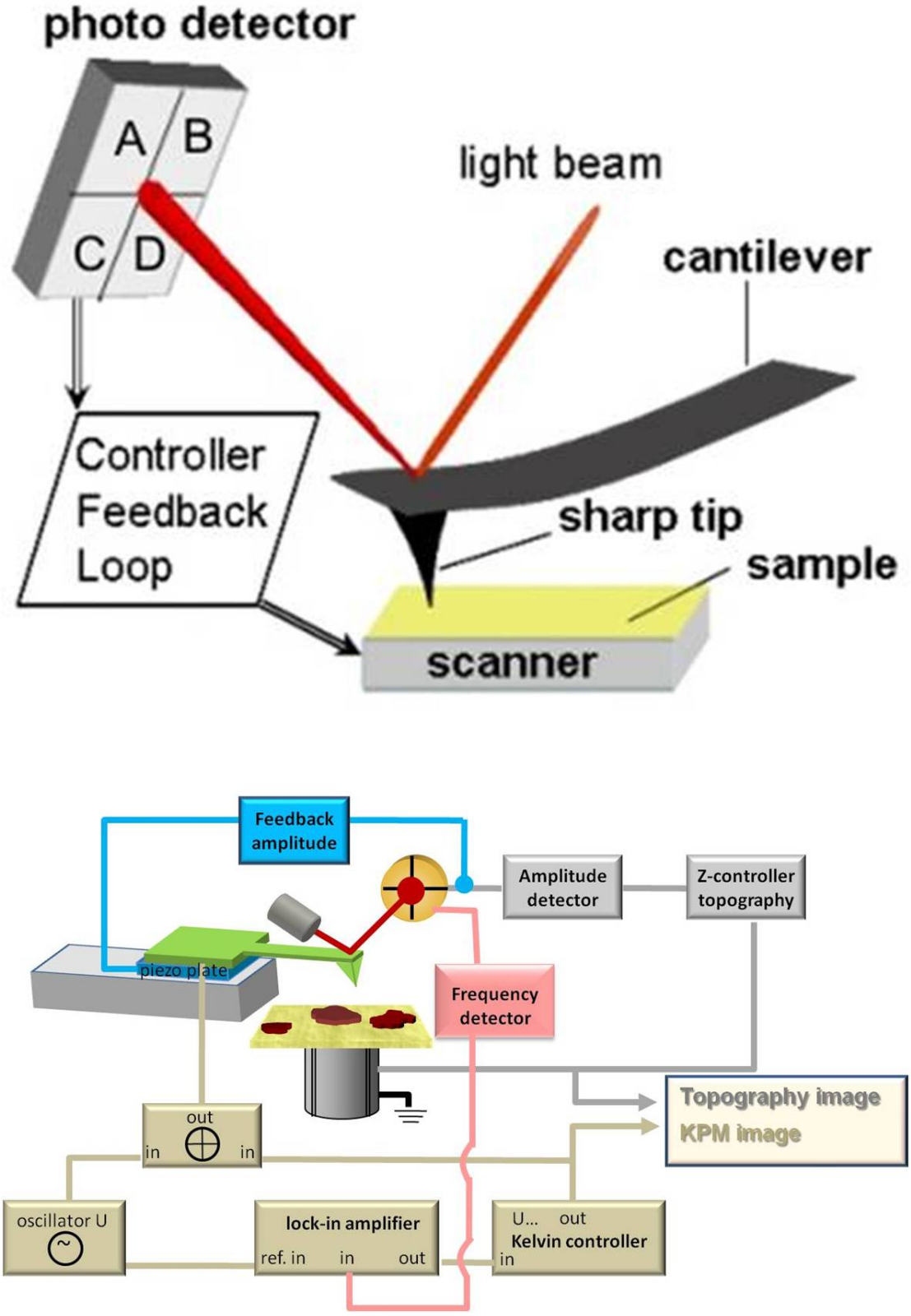

Figure 4.6: Schematic diagram of the Atomic Force Microscope is shown on the top and of the Kelvin Probe Microscope is shown in the bottom.

moves across the surface of the film. Resonant modes can provide additional information about the surface composition through phase imaging and harmonic analysis. The image obtained from AFM is a convolution of the shape of the tip with the shape of the sample. If the sample features are sharper than the tip, the image is merely an image of the tip. Detailed discussion on AFM can be found elsewhere [114–116]

4.5.2 Kelvin Probe Microscope

Kelvin Probe Microscopy (KPM) (Figure 4.6) allows the quantitative measurement of the surface potential with nanoscale resolution, by mapping the electrostatic interaction between a conductive tip and the sample during the scan. The principle of the technique relies on the fact that when two metallic electrodes (tip and sample) are electrically connected, their Fermi levels align and an electrostatic force arise between them due to the difference in work functions. The feedback of the KPM system nullifies this force by applying a voltage between tip and sample. The magnitude of the voltage at which the force is zero is the surface potential. Though the working principle of the KPM is well established the interpretation of the obtained data is not straightforward for non–metallic samples. For metallic samples, the surface potential is the work function difference between the sample and the tip. In the case of semiconductors (organic or inorganic) surface polarizability and band bending effects might influence the surface potential measured. Any change in the vacuum level due to the presence of dipoles or accumulation of charges can be investigated with KPM. Detailed discussion on KPM can be found elsewhere [114–116].

CHAPTER 5

Experimental set–ups used

This chapter contains description of the different materials used, techniques used to prepare different substrates and the different experimental set–ups used in the framework of this thesis.

5.1 Substrate and P3HT: PCBM blend preparation

Commercially available glass substrates were cleaned by sonication in acetone followed by isopropanol for 10 minutes respectively and subsequently treated with oxygen plasma for 2 minutes. The Poly (3,4-ethylenedioxythiophene): poly (styrenesulfonate) (PEDOT:PSS) dispersion (batch – VPAI4083) was purchased from H.C. Starck, Germany. After sonicating the dispersion for 10 minutes, it was filtered with a 0.45 μm filter and then diluted 1 : 1 by volume with water. A layer of PEDOT:PSS was cast on oxygen plasma treated glass substrates by doctor–blading with a slit width of 70 μm and coating speed of 5 mm/s resulting in 20–40 nm dry film thickness. We shall refer to these substrates as PEDOT:PSS/Glass. Some PEDOT:PSS/Glass substrates were coated with a thin layer of indium tin oxide (ITO). They will be referred to as PEDOT:PSS/ITO/Glass.

The silicon substrates (35×35 mm^2) used had about 4 nm silicon dioxide on top. They were cleaned by sonication in acetone and isopropanal followed by an oxygen plasma treatment for 120 seconds.

P3HT used had molecular weight $\approx$ 48900 g/mol, polydispersity $\approx$ 1.7 and was purchased from Rieke Metals. PCBM used had molecular weight 990 g/mol, and was purchased from Solenne. Different weight ratios of P3HT and PCBM such as 1 : 2, 2 : 1 and 1 : 0.8 were dissolved in 3 weight–% solid fraction of solvent DCB and were left overnight at 40°C.

The density of polymer/fullerene solutions was determined with Anton Paar DMA 4500 density meter. P3HT and PCBM solution in DCB was deposited in front of the coating knife and a wet film was cast evenly underneath the knife–edge. This method of film coating is known as doctor–blading. Doctor blading is a coating technology where a knife homogeneously spreads ink (in this case, P3HT: PCBM blend solution in DCB) as the blade is drawn over a substrate. The parameters that determine film formation are the concentration (determining the viscosity of the ink), the temperature of the solution, the speed of the blade, and the distance between the blade and the substrate (i.e. the volume of the blend being deposited). Dry film thickness were measured with a Veeco Dektak M6 surface profiler with a 12.5 μm stylus. The substrate and blend preparations were done in the Karlsruhe Institute of Technology.

5.2 New set–up to study real–time in–situ GIXD during P3HT: PCBM blend drying

For the real–time investigation of the crystallization of the polymer/fullerene solution, a drying channel with an integrated doctor–blade having slit width of 70 μm and a constant knife speed of 5 mm/s was constructed at the Karlsruhe Institute of Technology (Figure 5.1). It has an aluminum window, which is transparent to x–rays, to allow GIXD measurement. The scattered x–rays were collected using a two dimensional MAR–CCD area detector allowing the study of the structural evolution in real–time during drying (Figure 5.2) at a previously adjusted temperature and airflow rate. Additionally, to monitor the in–situ drying kinetics, laser light of wavelength 633 nm was reflected from the film under an incidence angle of 30° and detected by a silicon photodiode during coating and drying of the wet solvent–blend film. Laser and photodiode were mounted on the channel cover. At the air/film interface reflected light interfered with light that was reflected at the film/substrate interface enabling thickness measurement of the film. The deposited wet solvent–blend film was dried using air or nitrogen that flowed through the drying channel. The drying gas and the substrate holder were liquid temperature controlled with a Lauda RC6 cryostat. The airflow speed of the drying gas was measured in front of the substrate holder by a mountable hot–wire anemometer, which was removed after the measurement. For interference analysis conducted at the Karlsruhe Institute of Technology, the composition dependent refractive index of the polymer/fullerene solution was determined from concentration series using a Kernchern refractometer at 589 nm enabling the thickness of the blend film to be recorded during in–situ drying [118].

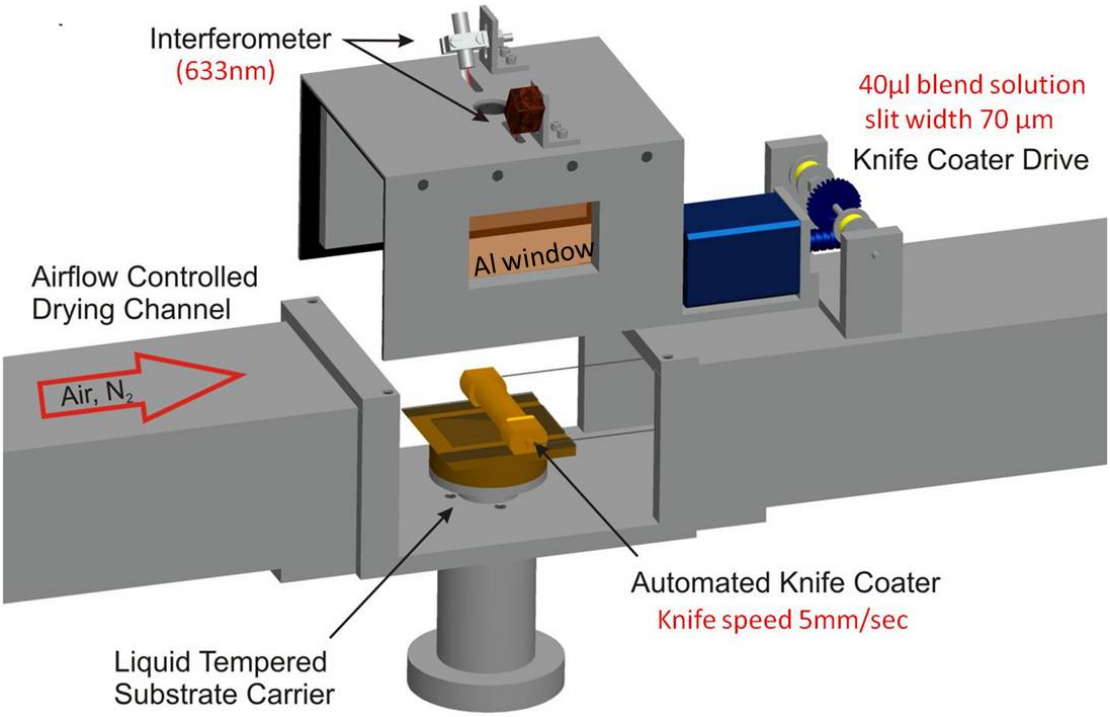

Figure 5.1: Schematic diagram of the drying channel with an integrated doctor–blade and optical interferometer. The optical interferometer is mounted on a cover with thin aluminum walls, practically transparent to x–rays, enabling simultaneous in–situ GIXD and interferometry of P3HT: PCBM blend films processed from solution.

5.3 Synchrotron Beamlines

This section contains concise description of the beamlines MPI–MF at the synchrotron Ångstrϕquelle Karlsruhe (ANKA) and the ID–10B at the European Synchrotron Radiation Facility (ESRF); these beamlines were used in the work discussed in this thesis.

5.3.1 MPI–MF Surface Diffraction Beamline at ANKA

The synchrotron ANKA has a storage ring operating at energy 2.5 GeV with current 200 mA. The beamline is a multi–purpose bending magnet beamline with optics containing a rhodium coated silicon mirror for cutting the energy spectrum and for vertical beam focusing. A Si(111) double crystal monochromator adjusts the energy within 6 to 20 keV with an energy resolution of 10^{-4}. The multi–circle $(2+3)$ diffractometer can house different ultra high vacuum chambers and detectors allow vertical and horizontal diffraction geometry for the experiments. The ex–situ experiments on dried P3HT: PCBM blends were conducted in this beamline with sodium iodide scintillation counter as the point detector and a round two dimensional MAR–CCD camera of di-

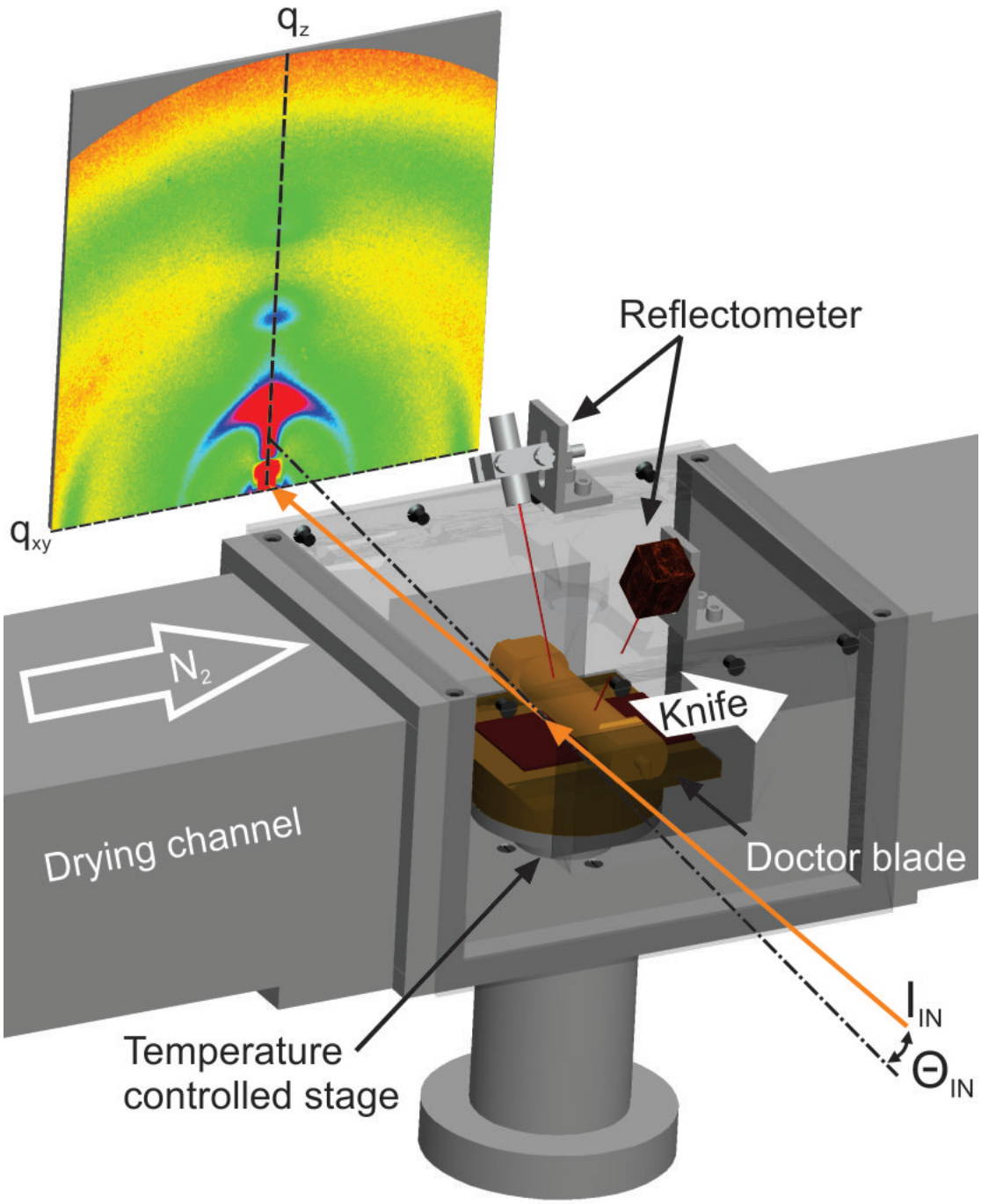

Figure 5.2: Schematic diagram of the experimental set–up for simultaneous measurement of real–time GIXD and laser interferometry on doctor–bladed P3HT: PCBM blend films in a controlled drying environment [117].

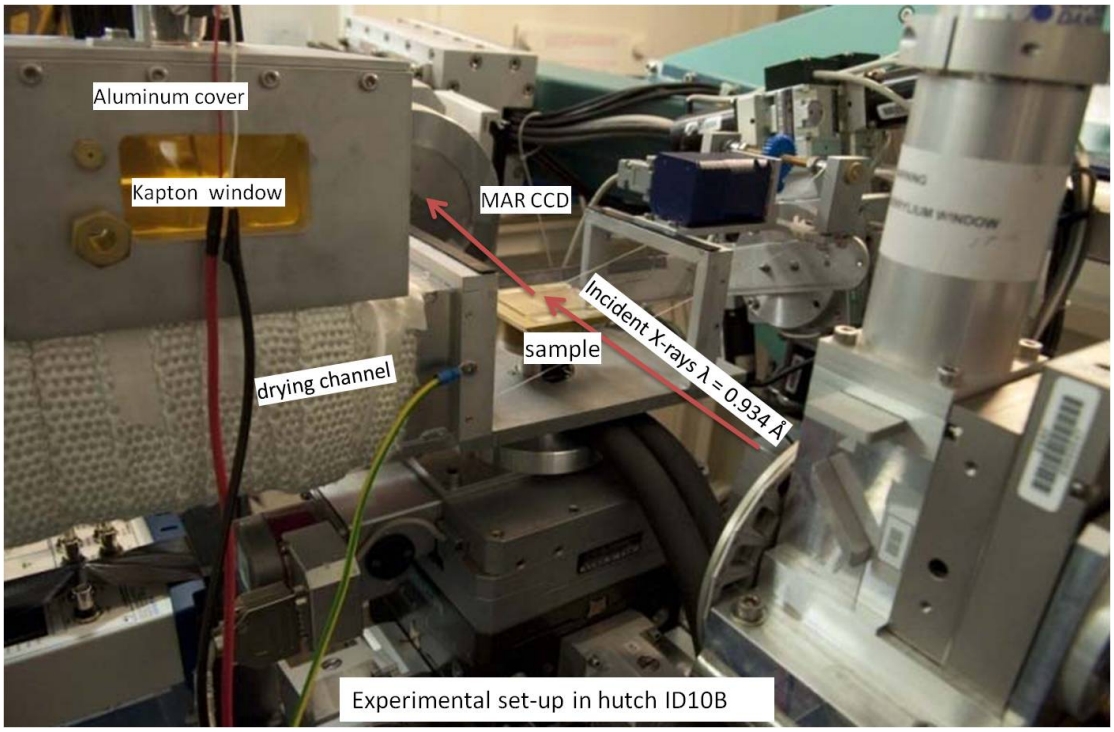

Figure 5.3: Photo of the experimental set–up in the ID10B surface diffraction beamline at ESRF to study in real–time the in–situ structural evolution using GIXD of P3HT: PCBM blend from solution.

ameter 165 mm was used as the area detector. Each pixel size of the used MAR–CCD detector was 80 μm and there were 2048$\times$2048 pixels in each image.

5.3.2 ID–10B at ESRF

The ESRF operates a storage ring with energy 6 GeV and current of 200 mA. The ID–10B beamline is a multipurpose, high brilliance undulator beamline and is dedicated for high resolution x–ray scattering and surface diffraction on solid and liquid surfaces and interfaces, combining GIXD and x–ray reflectivity. Its optics consists of a diamond (111) and (220) double crystal monochromator with an intrinsic energy resolution $\frac{\Delta E}{E}$ of 5.9×10^{-5} and 2.3×10^{-5} respectively. The energy can be tuned from 8 to 13 keV with the (111) face and from 13 to 22 keV with the (220) face of the crystal diamond. In order to suppress higher harmonics a double–mirror set–up is installed. The diffractometer is able to perform scattering experiments in both horizontal and vertical scattering geometry. The experiments involved in the real–time *in–situ* study of the structural evolution of P3HT: PCBM blend in real–time during the drying of the P3HT: PCBM blends were conducted in this beamline using a round two dimensional MAR–CCD camera of diameter 133 mm as the area detector. The experimental set–up used in this thesis is shown in the photo in Figure 5.3. Each pixel size of the used MAR–CCD detector was

65 μm and there were 2048$\times$2048 pixels in each image.

5.4 Solar Cell Fabrication

Some preliminary investigations of solar cells were conducted with the blend of P3HT and PCBM in DCB. The blend was doctor–bladed on top of PEDOT:PSS/ITO/Glass substrates followed by vapor deposition of calcium of thickness 50 nm and aluminum of thickness 150 nm. For solar cell fabrication, structured ITO glass slides (50 $\times$ 50 mm^2) were cleaned with toluene, acetone and isopropanol by sonication. 35 nm thick PEDOT:PSS layer was cast by doctor–blading and heated at 120°C for 20 minutes in a glove–box. The current–voltage–characteristics were measured under spectrally monitored ORIEL solar simulator without post–annealing the active layer. Solar cell fabrication was conducted in the Karlsruhe Institute of Technology.

5.5 Ultra–High Vacuum System

In addition to solvent drying growth of thin films of P3HT, preliminary investigation of topography and surface potential of these films have been conducted in ultra–high vacuum (UHV) immediately after their formation and transporting them in vacuum. The Ultra–High Vacuum (UHV) System (Omicron, Germany), shown in Figure 5.4 has three chambers — the load lock, the deposition chamber and the analysis chamber, all connected by a transfer system which allows substrate movement to all parts of the chamber without breaking the vacuum. The load lock system ensures a fast insertion of substrates and can be pumped down to a pressure of 10^{-6} mbar within one hour. The deposition chamber has four Knudsen cells for controlled deposition of molecules on substrates, a quartz crystal micro–balance to measure the thickness and deposition rate of molecules to form films and C– or K– type thermocouples to measure the evaporation temperature. The analysis chamber contains a combined AFM/STM system for the characterization of different film surfaces. The base pressure of the growth and analysis chamber can go down to 10^{-10} to 10^{-11} mbar with a combination of turbo–molecular pumps, ion–pumps and titanium sublimation pumps. All three parts of the system can be sealed from each other to maintain low pressure in the respective chambers.

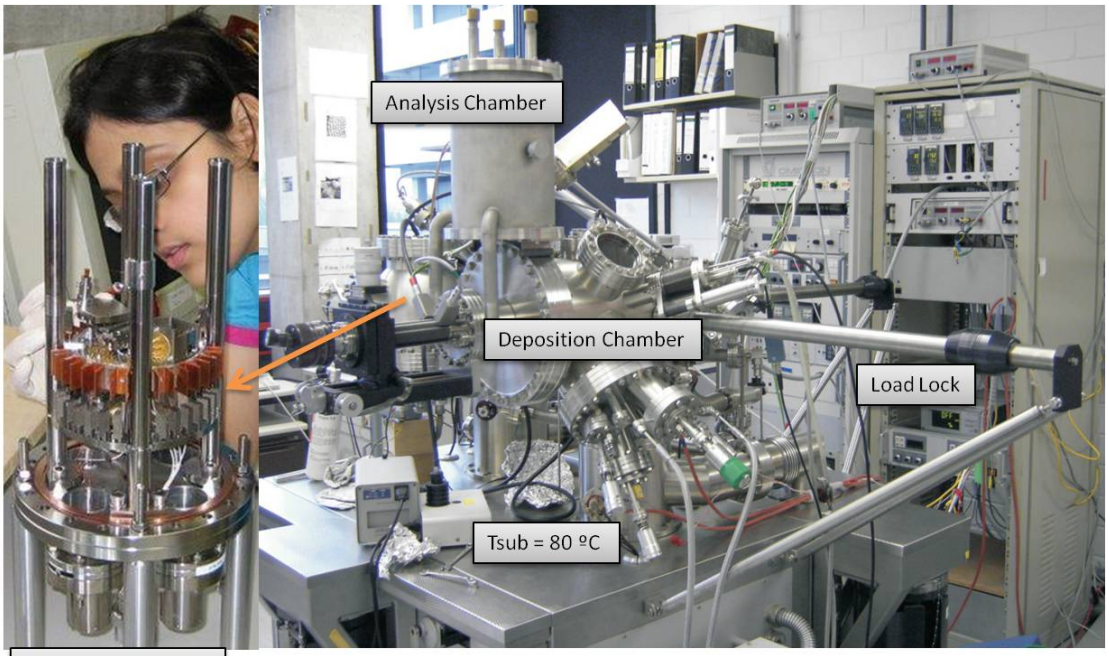

Figure 5.4: The AFM/KPM unit inside the analysis chamber of the UHV system of the OMBD is shown on the left and the entire OMBD system is shown on the right.

5.5.1 Atomic Force Microscope

The Atomic Force Microscope (AFM) system that was previously installed in the analysis chamber of the UHV OMICRON system was upgraded to include Kelvin Probe Microscope (KPM). The primary aim of the KPM was to study the change of surface potential when light is incident on the photo–sensitive P3HT: PCBM blend. However before using KPM for P3HT: PCBM it was tested on surfaces of known substrates and films. All the measurements in AFM and KPM were performed in UHV at a pressure $p < 10^{-10}$ mbar. The topography was measured using the standard frequency modulation technique at the first resonance frequency of the cantilever ($\sim$70 kHz). For KPM measurements, frequency modulation detection with an ac bias amplitude of 500 mV peak–to–peak voltage was used. For all measurements, chromium/platinum coated silicon cantilevers purchased from Budgetsensors were used (Figure 5.5).

5.5.2 Kelvin Probe Microscope

During measurement of the films of P3HT, PCBM and of the blend film P3HT: PCBM with ratio 1 : 0.8 (Figure 5.5) on PEDOT:PSS/ITO/Glass substrates, the nullifying voltage had been applied to the sample while the tip had been grounded. The higher sur-

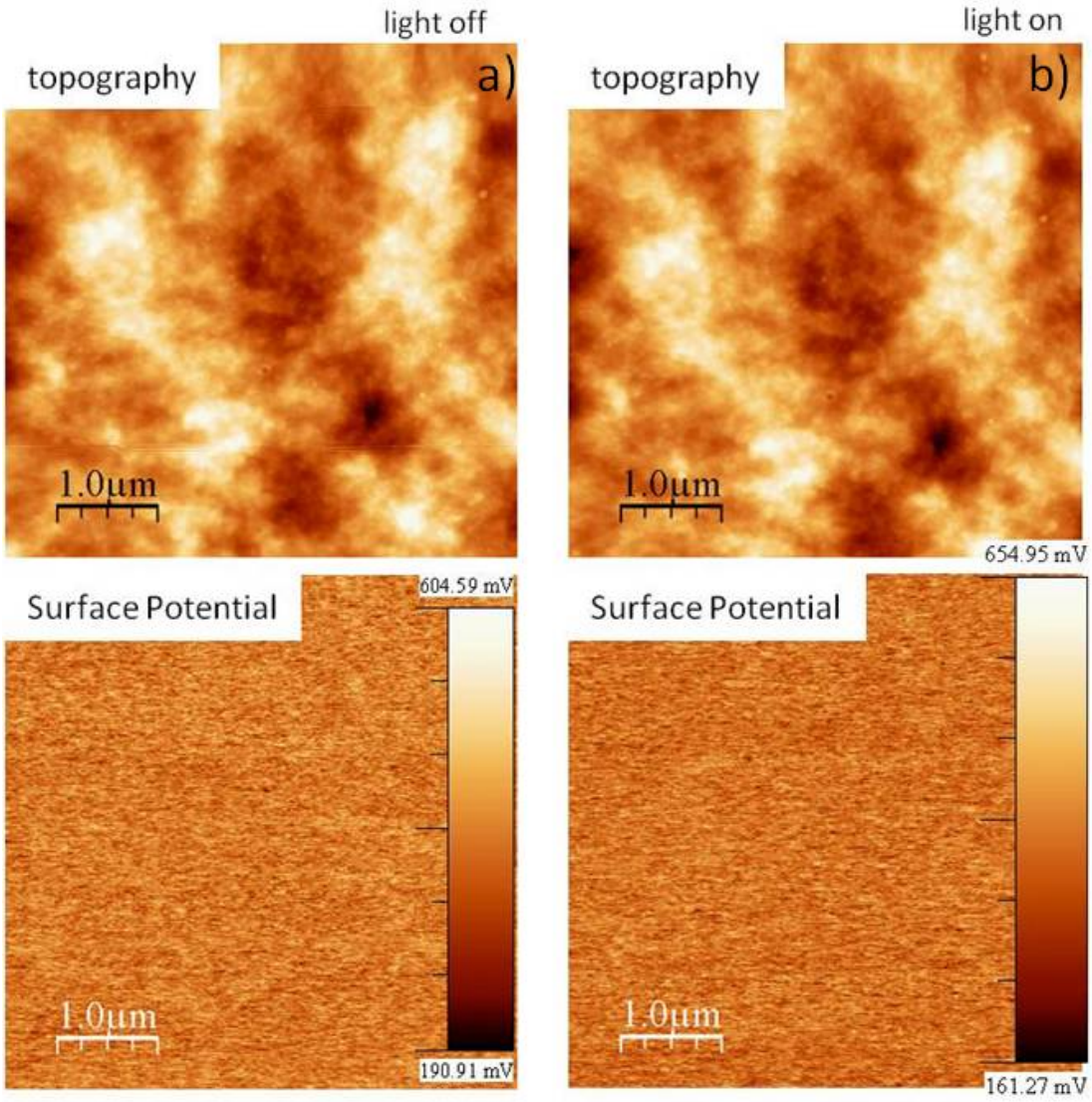

Figure 5.5: Topography (top), surface potential (bottom) of P3HT: PCBM blend on PEDOT:PSS/ITO/Glass in light off (a) and light on (b) conditions.

face potential values were the brighter regions in the KPM image; hence the brighter regions give a map of the negatively charged regions on the film as areas with higher work function have accumulation of negative charges. Figure 5.6 shows that with incident white light, both P3HT: PCBM blend (Figure 5.6 a) and P3HT (Figure 5.6 b) show decrease of average surface potential. As PCBM is not photosensitive, it does not show any change in surface potential in both conditions (c). The holes in the film have transported to the ITO and have been removed from the film. Further experiments and further analysis must be conducted in order to draw any conclusion on the surface potential behavior of different films.

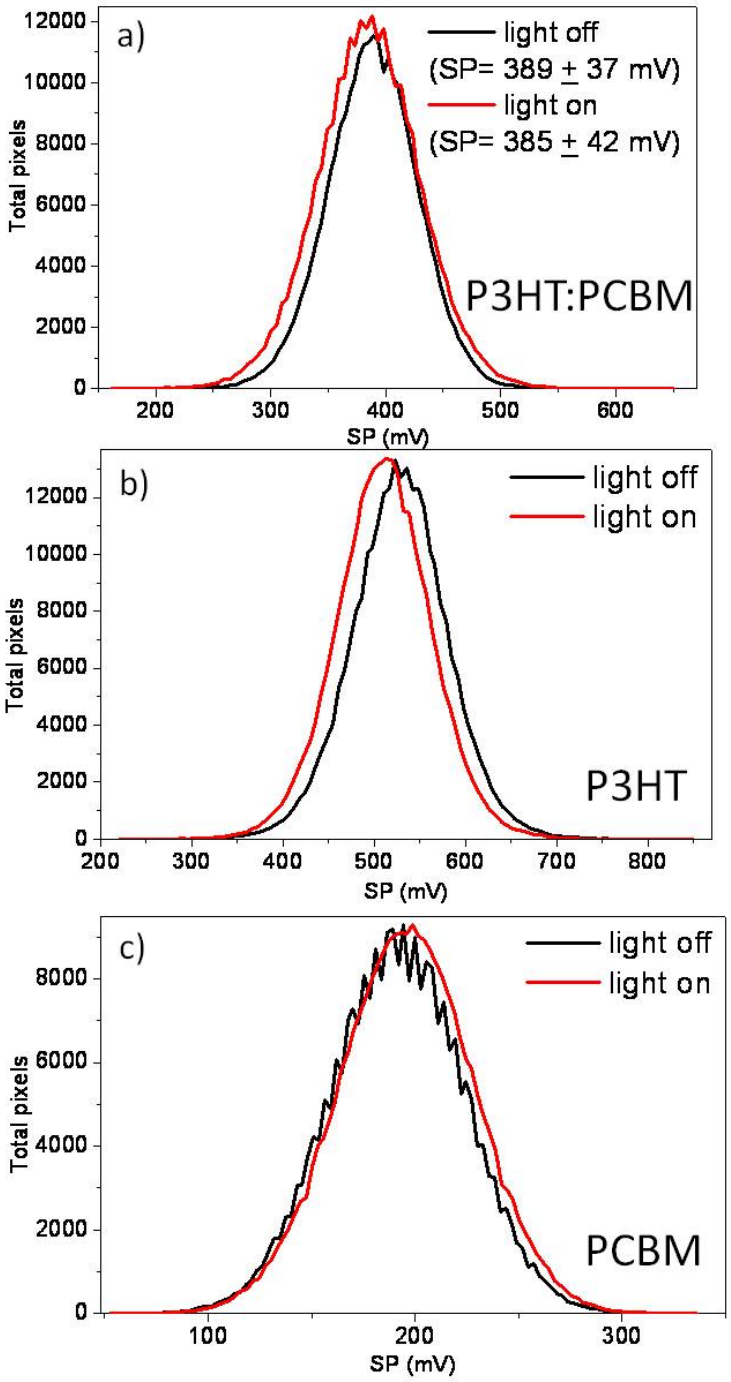

Figure 5.6: Average surface potential of (c) P3HT: PCBM (d) only P3HT and (e) only PCBM film in the light on (red) and light off (black) conditions.

CHAPTER 6

Real time investigation of in–situ drying of P3HT: PCBM blend

6.1 Introduction

In this chapter, real–time GIXD study has been combined with optical reflectometery to follow the evolution of structure and thickness of polymer–fullerene–solvent blend as the solvent evaporates. Furthermore, analysis of x–ray diffuse scattering from the polymer–fullerene–solvent blend has, for the first time, been applied to determine the evolution of the elastic constants of the P3HT: PCBM blend during crystallization. This is a powerful experimental approach to advance the microscopic understanding of the nanoscale phase separation in bulk heterojunction polymer/fullerene blends during solidification from the solvent.

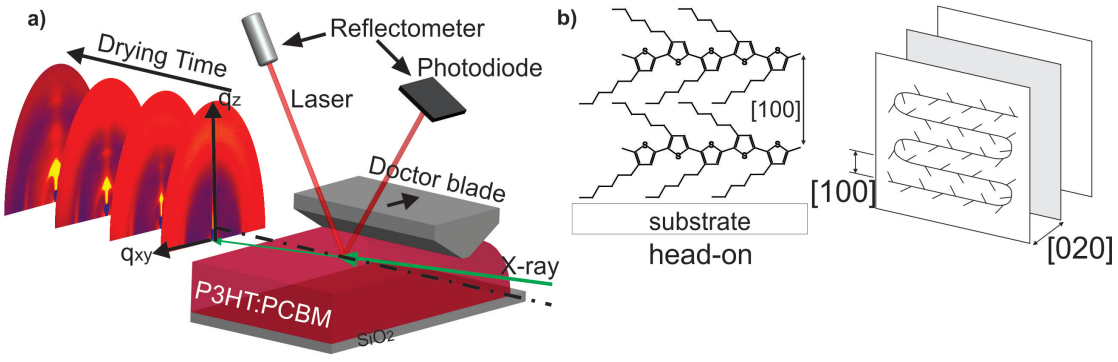

Figure 6.1: (a) Schematic diagram of the experimental set–up to study the in–situ drying of P3HT: PCBM blend using GIXD and laser interferometry (b) Chemical structure of P3HT

6.2 Experimental Details

The GIXD study (Figure 6.1) was carried out with energy 12.3 keV at the ID–10B beamline in ESRF. This experiment has been performed using blend ratio 1 : 0.8 and solvent DCB (see chapter 2 for details for choosing this blend ratio). To measure the structural evolution instantly after film coating, the temperature controlled drying channel with an integrated doctor–blade was used (see chapter 5 for detailed description of the drying channel). The P3HT: PCBM solution in DCB was homogeneously spread on a clean silicon substrate with native silicon oxide (temperature held constant at 25°C) by the doctor–blade. Instantly after coating, x–ray scattering data was collected in the MAR–CCD area detector and reflected laser light was collected in the silicon photodiode. (see section 5 for details) GIXD data was taken for 3 seconds, each in interval of 50 seconds, with the two dimensional MAR–CCD area detector (Figure 6.1 a).

6.3 Structural evolution of P3HT: PCBM blend during drying

During drying, the reflected laser intensity shown in the inset of Figure 6.9 exhibited a series of maxima and minima from constructive and destructive interference conditions. The blend solution thickness decreased and acquired a constant value of 250 nm after about 400 seconds when most of DCB solvent had evaporated. The final dried blend, measured with a profilometer, was 178 nm thick — this is below the detection limit of the optical interferometer. Figure 6.2 a to d show the structural evolution of P3HT: PCBM blend during evaporation of the solvent DCB. Due to GIXD geometry, Bragg peaks measured along q_z have small in–plane component, which at P3HT (100) Bragg peak ($q_z = 0.339\,\text{Å}^{-1}$) is $q_y = -0.0078\,\text{Å}^{-1}$ implying a slight underestimation of angular misorientation. Distortion due to planar geometry of the two dimensional area detector has been corrected in all data analysis and has been discussed in chapter 4. In the initial stages of drying, only two broad diffraction rings associated with DCB solvent were visible (Figure 6.2 a) corresponding to spacings of 3.8 Å and 5.6 Å , which disappear in the course of solvent evaporation. The first signature of P3HT ordering was observed after 50 seconds of drying, when the first order pseudo–Bragg peak appeared in the two dimensional MAR–CCD area detector diffraction pattern (Figure 6.2 b). The second and third order Bragg peaks appear after 200 seconds and 250 seconds respectively (Figure 6.2 c). P3HT Bragg peaks along q_z appear split initially as ordering starts at the edge of the sample due to faster drying. In grazing angle of incidence, the entire sample is illuminated. Parallel beam produce two peaks in the two dimensional area detector from crystallized areas at the two sample edges along the beam.

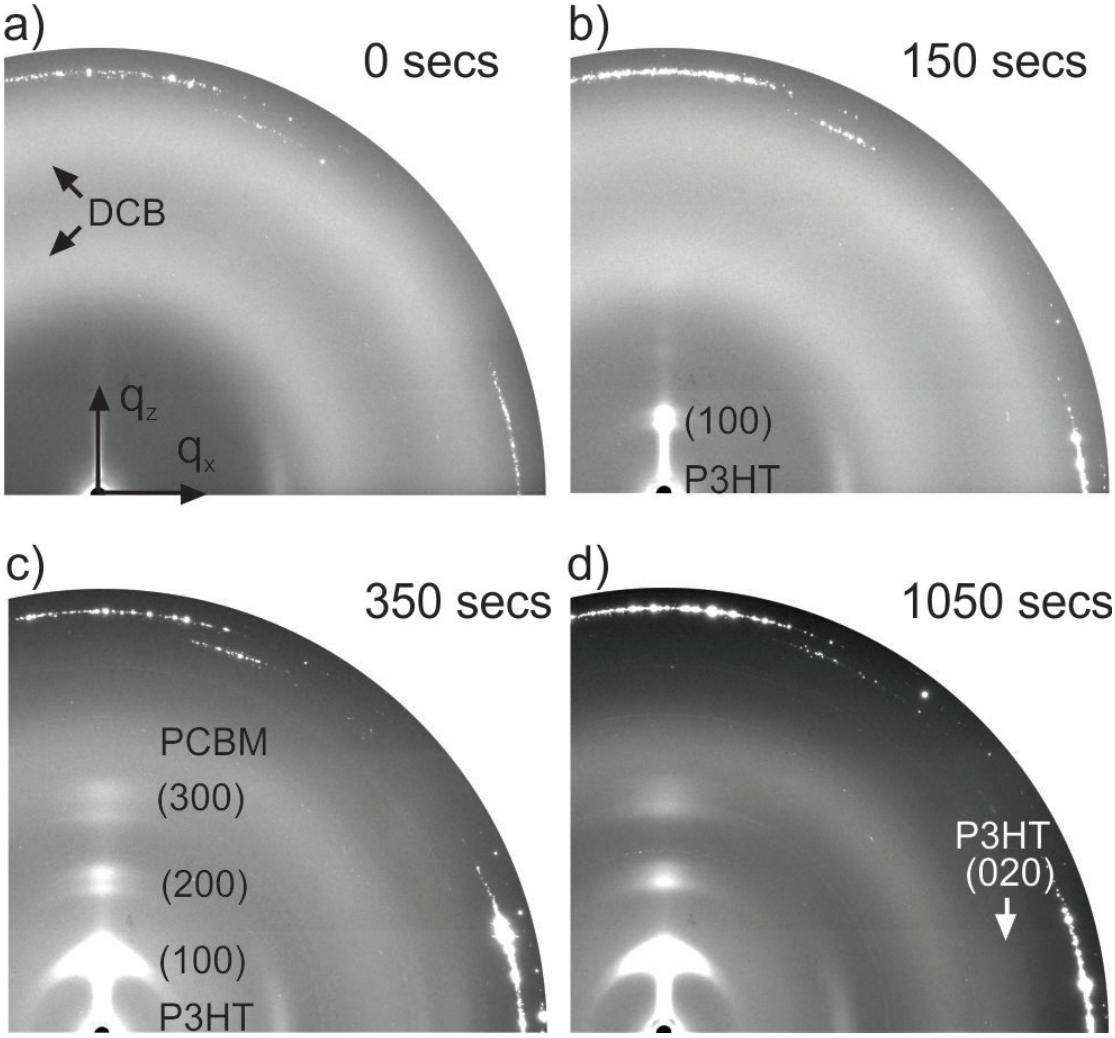

Figure 6.2: Snapshots (a)–(d) of two dimensional x–ray diffraction patterns taken with MAR–CCD area detector of P3HT: PCBM blend (a) just after coating the blend film, (b) when P3HT (100) Bragg peak appears (c) when higher order Bragg peaks appear and (d) final dried blend film.

The splitting becomes negligible as ordering progresses towards the center of the sample. This was confirmed by reducing the beam size so that only the central portion of the film is illuminated. However, we used larger beam size to increase data collection efficiency to enable monitoring of the solvent drying process. The final dried sample is shown in the Figure 6.2 d. The average spacing of 16.5 Å associated with the observed (h00) Bragg peak arises from the lamellar stacking of P3HT backbones (6.1 b) separated by their hexyl side chains with the *a*–axis perpendicular to the substrate. The nearly constant value of the P3HT interlayer spacing during drying process rules out solvent incorporation into the P3HT chains. At about 350 seconds (Figure 6.2 c), a broad diffraction ring corresponding to PCBM emerges revealing the aggregation of PCBM randomly oriented in the blend, with an associated spacing of 4.8 Å and a corre-

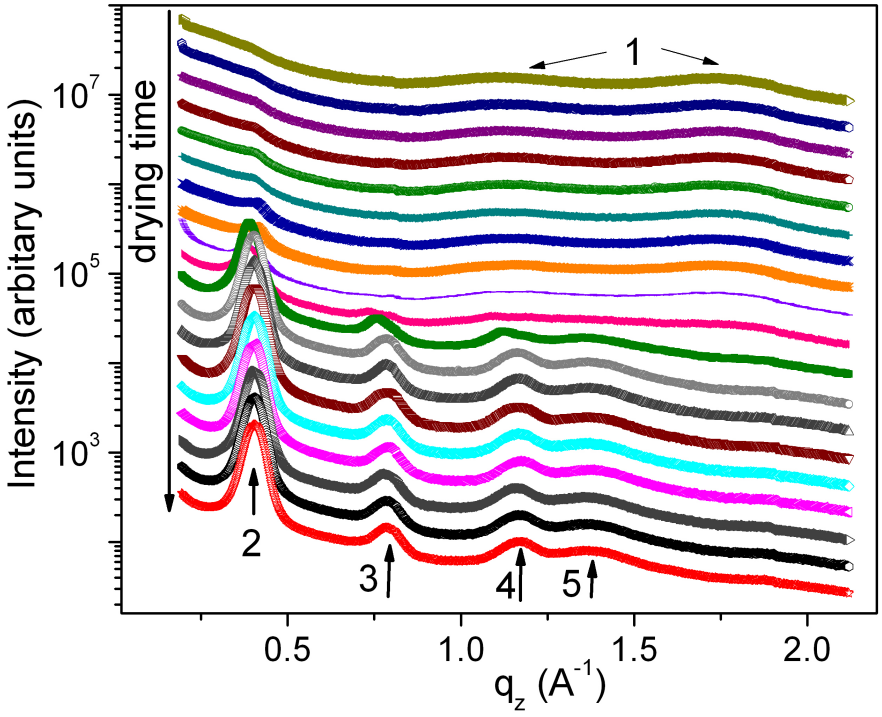

Figure 6.3: Evolution of (1) solvent DCB (2) P3HT (100) (3) P3HT (200) (4) P3HT (300) and (5) PCBM diffraction peaks with drying of solvent DCB. The profiles shown have been scaled along the vertical axis for clarity.

lation length of ~ 20 Å estimated by Scherrer analysis. At 450 seconds, when the film is dried according to optical reflectrometery, a faint (020) peak of P3HT along q_{xy} appears which is a signature of development of short–range ordering within the P3HT layers and is associated with the P3HT π–π interchain stacking. The drying experiment was repeated again under controlled evaporation of solvent by controlling the speed of the air–flow in the drying channel to ensure uniform drying of the film. The line profiles along the q_z direction on the two dimensional area detector frames were taken at different drying times as shown in Figure 6.3. To demonstrate the appearance of PCBM peak during drying, a portion of the line profile from $q_z = 0.4\text{Å}^{-1}$ to $q_z = 2.0\text{Å}^{-1}$ in Figure 6.4. Figure 6.4 also shows the disappearance of the peaks corresponding to solvent DCB, the appearance of PCBM and demonstrates that PCBM crystallizes only during the last stage of solvent evaporation (refer black line corresponding to drying time of 50 seconds). The green profile (after drying of 450 seconds) clearly show the emergence of PCBM peak at $q_z = 1.3\text{Å}^{-1}$. Late appearance of PCBM peak after disappearance of DCB clearly demonstrate that PCBM crystallizes during the last stage of solvent evaporation.

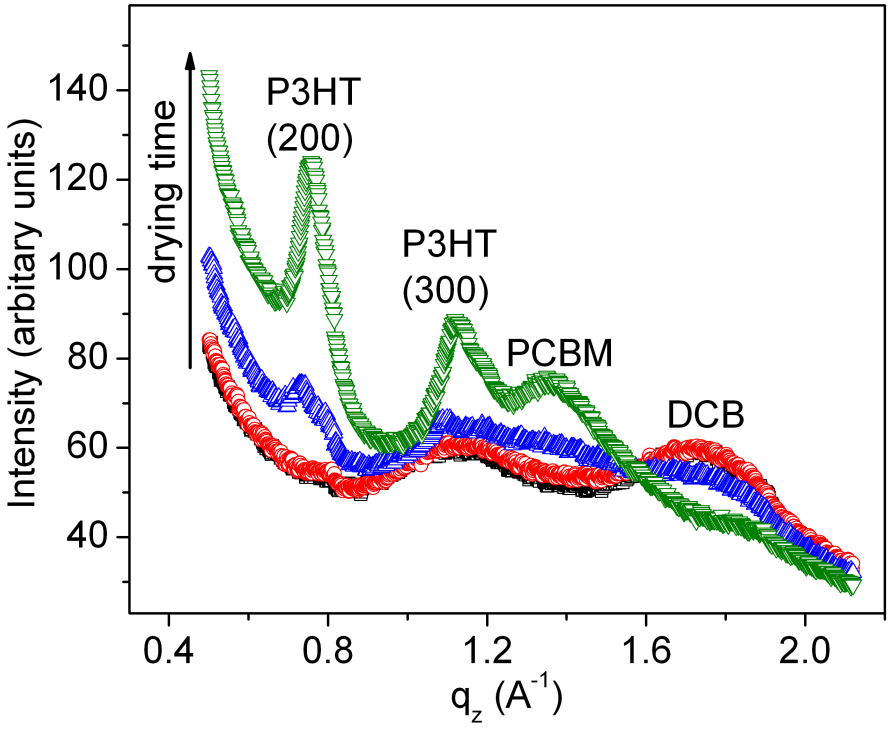

Figure 6.4: Profile plots showing the emergence of the diffraction peaks of PCBM, P3HT (200) and P3HT (300) Bragg peaks with drying of solvent DCB. The plots show that the diffraction peak of PCBM appears after solvent DCB has evaporated.

6.4 Evolution of the elastic constants of P3HT: PCBM blend

Diffuse x–ray scattering analysis along q_{xy} provides further insight into the solidification process as a function of drying time (refer to chapter 4 for details). The liquid crystalline nature of the film becomes evident in the diffuse scattering tail along transverse profiles taken in the two dimensional x–ray diffraction maps obtained from the MAR–CCD area detector at the Bragg peaks along q_{xy}. Strong thermal fluctuations lead to characteristic features in x–ray line shape of liquid crystals calculated by Caille [109] and experimentally observed by Als–Nielsen et. al. [110]. This line shape shows a central Gaussian portion that goes into power-law decay of intensity along q_{xy} with exponent $\eta - 1$ in this geometry [105–107, 110, 119]. The exponent η for liquid crystalline systems is $\eta = \frac{{q_{z0}}^2 k_B T}{8\pi\sqrt{KB}}$ where q_{z0} is the value of q_z at the Bragg position, k_B is the Boltzmann constant, T is the temperature (T = 298K in this case), B and K are the elastic constants associated with the compression and undulation of the layers respectively (Figure 6.6). K and B are related to the penetration depth $\lambda = \sqrt{K/B}$, which is

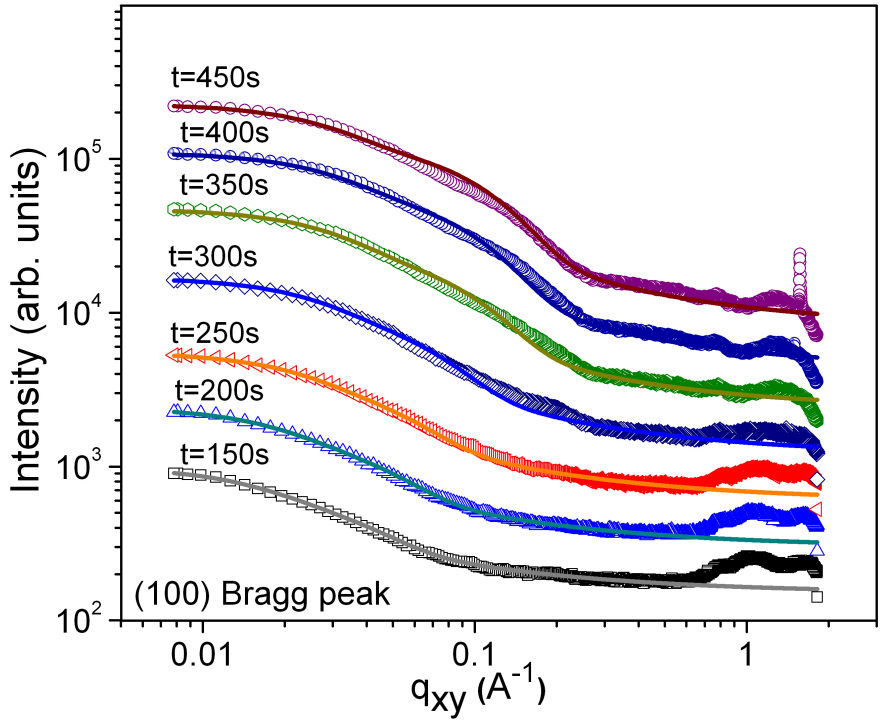

Figure 6.5: Log–log plot of diffuse x–ray intensity versus q_{xy} at (100) P3HT Bragg peak ($q_{z0} = 0.39\text{Å}^{-1}$). Symbols denote data points and the lines are corresponding fits to data.

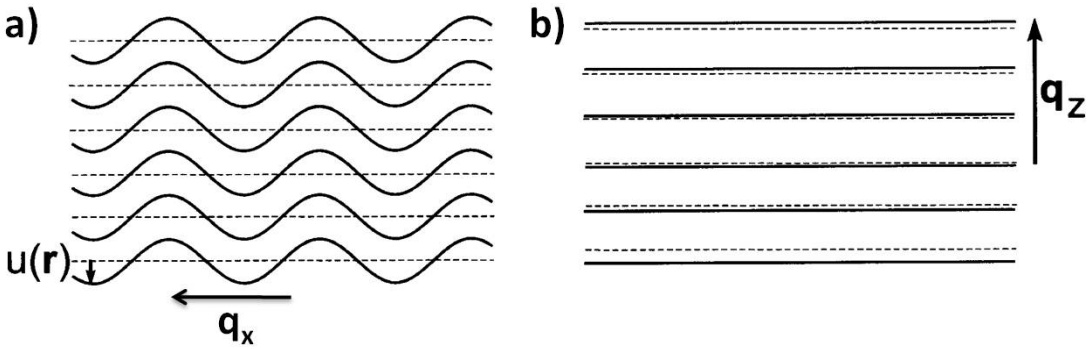

Figure 6.6: Schematic diagram of (a) undulations and (b) compression of smectic layers with the corresponding wave vectors used to define the elastic constant K and B respectively.

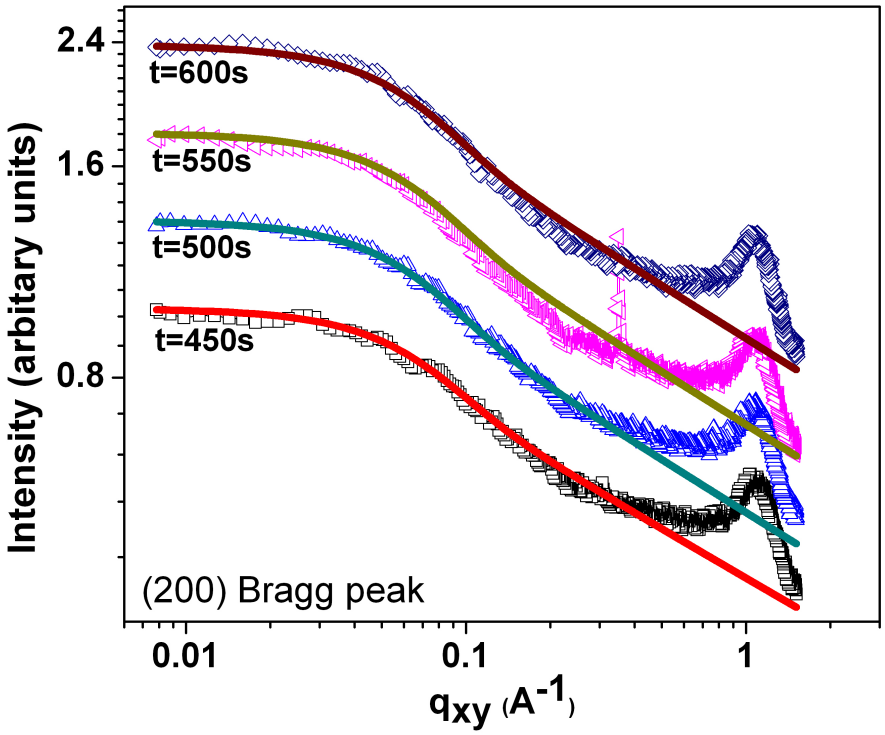

Figure 6.7: Log–log plot of diffuse x–ray intensity versus q_{xy} at (200) P3HT Bragg peak ($q_{z0} = 0.78\text{Å}^{-1}$). Symbols denote data points and the lines are corresponding fits to data.

of the order of layer spacing. λ has been estimated to be the spacing calculated from the x–ray data for each drying time. Hence, the exponent η obtained from the fitted diffuse x–ray intensity directly gives a measure of the time evolution of the elastic constants B and K as the solvent evaporates. The range of data for fitting is limited by the presence of PCBM ring; in addition a spurious ring at $q_{xy} = 0.78\text{Å}^{-1}$ was present originating from the detector window. For verifying the consistency of the extracted η value, the in–plane diffuse scattering at the P3HT (100) peak ($q_{z0} = 0.39\text{Å}^{-1}$) (Figure 6.5) and the (200) peak ($q_{z0} = 0.8\text{Å}^{-1}$) (Figure 6.7) was analysed which confirmed the appropriate scaling of $\eta = \frac{{q_{z0}}^2 k_B T}{8\pi\sqrt{KB}}$. Both the data sets as a function of drying time could be fitted with same value of K and B. The obtained value of B from the fitting of both the data sets are given in Figure 6.8. The results of the q_{xy} line shape analysis for the first (Figure 6.5) and second (Figure 6.7) order Bragg peaks of P3HT are presented in a log–log plot at different drying times. Hypergeometric Kummer function ${}_1F_1[(1-\eta)/2; 1/2; -{q_{xy}}^2(\zeta/2\pi)^2]$ has been used to simplify the fitting of line shape profiles along q_{xy}. The Kummer function has a central Gaussian function followed with power-law decay with exponent $\eta - 1$. The value of η gradually decreased as

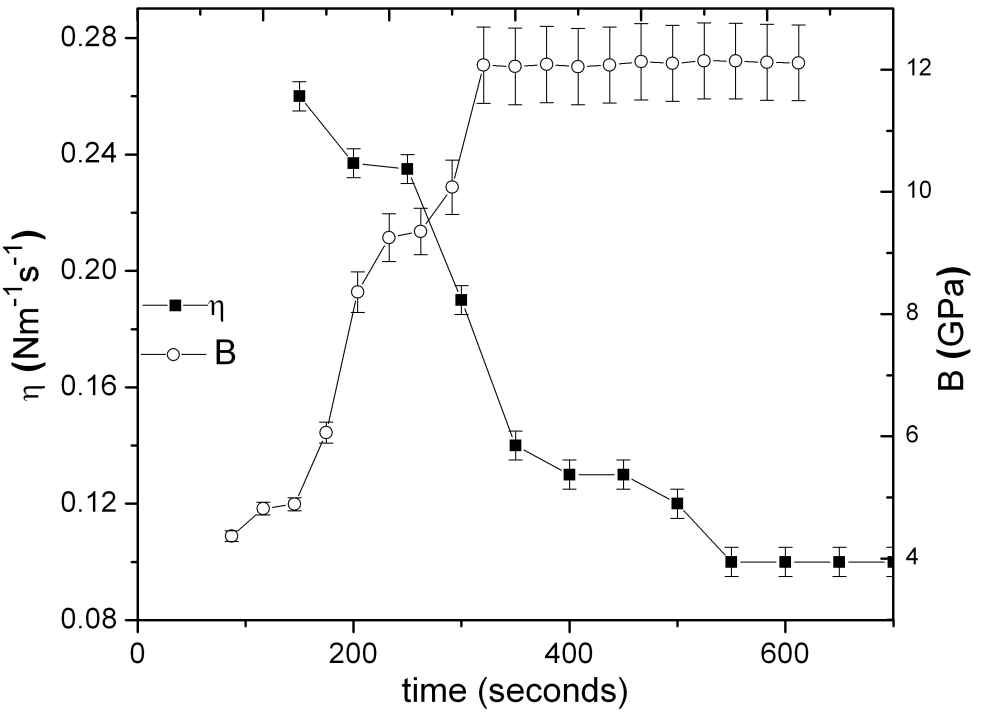

Figure 6.8: Evolution with drying time of the exponent η and the elastic constant B for layer compression calculated from the fit of diffuse x–ray intensity. As solvent evaporates, increase of B provides direct evidence of P3HT solidification.

the solvent evaporated and correspondingly the calculated elastic constants B and K increased (plotted η and B in Figure 6.8) [107]. Therefore P3HT becomes more resistive to lateral and vertical compression with solvent drying time. Also to be noted is that the elastic constants reach the maximum value and η the minimum value when the P3HT third order Bragg peak and the in–plane P3HT (020) peak appear. Hence the evolution of the elastic constants and the structural data provide a consistent picture of a smectic liquid crystalline state, when elastic constants have taken high value (refer Figure 6.8), η becomes negligibly small and the exponent becomes close to 1 as expected for liquid crystalline to solid transition leading to the development of positional ordering within the smectic P3HT layers at $\sim$ 450 seconds.

6.5 Discussion of structural changes during drying

An estimate of P3HT "degree of crystallinity" from the P3HT (100) Bragg peak includes the azimuthal distribution of intensity to take into account all the crystallites oriented

in different directions. So the x–ray scattered intensity is integrated over 180° between two concentric circles containing the P3HT (100) Bragg peak as shown in the inset of Figure 6.9 b and plotted as a function of drying time in Figure 6.9 a. This is referred to as the "(100) crystallinity" to emphasize that it gives information about the "degree of crystallinity" of the ordered layered structure of P3HT in the out–of–plane direction along q_z regardless of the quality of the P3HT π–π interchain packing within the layers in the plane of the substrate along the q_{xy} direction. Also note that the "wing"–like shape of the P3HT (100) Bragg peak increases with drying time. This indicates a larger distribution of P3HT crystallite orientations in the plane of the substrate i.e. the mosaicity of P3HT increases. The time evolution of the angular distribution of orientations of P3HT crystallites with respect to the substrate surface, namely, mosaicity is shown in Figure 6.9 b. The angular spread of the P3HT (100) Bragg peak is fitted to a Lorentzian curve whose full width at half maximum gives a measure of the mosaicity. In the early stages of drying, the P3HT microcrystalline grains have mosaicity of about 6°; as solvent evaporates, there is a larger fraction of misaligned crystallites and the mosaicity increases to 13° at about 450 seconds (Figure 6.10). During this time, emergence of π–π interchain stacking within P3HT layers is also observed and the film is dry according to the laser interferometry measurement shown in the inset of Figure 6.9 a. The emergence of P3HT π–π interchain stacking, with spacing 3.8 Å and correlation length of 60 Å further confirms solidification of P3HT as observed in the previous section. Also the diffraction ring due to PCBM is observed at this time. Gradually, all the solvent evaporates and the mosaicity increases to maximum of 14°. The blend film at this stage is dry. No further structural changes of the P3HT: PCBM blend film is observed.

6.6 Conclusions

In this chapter real–time x–ray scattering data was collected from photoactive P3HT: PCBM blends while it was being processed using doctor–blading. The x–ray scattering data collected during drying has been discussed which gives novel insight into the crystallisation and the associated evolution of the elastic properties of the blend film during the film formation. The blend microstructure has been shown to emerge from liquid crystal to solid phase as the solvent evaporates. This discovery opens the door to a microscopic understanding of the nanoscale organisation in polymer–fullerene BHJ organic solar cells on the basis of the phase and drying behaviour — key for direct control of the nanomorphology for optimised photovoltaic performance.

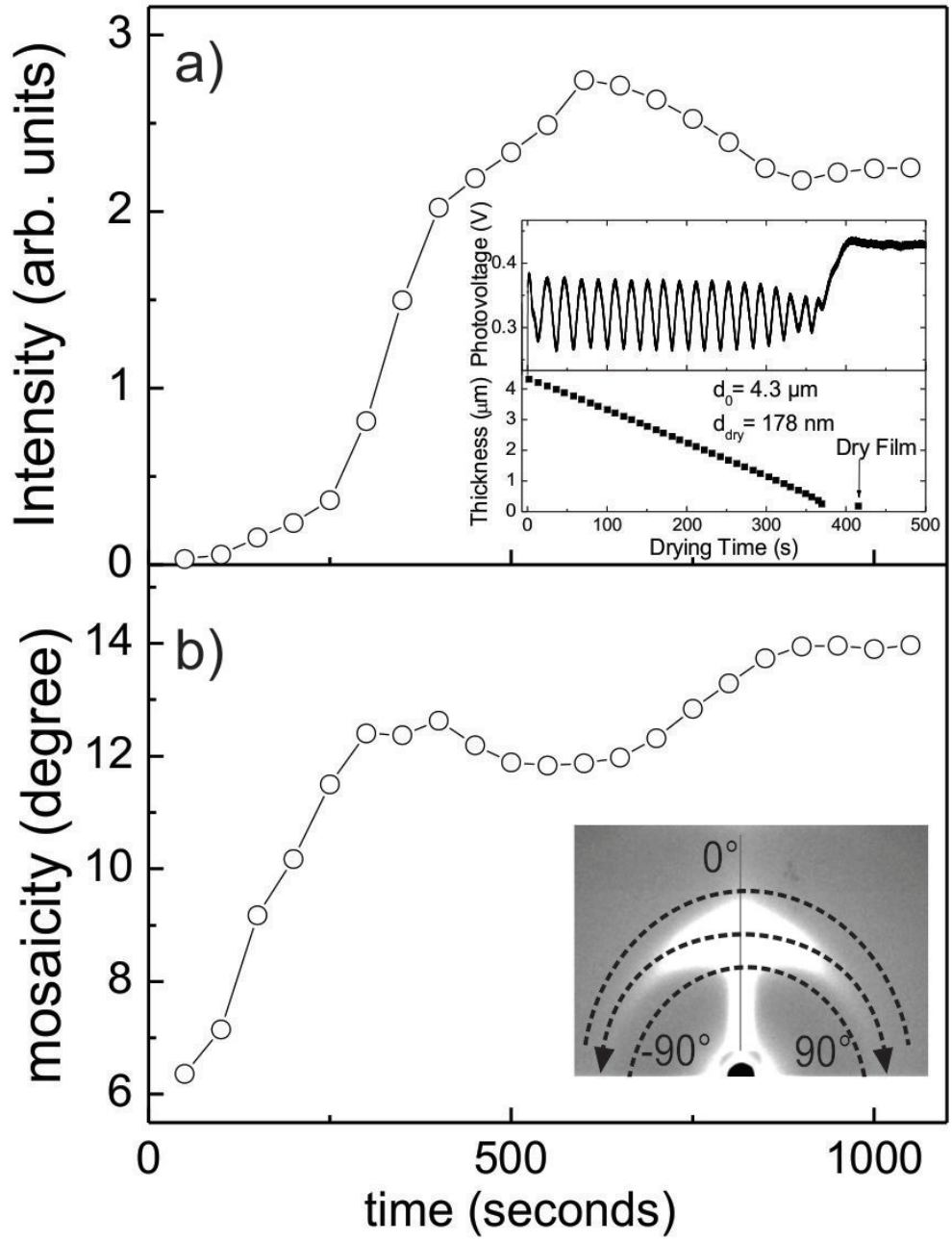

Figure 6.9: Evolution during solvent drying of (a) total integrated intensity (b) mosaicity of P3HT (100) Bragg peak. Inset in (a) shows the photovoltage of the reflected laser light (top) and blend film thickness (bottom) calculated from laser interferometery. Inset in (b) shows the azimuthal integration of the P3HT (100) Bragg peak to calculate its total integrated intensity (a) and mosaicity (b).

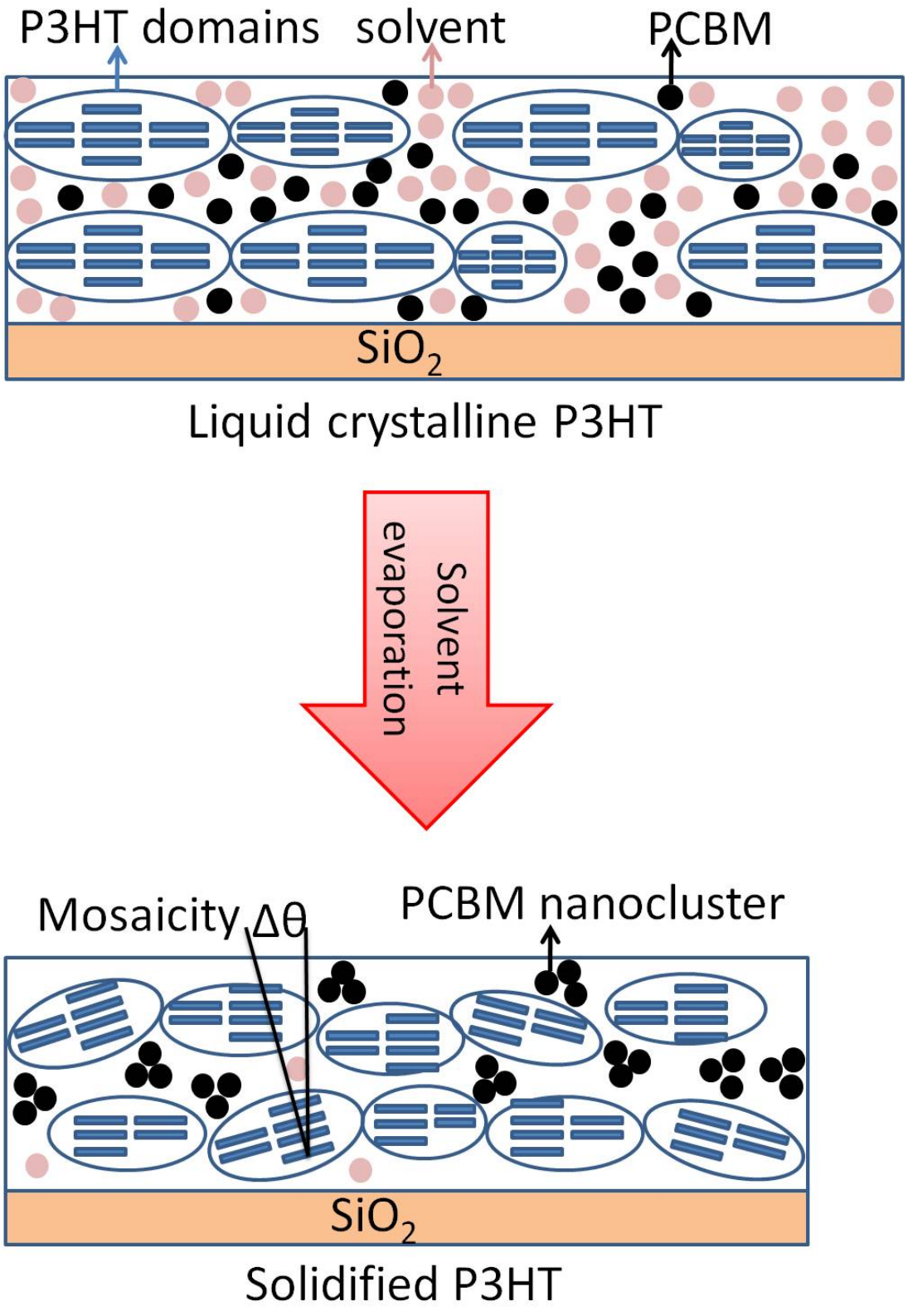

Figure 6.10: Schematic representation of the transition of P3HT from liquid crystalline phase when P3HT: PCBM blend is wet (excess solvent DCB) to solidified phase when the blend is dry (DCB evaporated) accompanied by the aggregation of PCBM molecules.

CHAPTER 7

Effect of drying temperature on P3HT: PCBM blend structure evolution

7.1 Introduction

In this chapter, the effect of drying temperature on the structural evolution of P3HT: PCBM blend processed by doctor–blading has been studied in–situ using real–time GIXD. In–situ x–ray measurements allow real–time observation of the emergence and evolution of the blend microstructure during solvent evaporation at different drying temperatures, providing fundamental understanding of the polymer/fullerene microstructure evolution during solvent evaporation. The characterization of the dried P3HT: PCBM blend films has been complemented with ex–situ GIXD, optical absorption data and atomic force microscopy. This chapter demonstrates that lowering the processing temperature during coating and drying offers a simple route to achieve a more optimized blend nanomorphology.

7.2 Experimental Details

For the in–situ study of the structural evolution during drying, the P3HT: PCBM solution in DCB was doctor–bladed with the set–up described in chapter 5 on PEDOT:PSS/ Glass substrates at drying temperatures of 10°C, 25°C, 40°C and 80°C. Using the set–up, immediately after coating, real-time x–ray scattering data was collected with a two dimensional MAR–CCD area detector for 3 seconds in intervals of 50 seconds as the solvent DCB evaporated in a temperature controlled environment. The optical interfer-

ometer allowed simultaneous measurement of the solvent–blend film thickness during solvent evaporation. The real–time GIXD study was done at beamline ID–10B in ESRF with energy 12.3 keV. Ex-situ x–ray reflectivity and GIXD measurements were done in ANKA using a point detector with energy 8 keV.

7.3 Structural Evolution of P3HT: PCBM blend during drying

Two dimensional x–ray diffraction patterns from the MAR–CCD area detector of the dried P3HT: PCBM blends after solvent evaporation at substrate temperatures of 10°C, 25°C, 40°C and 80°C are shown in Figure 7.1 a–d. The vertical and horizontal axis correspond to the components of the momentum transfer perpendicular (q_z) and parallel to the sample (q_{xy}) respectively, and also denoted out–of–plane and in–plane directions. The diffraction ring which is marked in Figure 7.1 c corresponds to randomly oriented PCBM aggregates. At all drying temperatures, the (h00) Bragg diffraction peaks arose along the out–of–plane direction reflecting the layered structure of P3HT in an edge–on configuration.

7.3.1 Evolution of Bragg peaks during drying

The "wing" like shape of the P3HT (100) Bragg peak (Figure 7.1 a–d) decreases with increasing temperature indicating a narrower distribution of crystallite orientations (mosaicity) or, in other words, a larger fraction of P3HT crystallites develop with edge–on orientation. Additionally the higher order Bragg peaks are more pronounced at higher drying temperatures, suggesting that P3HT ordering in (h00) direction increases with higher drying temperatures. The structural evolution as solvent evaporates is further analyzed in the Figures 7.1 e–f. An estimate of P3HT "degree of crystallinity" from the (100) reflection has to include the azimuthal distribution of intensity to take into account all the crystallites oriented in different directions. Therefore the x–ray scattered intensity was integrated over 180° between two concentric circles containing the P3HT (100) Bragg peak (as shown in the inset of 7.1 e) and plotted as a function of the drying time (Figure 7.1 e). This is referred to here as "(100) crystallinity" to emphasize that it gives information about the "degree of crystallinity" of the ordered layered structure of P3HT in the out–of–plane direction along q_z regardless of the quality of the P3HT π–π packing within the layers along the substrate in q_{xy}. The observed increase of P3HT (100) intensity as solvent evaporates reflects the crystallization of P3HT in the blend. At lower drying temperatures, slower kinetics of crystallization occurs due to slower evaporation of the solvent. The time evolution of the integrated intensity of the

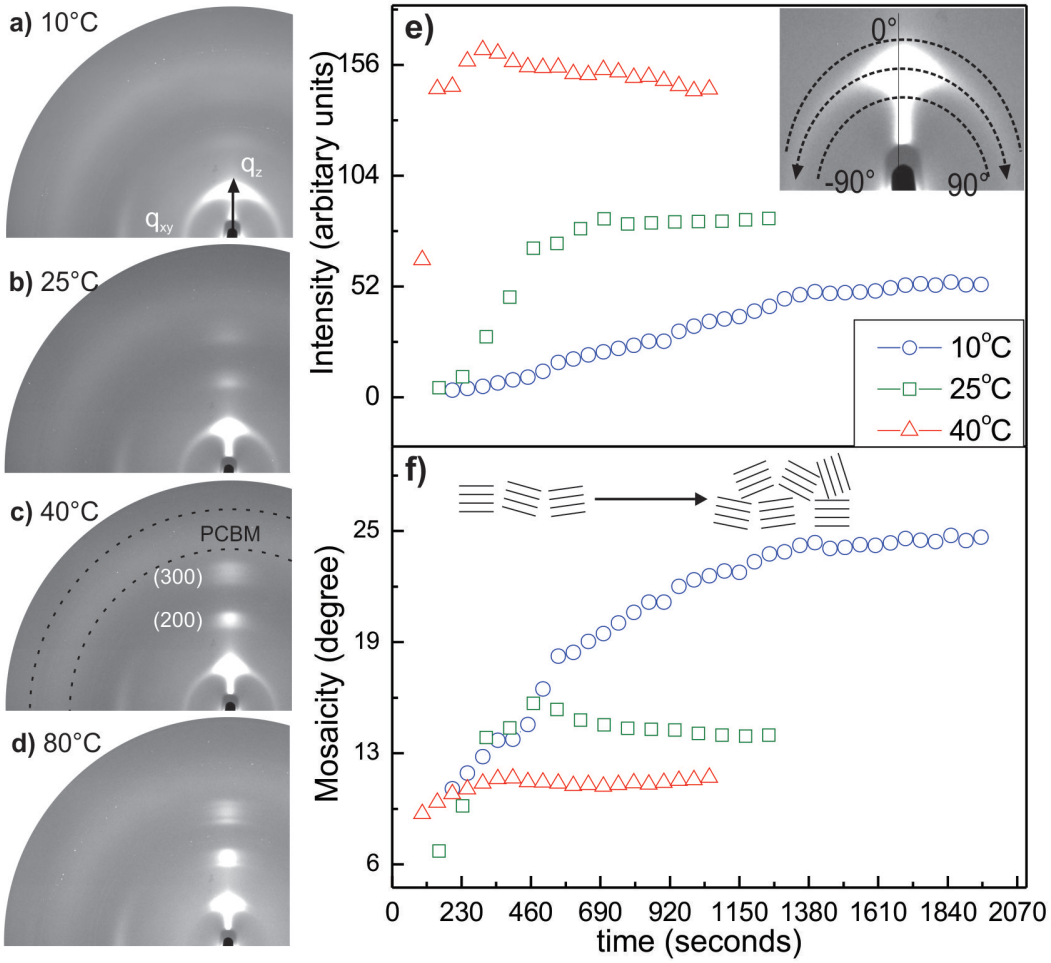

Figure 7.1: Two dimensional MAR–CCD area detector frames of dried P3HT: PCBM blend films taken at substrate temperatures of (a) 10° (b) 25° (c) 40° and (d) 80° on PEDOT:PSS/Glass substrates. Evolution of (e) total integrated intensity of P3HT (100) Bragg peak (f) mosaicity of the same with drying at substrate temperatures of 10°C (blue circles), 25°C (green squares) and 40°C (red triangles). Inset in (a) shows the azimuthal integration of the P3HT (100) Bragg peak to calculate its total integrated intensity and mosaicity.

P3HT (100) Bragg peak signifying P3HT crystallization confirms that drying at higher temperature speeds the kinetics considerably due to faster solvent evaporation (Figure 7.1 e). It has been reported that slower formation of spin–coated films promotes better P3HT ordering [74, 75, 77]. In this case a lower rate of evaporation is accompanied by reduced molecular kinetics due to decrease in thermal energy. The comparison of the intensity of the P3HT (100) Bragg peak measured in Bragg condition with a two dimensional area detector suggests a trend of decreasing total intensity for lower–temperature dried films. The final thicknesses of the blend films were 68 nm, 95 nm, 119 nm and 191 nm for drying temperatures of 80°C, 40°C, 25°C and 10°C respectively. The thickness of the blend film decreases with increasing drying temperature because of temperature dependence of viscosity. In the blend, the solid fraction was constant which led to decreasing viscosity with decreasing wet film thickness. Nevertheless Figure 7.1 e reveals worse (100) crystallinity for the films dried at higher temperature. A rough estimation of P3HT (100) crystallinity gives a value about three times higher when the film is dried at 80°C than at 10°C. The measured intensity is under–estimated for the films with larger amount of edge–on orientation on the surface i.e. for the films grown at 80°C since the exact Bragg condition is not met in this geometry [120, 121].

7.3.2 Evolution of Mosaicity during drying

Another important result is the time evolution of mosaicity, namely the angular distribution of orientations of P3HT crystallites with respect to the substrate surface as shown in Figure 7.1 f. The P3HT (100) Bragg peak intensity was radially integrated over 180° in a rim containing the entire Bragg peak to give an angular plot of the P3HT (100) intensity and fitted to a Lorentzian whose full width at half maximum gives a measure of the mosaicity as shown in the inset of the Figure 7.1 e. The evolution of the mosaicity with drying time at drying temperature of 15°C is shown in Figure 7.2 a and at drying temperature of 80°C is shown in Figure 7.2 b. It is observed that in the early stages of drying, the P3HT microcrystalline grains exhibit a similar orientation distribution of mosaicity of 7°–10° at all substrate temperatures, which is attributed to a confinement effect of the substrate interface. As solvent evaporates, there is a larger fraction of misaligned crystallites, which is significantly larger for lower temperature drying and results in the highest mosaicity of 25° for the dried film at 10°. The larger mosaic spread of P3HT crystallites for the films dried at lower temperature can be related to the slower kinetics of film formation. The true values of mosaicity are obtained in Bragg condition as shown in Table 7.1. In grazing incidence geometry, the measured values of mosaicity are underestimated. Measurements at Bragg condition with a two dimensional detector also confirm that there is a strong trend for P3HT: PCBM blend

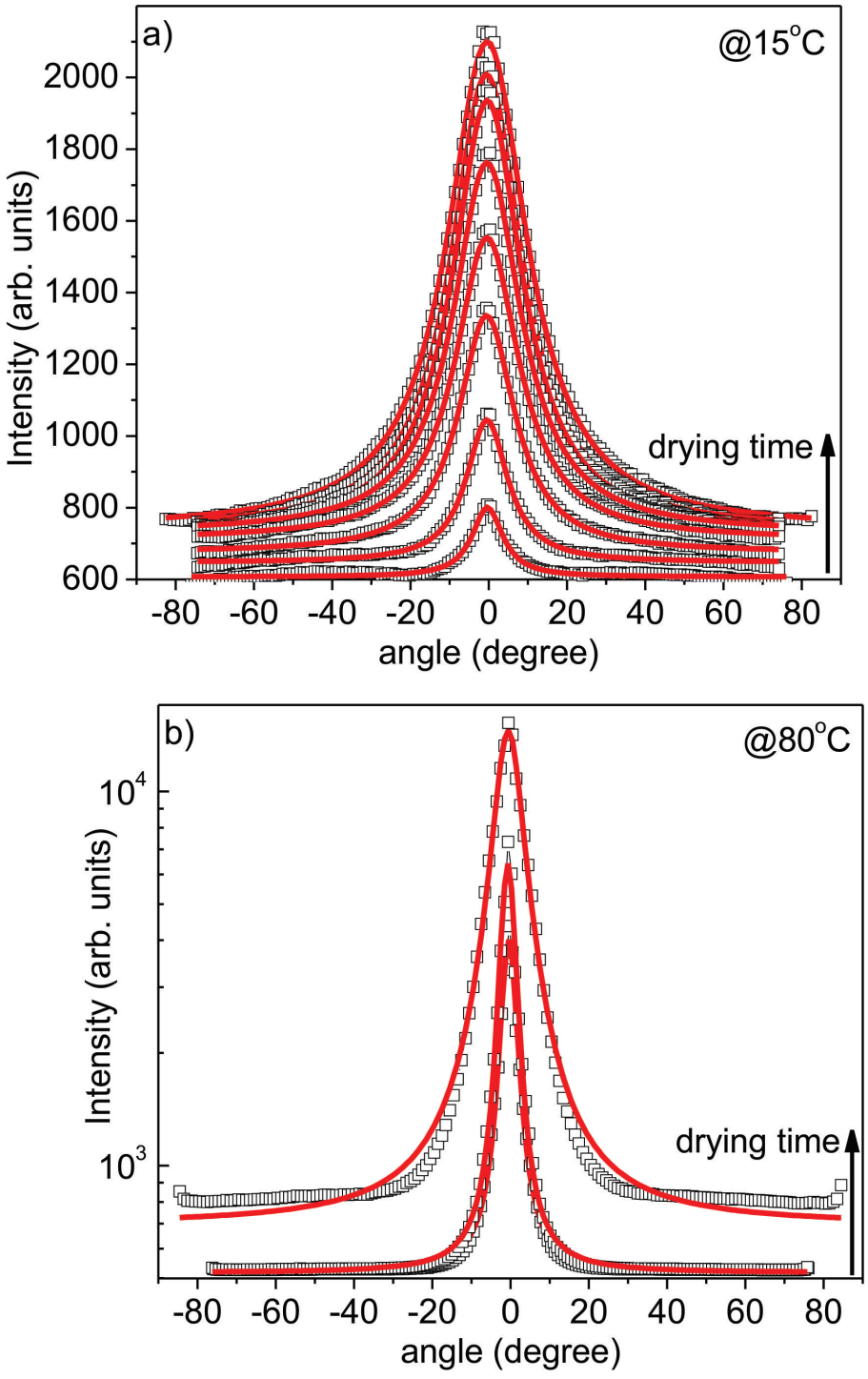

Figure 7.2: Angular pole plots showing the evolution of mosaicity of P3HT (100) Bragg peak with drying time at drying temperatures of (a) 15°C (b) 80°C. Mosaicity was calculated as shown in the inset of 7.1

Table 7.1: Comparison of mosaicity values in grazing incidence and Bragg geometry

Temperature (°C)	Bragg (°)	GIXD (°)
15	33.1	26.2
25	24.3	19.6
40	14.5	11.2
80	18.9	10.8

Table 7.2: Structural parameters for P3HT obtained from the GIXD and specular reflectivity data for films dried at different temperatures: Mosaicity, spacings (d) associated to the (100) and (020) Bragg reflections of P3HT, mean coherence length along those crystallographic directions (L) and ratio of integrated intensity of (020) to PCBM in–plane peaks ($I_{(020)/PCBM)}$).

Temperature (°C)	Mosaicity (°)	d_{100} (Å)	d_{020} (Å)	L_{100} (Å)	L_{020} (Å)	$I_{(020)/PCBM}$ (Å)
15	26.15	16.15	3.84	194	118	0.658
25	19.56	16.46	3.82	200	76	0.175
40	11.17	16.58	3.82	306	93	0.149
80	10.77	16.87	3.82	308	77	0.093

to have larger mosaicity at lower drying temperatures (Figure 7.1).

Further quantitative structural information of P3HT and PCBM ordering perpendicular and parallel to the substrate surface has been obtained ex–situ with a point–detector in specular reflection and grazing incidence geometries. In these two geometries the x–ray scattered intensity is exactly probed along q_z and q_{xy}, respectively. An accurate quantification of the associated spacing and coherence length of the P3HT layered structure along out–of–plane direction and of P3HT π–π interchain stacking along in–plane direction can be performed. The measurements were conducted on PEDOT:PSS/ ITO/ Glass substrates for future comparison with solar cells devices. The P3HT: PCBM blends coated on the said substrates were dried at 15°C, 25°C, 40°C and 80°C drying temperatures. The out–of–plane and in–plane x–ray data are shown in Figure 7.3 a and Figure 7.3 b. The specular x–ray data reveals a shift of the Bragg peak position towards lower q_z and an increase of intensity for higher temperature drying of the films. The observed shift is due to a larger average interlayer spacing (d_{100}) for higher drying temperature (Table 7.2). The observed higher intensity for P3HT: PCBM blends dried at higher drying temperatures is due to both, a stronger preferential orientation of P3HT in edge–on configuration, resulting in lower mosaicity and an overall higher degree of P3HT (100) crystallinity (Figure 7.1 e and f). The mean coherence length (L_{100}) deduced

from the full width half maximum of the P3HT (100) peak, is a rough approximation of the mean size of P3HT crystallites along q_z in the out–of–plane direction. L_{100} increases with drying temperature from 194 Å at 15°C to 308 Å at 80°C. The structural characteristics derived from the analysis of the P3HT (100) crystallinity are that higher temperature drying results in

1. A higher fraction of P3HT crystallites being stacked regularly in layers.

2. Better alignment of P3HT in the edge–on orientation.

3. Larger mean coherence length of P3HT crystallites along the layered stack i.e. along the [100] direction.

These results suggest that higher drying temperature enables better P3HT ordering due to the effect of increased thermal molecular mobility.

However good P3HT ordering impedes nanophase mixing of P3HT and PCBM which is mandatory for good solar cell performance as discussed in chapter 2. The investigation of the in–plane structure and optical absorption properties as discussed below corroborates this finding.

Precise structural information of the in–plane ordering is achieved with GIXD. In the in–plane GIXD data (Figure 7.3 b), the middle broad peak is due to PCBM and the last sharp peak on the right corresponds to the P3HT (020) which is associated with the π–π interchain stacking within the P3HT layers. The spacing of 4.5 Å associated to the PCBM diffraction peak was the same at all drying temperatures. The observation of the P3HT (020) in–plane peak indicates that the π–π assembly of P3HT chains develops at all drying temperatures with a spacing (d_{020}) of 3.8 Å, in agreement with previous studies [122–124]. However, the crystallinity of the π–π stacking increases significantly at lower drying temperature as revealed by the larger intensity of the P3HT (020) peak. In Table 7.2, the integrated intensity is given relative to the PCBM peak giving clear evidence of this trend. Additionally the coherence length of the π–π stacking within the P3HT layers (L_{020}) estimated from the width of the P3HT (020) peak is the largest for the sample dried at the lowest temperature; 118 Å at drying temperature of 15°C compared to 76 Å, 93 Å, 77 Å for the temperatures of 25°C, 40°C and 80°C, respectively (Table 7.2). These results suggest that films dried at lower temperature have better P3HT interchain π–π ordering.

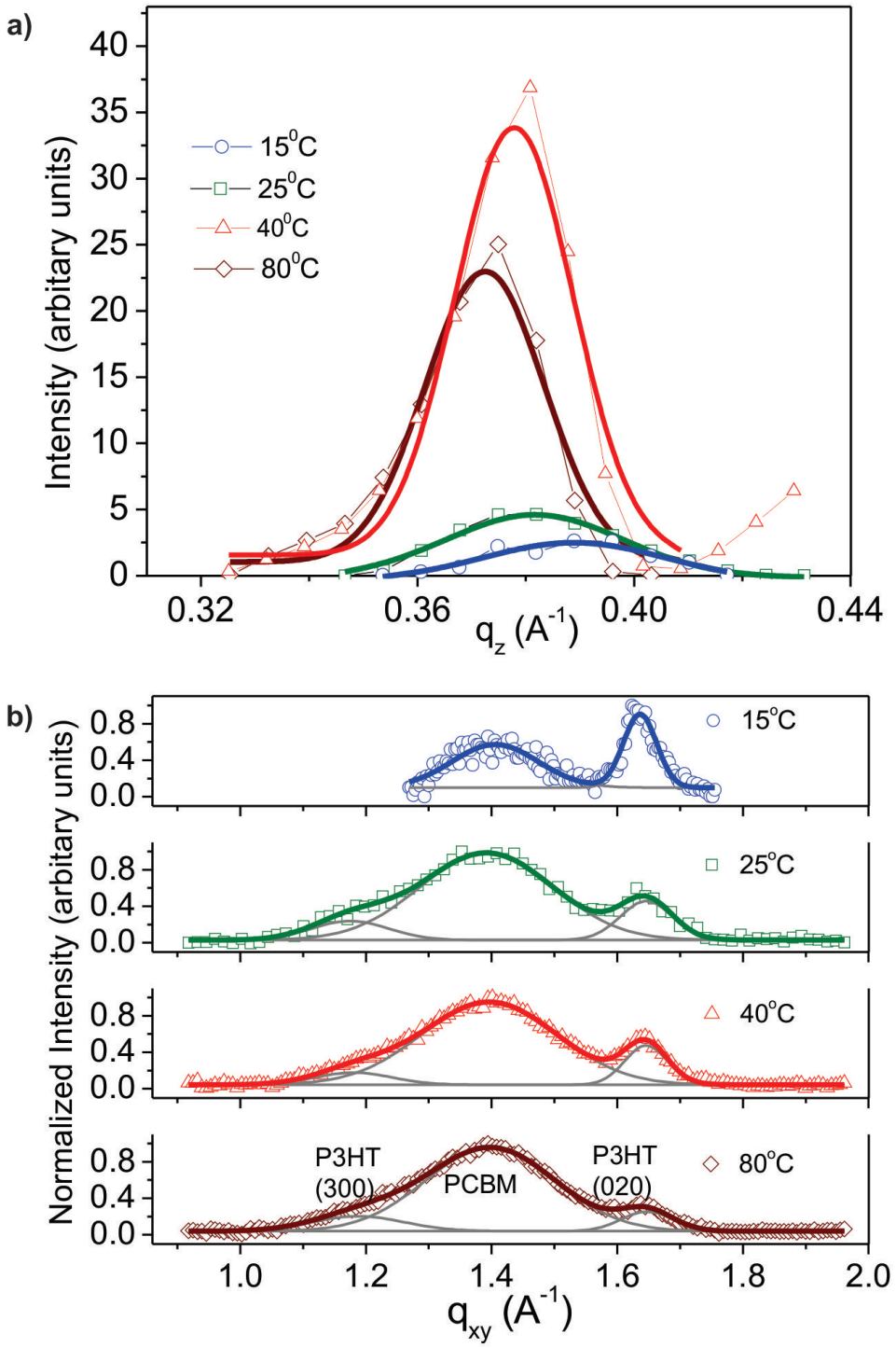

Figure 7.3: (a) X–ray reflectivity (b) GIXD data of P3HT: PCBM blends dried at substrate temperatures of (a) 15°C (blue) (b) 25°C (green), (c) 40°C (red) and (d) 80°C (maroon). The symbols are the data points and the solid lines are the Gaussian fits.

7.4 Optical Absorption and AFM data for P3HT: PCBM blend at different drying temperatures

Further insight into the crystalline organization of P3HT is obtained from the optical absorption spectra measured on the same films investigated by x–ray diffraction using a point detector (Figure 7.4 a). The absorption spectra for the different dried films (Figure 7.4 a) reveal a continuous red–shift of the P3HT absorption peak maximum around 500 nm and the appearance of vibronic sidebands with decreasing drying temperature. The red–shift of the solid–state absorption band in the dried blend films have been explained by an increase of the effective conjugation length due to a more planar and homogeneous conformation of the polymer backbone resulting from fewer twist or longer rotational defects. The vibronic sidebands related to the π–π P3HT interchain stacking are a direct consequence of good interchain interaction [65, 125, 126]. Hence the well structured solid state absorption achieved at 15°C, may be associated with a good P3HT interchain π–π packing. The in–plane data corroborates that delocalization of charge carriers and polaron excitations over neighboring chains takes place contributing to a more efficient solar cell performance [65, 125, 127]. This combined study reveals that although P3HT exhibits a significantly poorer "(100) crystallinity" for blend films dried at lower temperature, it develops better order along the P3HT π–π interchain stacking direction. Further structural effects resulting from lowering the drying temperature that P3HT has smaller interlayer spacing resulting in increased density in the out–of–plane direction in q_z and increase in the orientational distribution of P3HT crystallites resulting in increased mosaicity. Photoactive bulk heterojunction films processed by solvent annealing [75, 77], with octanedithiol [10] or by thermal annealing leading to better performing solar cells exhibit well structured solid–state absorption with red–shifted maximum and pronounced side shoulders: a shorter P3HT (100) interlayer spacing for solvent annealed or octanedithiol processed films and a longer P3HT (100) interlayer spacing is observed for thermally annealed films. The larger mosaicity of P3HT crystallites is expected to provide enhanced charge carrier transport perpendicular to the substrate in q_z, as required by bulk heterojunction solar cells [58]. This is in contrast to films with the π–π stacking direction predominantly parallel to the surface in edge–on configuration.

In addition, reduced molecular kinetics at low drying temperature restricts the phase separation of P3HT and PCBM, required for finer mixed nanomorphology of P3HT and PCBM in the bulk heterojunction. The following comparative AFM study supports this hypothesis. The film topography for blends dried at 15°C and at 40°C is depicted on the left of Figures 7.4 b and c, respectively. Subsequently, PCBM was removed by washing

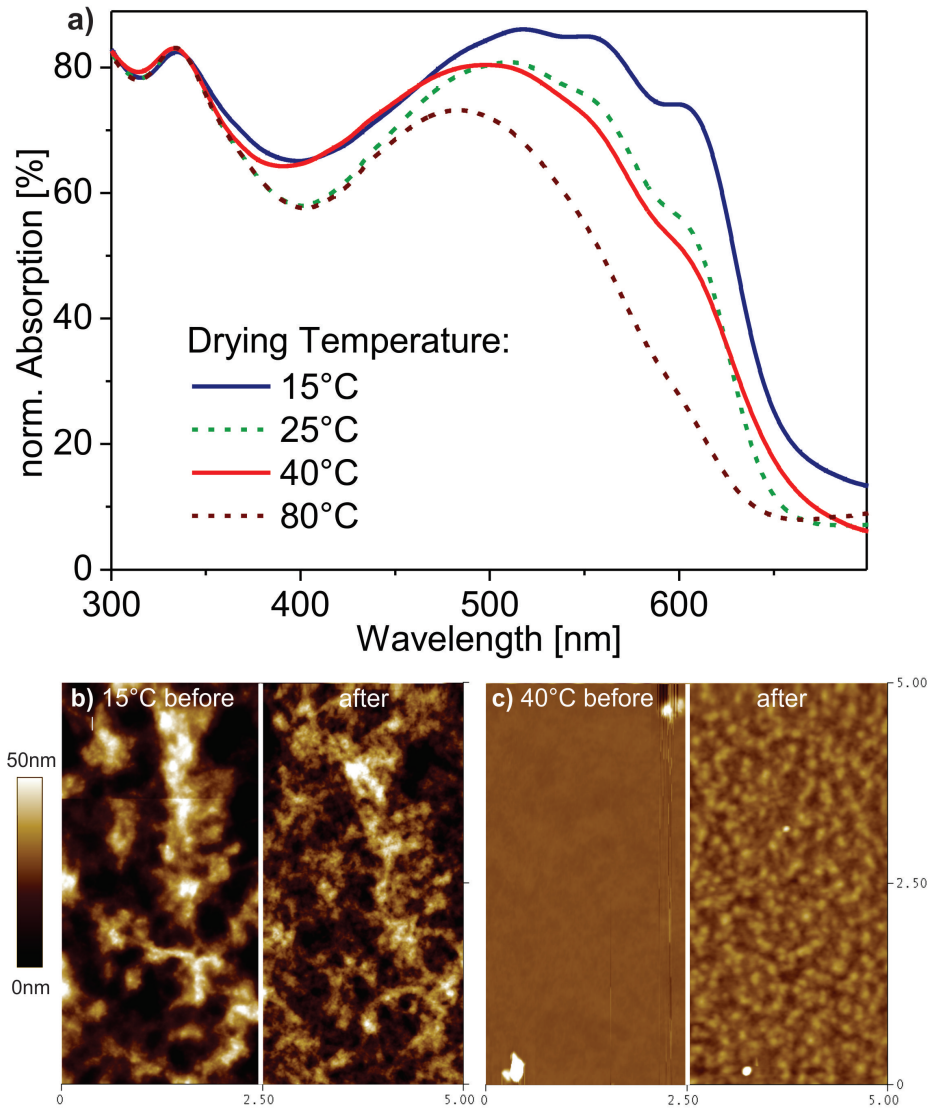

Figure 7.4: (a) Absorption spectra of doctor-bladed P3HT: PCBM films coated and dried from DCB solution at different temperatures (15°C–80°C) normalized to the isotropic PCBM peak at 330 nm. Atomic force microscope topography images of P3HT: PCBM films doctor bladed at b) 15°C and c) 40°C (represented with the same topographical scale). In each case, the left image shows the untreated blend film and the right image shows the film topography after washing of PCBM with octanethiol. (Data was collected at the Karlsruhe Institute of Technology.)

the film with octanethiol and then the films were imaged again by AFM (on the right of Figures 7.4 c and d) to reveal the places of PCBM domains. Although the topography of the blend dried at 15°C appears rougher and with larger lateral features in comparison to the smooth surface formed at 40°C drying, the porous structure remaining upon removal of PCBM domains is evidently larger for the 40°C process conditions, confirming the trend of increased phase segregation at higher drying temperatures. This is in agreement with results recently reported for low temperature and room temperature spin–coated solar cells [75].

7.5 Conclusions

In summary, the x–ray in–situ study reported in this chapter gives insight into the effect of the drying temperature on the structural evolution of doctor–bladed P3HT: PCBM blends in the transition from wet solvent–blend film to solid blend film. It has been shown that drying the photoactive P3HT: PCBM blend at lower temperature of 10°C leads to good π–π P3HT assembly and broader orientational distribution of P3HT in comparison to drying at 25°C, 40°C and 80°C. Slow crystallization kinetics and restricted phase separation of P3HT and PCBM due to lower molecular mobility enable better nanomorphology with finer interpenetrated network in the P3HT: PCBM bulk heterojunction. On the basis of the results presented in this chapter, it can be proposed that lowering the substrate temperature during coating the photoactive P3HT: PCBM blend film and its subsequent drying is a simple route for optimization of device efficiency in doctor–bladed solar cells.

CHAPTER 8

Effect of P3HT: PCBM composition ratio on blend structure

8.1 Introduction

In this chapter, the effect of composition of P3HT: PCBM blend on its microstructure evolution has been studied in–situ with GIXD. The difference in structural evolution, especially of the π–π interchain stacking within P3HT, of P3HT: PCBM blends with ratios 1 : 0.5, 1 : 0.8 and 1 : 2 has been investigated here. In this chapter, it has been demonstrated that large excess of PCBM over the eutectic composition impedes the π–π packing of P3HT chains and leads to the observation of a new diffraction feature with an associated spacing of 12.6 Å, which might originate either from a disordered phase of PCBM or from the formation of a mixed P3HT–PCBM phase by charge transfer interaction. It is known that for a given combination of donor and acceptor materials, the performance of the solar cell depends critically on the nanoscale details of the blend such as the molecular packing, spatial distribution and size of the phase–separated domains that develop dynamically during its solidification, which is strongly determined by the composition ratio of the blend and material properties such as the mutual miscibility, solubility and surface energies [80, 128]. A major obstacle to enhanced performance is the optimization of the ratio of components and processing protocols in order to achieve a blend microstructure that simultaneously ensures efficient exciton generation, exciton dissociation, and charge transport to electrodes. Previous works have reported that the optimum P3HT: PCBM ratio for best device performance is about 1 : 0.8 [80]. A recent study on the phase behavior proposes that the optimum ratio is at a composition that is slighly hypoeutectic, as it is probably linked to the formation of a nanomorphology that favors a balanced hole and electron transport [129]. The results discussed in this chapter are important because they provide a microscopic un-

derstanding of the nanoscale phase segregation in polymer/fullerene bulk heterojunctions with different blend ratios, necessary for improving photovoltaic performance in an industrially relevant process of production.

8.2 Experimental details

To study the in–situ structural evolution of the P3HT: PCBM blends of ratios 1 : 0.5, 1 : 0.8 and 1 : 2 instantly after film coating, the temperature controlled drying channel with the integrated knife coater as described in chapter 5 was used. The in–situ scattering study was carried out with x–rays of wavelength $\lambda = 0.934\,\text{Å}$ at the ID–10B beamline in ESRF. Immediately after coating each P3HT: PCBM blend having a different composition, GIXD data was taken by the two dimensional MAR–CCD area detector for 3 seconds in intervals of 50 seconds as the blend film dried at a controlled temperature of 25°C. The in–plane structure of P3HT and PCBM in dried blend films with ratios 1 : 0.5, 1 : 2, with only P3HT and only PCBM on industrially relevant PEDOT:PSS/ITO/Glass substrates was studied in the MPI–MF beamline at ANKA with energy 8 keV.

8.3 Structural evolution of P3HT: PCBM blend of different compositions during drying

The initial thicknesses of the wet coated films of P3HT: PCBM blends with ratios 1 : 0.5, 1 : 0.8 and 1 : 2 respectively were 3855 nm, 2728 nm and 2189 nm and the thicknesses of the final dried films for these blend ratios respectively were 134 nm, 200 nm and 69 nm. Differences in the thicknesses of the coated blend–solution were responsible for variations in the speed of drying and the final thicknesses attained. Two dimensional x–ray scattering frames taken from the MAR–CCD detector illustrating different stages of drying of the blends are shown in Figure 8.1 for the P3HT: PCBM blend–ratios 1 : 0.5, 1 : 0.8 and 1 : 2. The structural features corresponding to the x–ray scattering from DCB, P3HT and PCBM appear for the three blend ratios during solvent evaporation. In the initial stages of drying for all the three blend ratios (1 a, 2 a and 3 a in Figure 8.1), two broad diffraction rings were visible associated to spacings of 3.8 Å and 5.6 Å that correspond to x–ray scattered from solvent DCB. These diffraction rings gradually disappeared completely in the course of solvent evaporation. The first sign of P3HT ordering can be seen in frames 1 b, 2 b and 3 b of Figure 8.1 when the first order pseudo–Bragg peak appears along the out–of–plane q_z direction. The second and third order Bragg peaks can be observed in the frames 1 c, 2 c and 3 c of Figure 8.1. The average

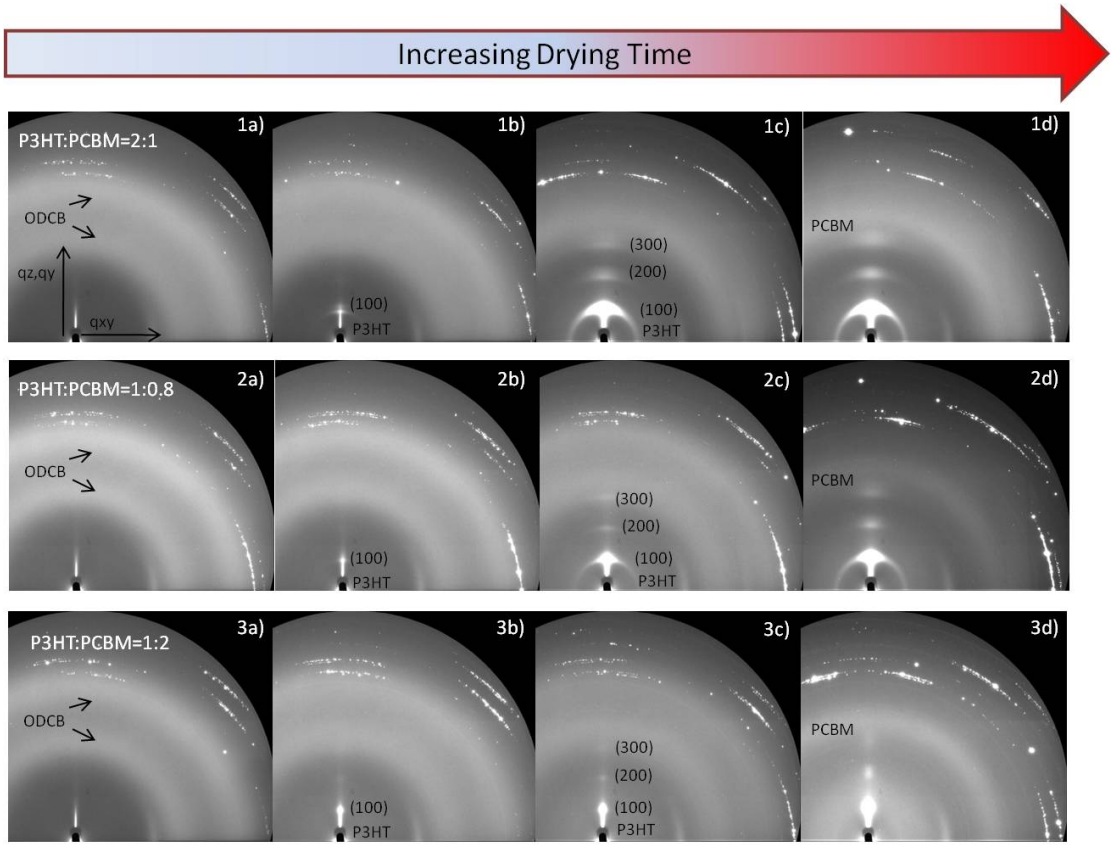

Figure 8.1: Two dimensional MAR-CCD area detector images showing drying of P3HT: PCBM blends of ratio [1a) to 1d)] 1:0.5, [2a) to 2d)] 1:0.8 and [3a) to 3d)] 1:2 doctor–bladed on PEDOT:PSS/Glass substrates (a) right after coating the blend on the substrate (b) appearance of the first order Bragg peak (c) appearance of higher order Bragg peaks (d) when the blend film has dried.

spacing of 16.3 Å associated with (h00) Bragg peaks for all the three blend ratios arises from the edge–on, layered stacking of P3HT backbones separated by their hexyl side chains (a–axis perpendicular to the substrate) [40, 42, 49, 130]. Towards the end of film drying, a broad diffraction ring associated with PCBM aggregates is seen to be randomly oriented in the blend (1 d, 2 d and 3 d in Figure 8.1) with an associated spacing of 4.1 Å.

8.3.1 Evolution of Bragg peaks during drying

During the course of solvent evaporation, major differences are observed in the shape and evolution of the P3HT Bragg peaks. The investigated blend ratios 1 : 0.5, 1 : 08 and 1 : 2 show the organization of P3HT in a layered structure responsible for the observation of (h00) Bragg peaks in the out–of–plane direction. The arcing of the P3HT

(h00) Bragg peaks observed were due to an azimuthal distribution of the intensity of the P3HT (h00) Bragg peaks in the P3HT: PCBM blends with ratios 1 : 2 and 1 : 0.8. This arcing indicates that a relatively large distribution of P3HT crystallite are misaligned with respect to the substrate surface i.e. P3HT crystallites have their a–axis tilted away from the direction perpendicular to the surface. In contrast, the spot–like shape of the P3HT (h00) Bragg peaks in the P3HT: PCBM blend with ratio 1 : 2 indicates a stronger ordering of the P3HT a–axis along the surface normal. In Figure 8.2, the time evolution of the integrated intensity (Figure 8.2 a) and the angular distribution of the P3HT crystalline domains, namely mosaicity (Figure 8.2 b) of the P3HT (100) Bragg peak has been plotted. The intensity, which provides an estimate of the crystallization of P3HT in a layered structure, was calculated by integrating over 180° the area between two concentric circles containing the P3HT (100) Bragg peak as shown in the inset of the Figure 8.2 a. The intensity shown in the Figure 8.2 a has been normalized to the maximum value for each blend ratio.

8.3.2 Different stages of drying in different blend compositions

The real–time study reveals a remarkable effect of PCBM on the development and evolution of ordering of P3HT during film drying. The plots in Figure 8.2 a shows two stages —

1. The first 500 seconds of drying, when the blend film is wet. During this stage, a monotonous decrease of the thickness of the wet blend–solution film as measured by optical interferometry takes place accompanied with the crystallization of P3HT measured with GIXD. At the end of this stage, P3HT has fully crystallized. The angular spread of the P3HT (100) intensity was fitted to a Lorentzian curve whose full width at half maximum gives a measure of the orientational distribution of crystallites known as the mosaicity (Figure 8.2 b). The mosaicity measured in the early stages of drying revealed a relatively narrow orientation distribution for all the different compositions of P3HT: PCBM blends, albeit with a slightly larger value of mosaicity for increasing concentration of P3HT. The increase of PCBM content in P3HT: PCBM blend film led to a smaller angular distribution of P3HT crystallites with higher edge–on configuration. The highest PCBM concentration studied in this chapter is in the P3HT: PCBM blend with ratio 1 : 2 in which the initially nucleated P3HT crystallites has lower mosaicity of about 6 Å and it remains constant during further P3HT crystallization accompanying drying of the blend. Larger fraction of edge–on P3HT crystallites is expected to be a hindrance for charge carrier transport perpendicular to the

substrate, as is required for bulk heterojunction solar cells. This is because the interchain π–π stacking direction of P3HT is predominantly parallel to the surface.

2. After 500 seconds of drying, when the solvent has completely evaporated from the blend film and the blend film is dry. The evolution of mosaicity with drying time was remarkably different for the P3HT: PCBM blends with ratios 1 : 0.5 and 1 : 0.8, i.e. with larger fraction of P3HT in the blend. For these two compositions, the mosaicity increased during the evaporation of the solvent to a maximum of 15.5° for the P3HT: PCBM blend with ratio 1 : 0.8 and to 21° for the blend with ratio 1 : 0.5 when these blend films dried at about 500 seconds. After about 500 seconds, the blend film with ratio 1 : 0.5 undergoes a gradual decrease of mosaicity accompanied with increase of crystallization. This can be attributed to slow reorganization of the P3HT crystallites during the slow removal of the remaining solvent molecules and the interaction of the remaining solvent in the drying channel, similar to solvent annealing effect [131] discussed in the chapter 2. In the case of the blend ratio 1 : 2, the mosaicity remained constant at about 6° during the whole drying process.

Despite the good P3HT out–of–plane ordering along q_z, increase in PCBM content in the P3HT: PCBM blend with ratio 1 : 2 hinders the organization of the interchain π–π stacking of P3HT along the substrate in the q_{xy} direction. This is in correlation with the disappearance of the two long–wavelength vibronic features in the optical absorption spectra previously reported. Since P3HT π–π packing is responsible for delocalization of charge carriers and polaron excitations over neighboring chains, contributing to more efficient solar cell performance, the lack of π–π P3HT interchain packing is identified as the factor responsible for the degraded power conversion efficiency for 1 : 2 blends [75, 132, 133].

8.3.3 Evolution of the P3HT interchain π–π packing

The in–plane P3HT (020) Bragg peak, barely visible to the eye in the MAR–CCD area detector images, appear at the end of drying. When profile plots in frames 1 d, 2 d and 3 d of Figure 8.1 on the MAR–CCD images are taken along q_{xy} at $q_z = 0.056\,\text{Å}^{-1}$ (i.e. along the horizontal at the bottom of the x–ray diffraction images) for all the blend compositions, P3HT (020) peak of spacing 3.8 Å is obtained. This peak corresponds to the short–range ordering of π–π interchain stacking within the P3HT layers. The correlation length of this π–π interchain stacking within the P3HT layers is 54.2 Å for the P3HT: PCBM blend with ratio 1 : 0.5; it is 61.5 Å for the blend with ratio 1 : 0.8 and it is absent in the blend with ratio 1 : 2. Initially, this finding suggests that PCBM disrupts

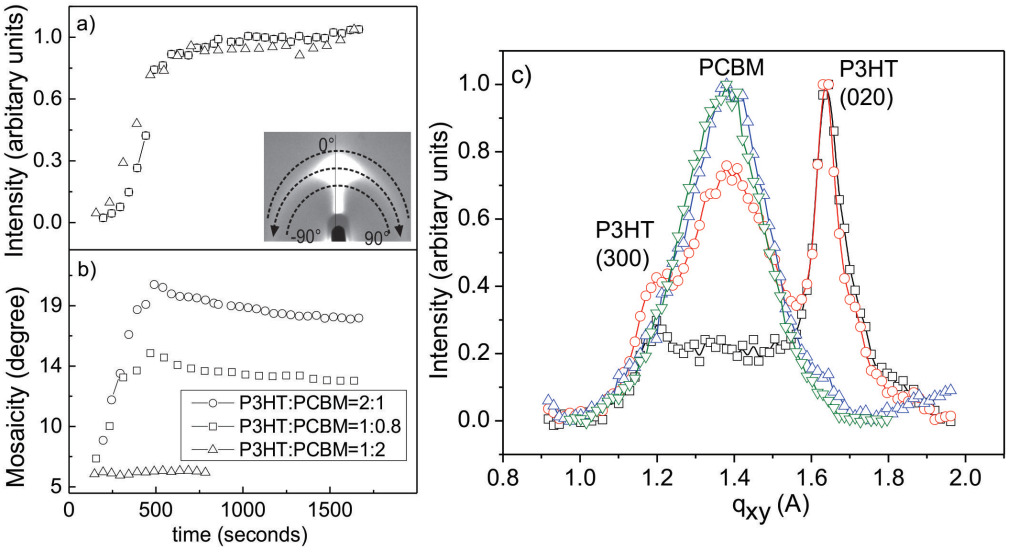

Figure 8.2: Evolution of (a) total integrated intensity (b) mosaicity of P3HT (100) Bragg peak of P3HT: PCBM blend ratios 1:0.5 (open circles), 1:0.8 (open rectangles) and 1:2 (open triangles) (c) GIXD data of films of pure P3HT (black square), P3HT: PCBM=1:0.5 (red circle), P3HT: PCBM=1:2 (blue triangle) and pure PCBM (green inverted triangle). The in–plane P3HT (020), PCBM and slightly visible P3HT (300) peaks have been labeled. The lines are a guide to the eye. The inset in (a) shows the azimuthal integration of the P3HT Bragg peak to calculate the total integrated intensity and the mosaicity.

the in–plane ordering of P3HT. The π–π stacking of P3HT backbones is important because this is one of the crystalline directions of highest charge mobility. However as the intensity of the P3HT (020) peak observed was very weak in the two dimensional x–ray diffraction images, more accurate measurements with a point detector were performed in ANKA. The in–plane scans are shown in Fig 8.2 c for pure films of P3HT and PCBM and blend films with P3HT: PCBM blend ratios of 1 : 0.5 and 1 : 2. The P3HT (020) peak for the pure P3HT film and 1 : 0.5 blend correspond to a spacing of 3.8 Å previously reported [122]. However the P3HT (020) peak is absent in the blend with the highest PCBM content, i.e. in the blend with ratio 1 : 2, once again suggesting that PCBM impedes the development of π–π interchain stacking within the P3HT crystallites. Differences are not observed in the diffraction peaks of PCBM of different blend compositions. They all show similar spacing of 4.5 Å and coherence length of about 30 Å in the pure PCBM and P3HT: PCBM blend films. The spacings and the correlation lengths of pure P3HT, pure PCBM and the blend of P3HT: PCBM have been summarized in Table 8.1.

Table 8.1: Correlation lengths for P3HT π–π stacking and PCBM for the different blend compositions

	Pure P3HT (Å)	P3HT: PCBM=1 : 0.5 (Å)	P3HT: PCBM=1 : 2 (Å)	Pure PCBM (Å)
P3HT (020)	86.9	84	absent	
PCBM		28	32.5	28.9

8.3.4 Formation of P3HT–PCBM complex

A broad diffraction ring in the P3HT: PCBM blend with ratio 1 : 2 is observed and is shown in the Figure 8.3. Figure 8.3 shows the images of the dried films of P3HT: PCBM blend with ratio 2 : 1 (Figure 8.3 a) and P3HT: PCBM blend with ratio 1 : 2 (Figure 8.3 b). A diffraction ring is seen between the first and second order Bragg peak. This ring has an associated spacing of 12.6 Å and can be attributed to a different PCBM phase as result of phase segregation and crystallization of PCBM as this blend ratio is well below the eutectic concentration [80]. The profile of this broad diffraction ring is shown in the Figure 8.3 d . It is not a priori clear whether this ring comes from x–ray scattering of P3HT or PCBM molecules. The hypothesis of it being a scattering feature related to P3HT may be discarded as the spacing observed here differs considerably from the lattice spacings observed for crystalline and disordered phases [42, 123] previously reported for P3HT. The crystalline structure of PCBM has not fully been characterized and differences in experimental reported values suggest that the choice of solvent or even crystallization conditions may affect the crystallization process of PCBM [69, 120, 121, 129, 134–138]. Since the distance between nearest neighbor PCBM molecules have been reported to be betwen 10 and 13 Å , it is physically plausible that this scattering ring provides a different structural phase of PCBM formed in the P3HT: PCBM with a large excess of PCBM. There is however a possibility of the formation of a mixed structure where the PCBM molecules are intercalated within the P3HT backbones. The formation of such a disordered mixed phase agrees with the short–correlation length observed. The plane–to–plane stacking distance of conjugated P3HT backbone is about 3.5 Å and the center–to–center distance of PCBM is reported to be about 10.5 Å . This mixed P3HT–PCBM phase can be attributed to a charge transfer interaction between the electron–rich π system of P3HT and the strong acceptor character of PCBM. The disordered mixed P3HT–PCBM phase were observed in MDMO-PPV:PCBM blends through the low intensity charge transfer absorption bands which showed a red–shift and a proportional decrease in open circuit voltage (V_{oc}) with increasing PCBM concentration. [139] Therefore the formation of mixed P3HT–PCBM phase driven by charge–charge transfer interaction is, although inconsistent with the

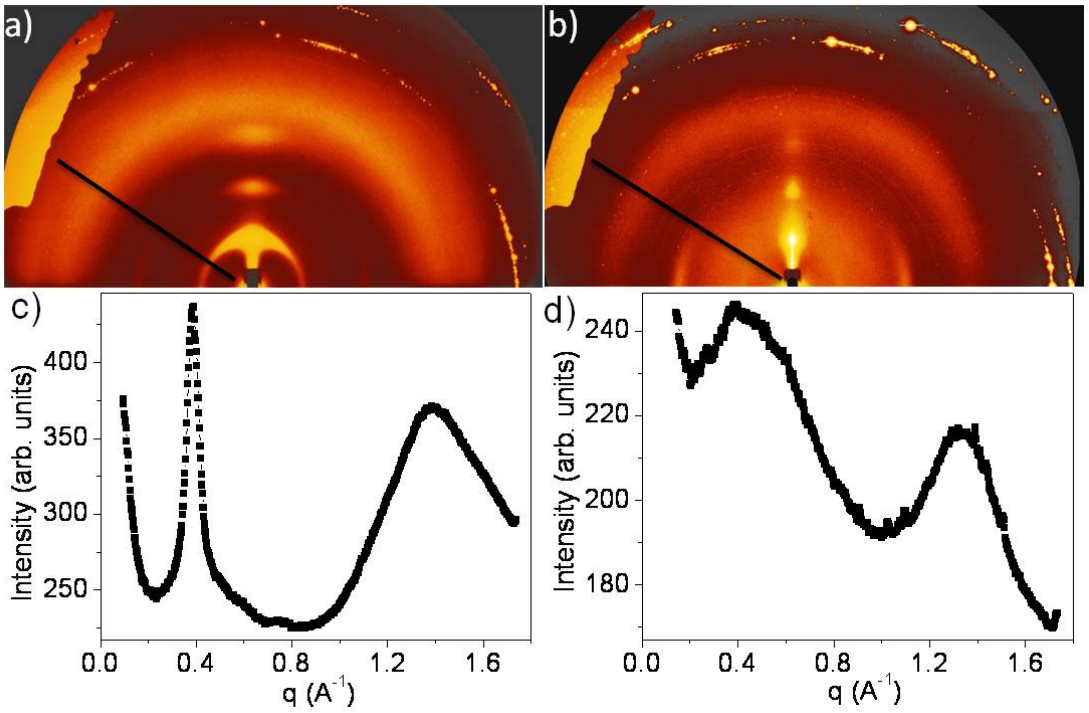

Figure 8.3: X–ray diffraction images of dried blend films with P3HT: PCBM ratios of (a) 1:0.5 (b) 1:2. Radial profiles at the same position in images (a) and (b) were taken. Black lines marked in (a) and (b) denote the position where the radial profiles shown in (c) and (d) were taken.

expected phase behavior, still physically plausible. So the new structural feature of PCBM with very short correlation length can be attributed to the phase segregation of disordered PCBM in this hypoeutectic mixture. [80] So the formation of a disordered mixed P3HT–PCBM phase with PCBM intercalated between P3HT backbones driven by charge–charge transfer interaction cannot be discarded and would be consistent with the observed disruption of P3HT π–π packing for this composition. The existence of such an intermediate charge–transfer state in a bulk heterojunction consisting of P3HT and PCBM has been experimentally shown. [140–142]. An extended investigation of charge–transfer absorption in dependence with PCBM concentration could help to elucidate this issue.

8.4 Conclusions

In this chapter, it has been demonstrated that P3HT: PCBM blends with ratios 1 : 0.5, 1 : 0.8 and 1 : 2 have differing structural evolutions during the course of solvent evaporation and different structures are formed at the end of drying. It has been shown here that with increasing PCBM content in the P3HT: PCBM blend:

1. A larger portion of edge–on P3HT crystallites develop in the blend.
2. Shorter range P3HT interchain π–π packing are completely absent in the 1 : 2 blend ratio proving that PCBM impede π–π packing of P3HT molecules.
3. Lead to the formation of a distinct diffraction feature for the highest PCBM content (1 : 2) with an associated spacing of 12.6 Å, which is attributed to the formation of disordered phase either due to PCBM with a different structure or to a mixed P3HT–PCBM structure by charge–charge transfer interaction.

Previous works have reported that the optimum P3HT: PCBM ratio for best device performance is about 1 : 0.8 as at this blend ratio simultaneous increase of short–circuit current and fill factor are drastically reduced with higher PCBM concentration. [132, 143] Optical ultra–violet–visual absorption studies showed that the spectral shape of pristine P3HT is preserved up to the 1 : 1 composition but exhibits a strong blue shift in the absorption along with the disappearance of the two long wavelength vibronic features, suggesting a disruption of the interchain π–π packing of P3HT for PCBM concentration larger than 50% and poor light harvesting at longer wavelengths [75, 132] as one of the causes for reduction of short–circuit current. In a recent study of the phase behavior by Mueller et al. [80], it has been shown that P3HT: PCBM system is of a simple eutectic nature with a eutectic point at a composition of approximately P3HT: PCBM of 1 : 0.7 and that the maximization of short–circuit photocurrent coincides with a slightly hypoeutectic composition (less P3HT) due to the formation of a nanomorphology that favors charge transport. Although varying results appeared in the literature regarding the composition dependence of charge transport efficiency [80, 129, 144, 145], a composition dependence of electron and hole transport is reported, which must be ultimately related to the nanomorphology of the blend. So, in summary, the optimum photocurrent generation is obtained from the compromise between

1. High light absorption, achieved by maximizing the ordering of P3HT.
2. Efficient charge separation, realized by maximizing the donor–acceptor interface area.
3. Balanced charge transport, accomplished by a balanced hole and electron transport and providing that both components form percolating paths for charge transport towards the electrodes.

The results obtained in this chapter provide microscopic understanding of the nanoscale phase segregation in P3HT: PCBM bulk heterojunction evolving in–situ during drying. The study of P3HT: PCBM blend with different compositions is necessary for improving photovoltaic performance of solar cells made with these blend ratios.

CHAPTER 9

Effect of solvent mixtures on dried P3HT: PCBM blend structure

9.1 Introduction

This chapter discusses the preliminary results of the effect of a different host solvent indane and its mixture with other solvents, such as toluene, o–xylene and chloroform on the structure of dried P3HT: PCBM blend to study solvent–blend interactions on the final structure of P3HT: PCBM blend. Most studies on P3HT: PCBM blend have been done using DCB as the primary solvent [83, 84]. Indane is a common organic solvent which is safer than DCB to human health because of its non–halogenated character. It is a good solvent for P3HT and PCBM like DCB and hence interest in it is increasing. As indane does not spread well on its own on the commonly used substrates for solar cells such as PEDOT:PSS/ITO/Glass, it is mixed with other solvents such as toluene or o–xylene to better its spreading property. Indane and DCB have similar vapor pressure and boiling points. Therefore the drying kinetics of indane and DCB is almost the same and studies conducted on P3HT: PCBM blends in solvent DCB can be easily translated to indane. Preliminary investigations at the Holst Centre in the Netherlands have shown that solar cells made with the mixture of indane and toluene have very good performance of around 2% efficiency.

9.2 Experimental Details

Ex–situ x–ray reflectivity and GIXD measurements were done on dried P3HT: PCBM blend films processed using solvent mixtures of indane with chloroform, o–xylene and toluene, respectively, in ratio 3:1 by volume, in the synchrotron facility ANKA, using a point detector with energy 8 keV. The boiling point of indane is 176.5°C, of chloroform

is 61.2°C, of toluene is 110.6° and of o–xylene is 144°C, whereas that of DCB is 198°C.

9.3 P3HT: PCBM blend structure after processing with indane solvent mixtures

Quantitative structural information on the ordering of P3HT and PCBM perpendicular and parallel to the substrate surface has been obtained in specular reflection and grazing incidence geometries from ex–situ x–ray measurements. In these two geometries the x–ray scattered intensity is exactly probed along q_z and q_{xy}, respectively, to obtain the associated spacing and coherence length of the P3HT layered structure along out–of–plane direction and of the P3HT π–π stacking along in–plane direction. The out–of–plane and in–plane x–ray data are shown in Figure 9.1 a and Figure 9.1 b. The interlayer spacing of P3HT normal to the substrate surface along q_z (Figure 9.1 a) is 16 Å in all the blends processed from the different solvent mixtures. The domain sizes of the different solvent mixtures are also nearly the same — 164 Å for o–xylene, and 152 Å for toluene and chloroform. So the interlayer structure of P3HT is independent of the solvent mixture used to process the P3HT: PCBM blend. GIXD measurements yielded the in–plane P3HT (020) spacing of 3.83 Å for all solvent mixtures (Figure 9.1 b) showing that the spacing of the interchain π–π stacking of P3HT along the substrate in q_{xy} direction does not depend on the type of the solvent used to process the P3HT: PCBM blend. The in–plane correlation lengths are also the same — toluene and chloroform mixtures have correlation lengths of 118 Å , whereas o–xylene mixture has 102 Å . The spacing of PCBM is 4.5 Å and correlation length is 29 Å in all the P3HT: PCBM blends processed from the different solvent mixtures. Hence, the in-plane π–π interchain P3HT packing is independent of the solvent mixtures used to process the P3HT: PCBM blend.

9.4 Conclusions

In this chapter, it has been shown that the solvent indane and its mixture with o–xylene, toluene and chloroform are good substitutes for DCB as the interlayer structure of P3HT along q_z and the interchain P3HT π–π stacking is well developed as in the P3HT: PCBM blend films processed with the solvent DCB, described in the previous chapters. Hence, the solvent mixture of indane with o–xylene and toluene are the safest option for human health due to their non–halogenated character and the final dried P3HT: PCBM blend is also well–suited for good solar cell performance.

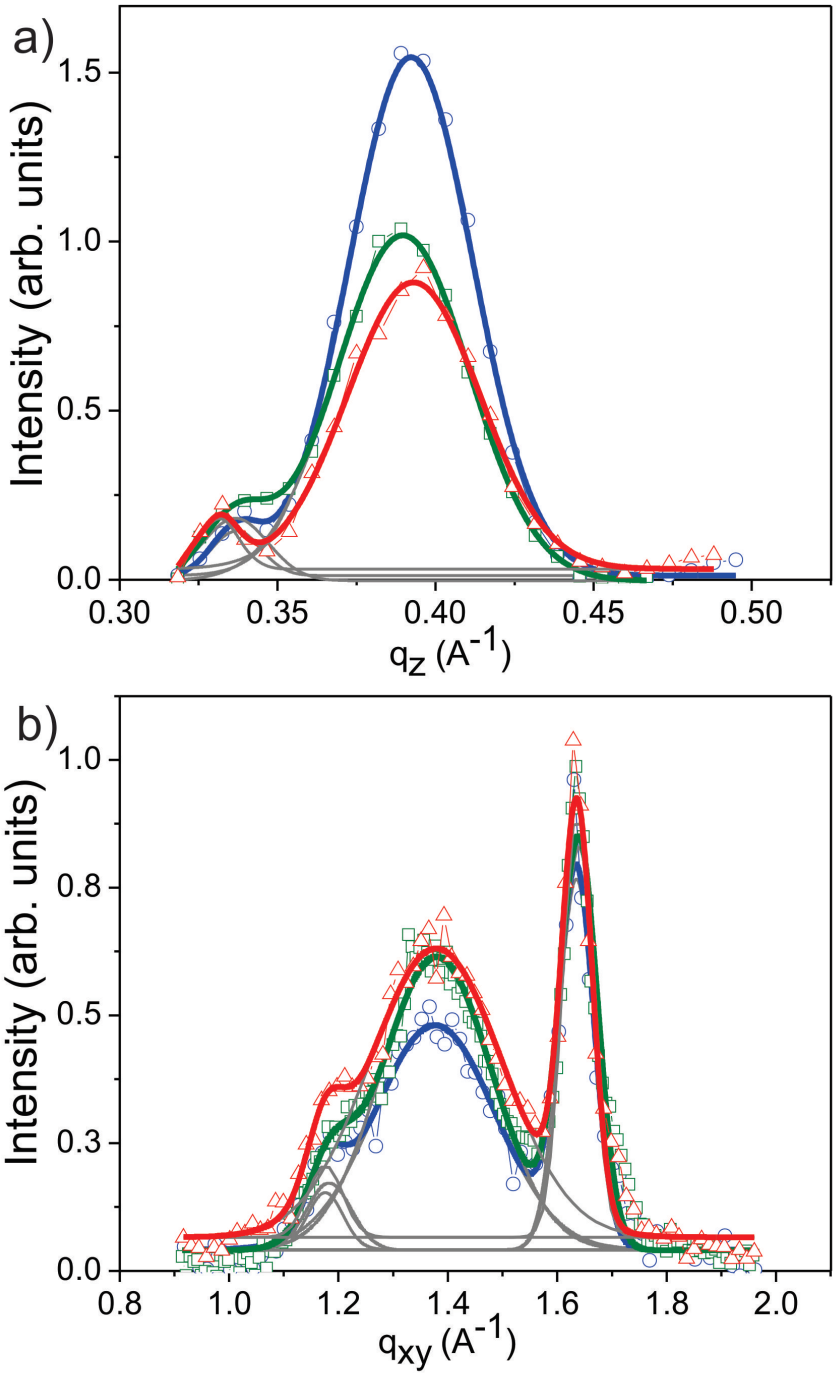

Figure 9.1: (a) X–ray reflectivity (b) GIXD data (symbols) and Gaussian fits (lines) of P3HT: PCBM blends in solvent mixture of indane with xylene (blue circles), toluene (green squares) and chloroform (red triangles), in 3:1 ratio by volume.

CHAPTER 10

Effect of additives on dried P3HT: PCBM blend structure

10.1 Introduction

In this chapter, the effect of the alkanedithiol additive 1,8–octanedithiol on the final P3HT: PCBM dried blend structure has been studied at different drying temperatures using ex–situ GIXD. In the P3HT: PCBM blend, increase in efficiency was observed with the addition of additives [146, 147]. Alkanedithiol, a good solvent for PCBM and not for the polymer P3HT, is absent in thoroughly dried, phase–separated bulk heterojunction films, functioning as "processing additives" for improving the blend morphology [88]. 1,8–octanedithiol has higher boiling point and higher vapor pressure than the host solvent DCB enabling PCBM to stay in solution longer than P3HT (Table 10.1). This enables control over phase separation and morphology of the P3HT: PCBM blend. The effect of additives on P3HT: PCBM blend films have been previously studied [88, 146–148]; however the combined effect of drying temperature and the addition of 1,8–octanedithiol on the final dried P3HT: PCBM blend film has not been studied so far. As discussed in chapter 7, drying temperature has a distinct effect not only on the structural evolution of the P3HT: PCBM blend during its drying, but also on the final dried blend film structure. In this chapter, the combined effect of both the drying tem-

Table 10.1: Comparison of solvent 1,2–dichlorobenzene and additive 1,8–octanedithiol

Material	Boiling Point (°C)	Vapour Pressure at 30°C (Pa)	PCBM solubility (mg/ml)
1,2–dichlorobenzene	198	200	100
1,8–octanedithiol	270	1	19

perature and 1,8–octanedithiol additive on the final P3HT: PCBM blend film structure has been studied.

10.2 Experimental Details

In this chapter, P3HT: PCBM blend films coated on PEDOT:PSS/ITO/Glass substrates and dried at temperatures of 15°C, 25°C and 40°C were studied. Ex–situ x–ray reflectivity and GIXD measurements were conducted in the synchrotron facility ANKA using a point detector with energy 8 keV.

10.3 P3HT: PCBM blend structure with additive 1,8–octanedithiol

Quantitative structural information on the ordering of P3HT and PCBM perpendicular and parallel to the substrate surface has been obtained in specular reflection and grazing incidence geometries from ex–situ x–ray measurements. In these two geometries, the x–ray scattered intensity is probed along q_z and q_{xy} respectively, to obtain the associated spacing and coherence length of the P3HT layered structure along out–of–plane direction and of P3HT interchain π–π stacking along the substrate in the in–plane direction. The out–of–plane and in–plane x–ray data are shown in Figure 10.1 a and Figure 10.1 b. The interlayer P3HT chain spacing normal to the substrate along q_z in the out–of–plane direction at temperatures of 15°C, 25°C and 40°C is 16.3 Å . The respective domain sizes along q_z increased with temperature being 186 Å , 208 Å and 215 Å respectively at 15°C, 25°C and 40°C (Figure 10.1 a). This suggests that with increasing drying temperatures, the mean coherence length of the P3HT layered stack deduced from the full width at half maximum of the P3HT (100) Bragg peak increases, implying better interlayer ordering of the P3HT chains in the out–of–plane direction, which has already been observed in P3HT: PCBM blends with increasing drying temperature in chapter 7.

The in–plane P3HT (020) peak (Figure 10.1 b) signifying interchain P3HT packing along the substrate in the q_{xy} direction arising from the overlapping of the π–π orbitals of the neighboring P3HT chains has spacing 3.82 Å at all the investigated drying temperatures of 15°C, 25°C and 40°C; the respective correlation lengths are 84 Å , 94.5 Å and 72.5 Å showing no specific trend as the drying temperature increases. In chapter 7, it was seen that at low substrate temperatures, the P3HT in–plane correlation length was 118 Å at 15°C, which was much larger than at other drying temperatures: 76 Å at 25°C, 93 Å at 40°C and 72 Å at 80°C. So 1,8–octanedithiol clearly disturbs the interlayer π–π P3HT packing along the substrate in the q_{xy} direction. The PCBM spacing is 4.5 Å at

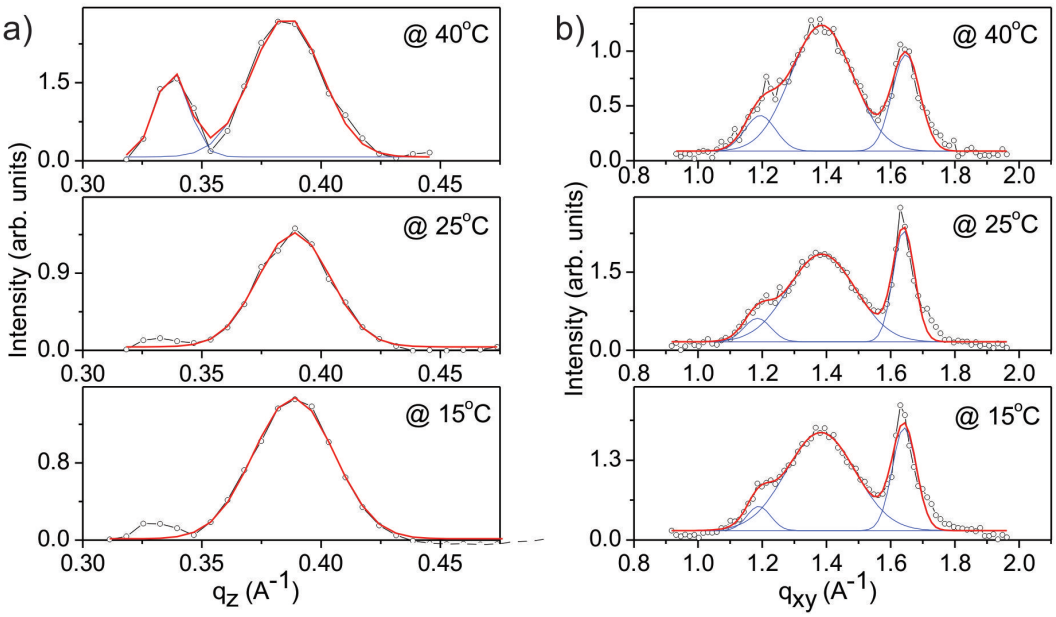

Figure 10.1: (a) X–ray reflectivity of P3HT (100) Bragg peak (b) GIXD data (symbols) with Gaussian fits (lines) of P3HT: PCBM blend films dried at substrate temperatures of 15°C (bottom) 25°C (middle) and 40°C (top). In (b), the left peak is of P3HT (300), middle peak is of PCBM and the right peak is of P3HT (020).

all drying temperatures and the respective correlation lengths are 31 Å at 15°C, 25°C and 40°C, showing no effect of drying temperatures and additives on PCBM. This is in agreement to what was observed previously in chapter 7 at different substrate temperatures, where the PCBM spacing was 4.5 Å and the in–plane correlation length was 30 Å at all the drying temperatures of 15°C, 25°C and 40°C. So the addition of 1,8–octanedithiol does not play an additional role in the final structure of PCBM in the blend.

10.4 Conclusions

In this chapter, the effect of the addition of 1,8–octanedithiol during processing the P3HT: PCBM blend at different drying temperatures has been studied on dried blend films. Although the addition of the additive 1,8–octanedithiol did not bring about any additional structural changes in the interlayer P3HT structure along q_z in the out–of–plane direction, apart from what had already been observed in the chapter 7 due to the different drying temperatures during its processing, however the in–plane inter-

chain π–π packing of P3HT was different from what was observed in the chapter 7. In chapter 7, it was seen that the interchain P3HT π–π in–plane packing was higher at lower drying temperature of 15°C; however in this chapter has been shown that the interchain π–π packing of P3HT is the same at all drying temperatures. This suggests that adding the additive 1,8–octanedithiol improved the interchain P3HT π–π in–plane packing at all drying temperatures, making the addition of 1,8–octanedithiol during the processing of P3HT: PCBM blend advantageous.

CHAPTER 11

Summary and Outlook

11.1 Summary

This thesis was devoted to investigate the real–time structural evolution of a polymer/fullerene blend from solution using in–situ x–ray diffraction. The novelty of the work in this thesis is that the in–situ structural study of a polymer/fullerene blend during its processing has been conducted in real–time for the first time. In this thesis, the structural evolution of the blend of electron–donor semiconducting polymer poly–(3–hexylthiophene) (P3HT) with the electron–acceptor semiconducting fullerene–derivative [6,6]– phenyl– C_{61}– butyric– acid– methyl– ester (PCBM) in a solution in solvent 1,2–dichlorobenzene (DCB) during solvent drying has been studied in–situ using x–ray scattering. Till date, only empirical knowledge exists between the performance of solar cells and the processing parameters used in the photoactive blend. The effect that processing parameters play on the nanostructural evolution of the P3HT: PCBM blend is largely unknown. In this thesis, detailed study of the effect of different technologically relevant processing parameters such as the drying temperature, composition of blend, additives and different solvents and solvent mixtures on the nanostructural evolution of P3HT: PCBM blend during its drying has been studied in–situ using x–ray scattering techniques.

Real-time x–ray scattering study of P3HT: PCBM blends during drying has been used to give novel insight into the crystallisation and the associated evolution of the elastic properties of the blend film during the film formation. The blend microstructure has been shown to emerge from smectic liquid crystal phase to solid phase as the solvent evaporates. The bulk modulus and the bending rigidity modulus of the blend film was calculated at different drying times using diffuse x–ray scattering analysis. This enabled for the first time direct evaluation of the material properties of the blend film as it was drying. This discovery opens the door to a microscopic understanding of

the nanoscale organisation in polymer/fullerene bulk heterojunction solar cells on the basis of phase and drying behaviour, which is key for the direct control of the nanomorphology for optimized photovoltaic performance [149].

Drying temperature has been seen to play a very important effect on the structural evolution of doctor–bladed P3HT: PCBM blends in the transition from wet to solid blend film. Drying the P3HT: PCBM active layer at a lower temperature of 10°C was seen to lead to a good P3HT interchain π–π stacking, broader orientational distribution of P3HT enabled by the slow crystallization kinetics and a restricted phase separation of P3HT and PCBM due to lower molecular mobility giving rise to better nanomorphology with finer interpenetrated network. It had been previously observed that lower drying temperature during processing of the photoactive blend created better performing solar cells; however the nanomorphological and nanostructural reason behind this empirical finding was not known. Based on the study carried out in this thesis, it can be proposed that lowering the substrate temperature during coating and drying is a simple route for optimization of device efficiency in doctor–bladed solar cells [150].

The composition of P3HT: PCBM blend has been observed to be vital for good solar cell performance. The structural evolution of P3HT: PCBM blend film has been observed to depend on the blend composition ratio. The work in this thesis shows that the mosaicity of P3HT decreases with increasing loading of PCBM in the P3HT: PCBM blend suggesting that the interlayer ordering of P3HT improves with higher PCBM content in the blend film. However, the interchain π–π stacking of P3HT deteriorates with increased loading of PCBM. In the P3HT: PCBM blend film with high PCBM content, the formation of a complex P3HT–PCBM structure was observed for the first time [117, 151].

The solvent DCB was used to prepare P3HT: PCBM blend in this thesis. DCB is a halogenated compound not safe for human health. However, the P3HT: PCBM blend structure that develops during drying of DCB leads to good performing solar cells. Search is on for a solvent similar to DCB which can produce the same nanostructure within the P3HT: PCBM blend and hence good performing solar cells and is safe for human health. In this respect, solvent indane and its mixture with o–xylene and toluene are a good substitute for DCB. Preliminary studies being carried out at the Holst Center in Netherlands have shown that the solvent mixtures with indane form good performing solar cells and the solvent mixtures are also safer for human health than DCB. In this thesis, it has been seen that the interchain structure of P3HT normal to the substrate and the interlayer P3HT π–π stacking along the substrate is well developed in the P3HT: PCBM blend films processed with indane mixture as in the blend films processed with solvent DCB. This encourages further investigation into materials for solar cells that

are safe for human health and ecology and have good performance.

The effect of the addition of 1,8–octanedithiol during processing of P3HT: PCBM blend at different drying temperatures has been studied to investigate the interplay of drying temperature and additives on the structure of dried P3HT: PCBM blend films; such a study has been carried out for the first time in this thesis. The addition of 1,8–octanedithiol did not contribute to further changing the interlayer P3HT structure along q_z in the out–of–plane direction; the changes observed were due to the different drying temperatures during processing discussed previously. However the in–plane interchain π–π packing of P3HT was improved at all drying temperatures with the addition of 1,8–octanedithiol. This suggests that the additive improved the interchain P3HT π–π in–plane packing at all drying temperatures, making the addition of 1,8–octanedithiol during the processing of P3HT: PCBM blend advantageous at all drying temperatures.

All the above investigations conducted during this thesis work exhibited delicate ordering of π–π interchain stacking in P3HT along the substrate that depends on drying temperature, composition ratio of P3HT: PCBM blend and the nature of solvent including additives in the solvent used to process the blend. On the other hand, structural ordering of P3HT along [100] direction, which is normal to the substrate surface, is found to be quite resilient. It forms in the early part of drying and improves with higher temperature processing and when P3HT phase segregates from PCBM in the P3HT: PCBM blend. However, this phase segregation of P3HT from PCBM deteriorates the nanophase mixing of their blend and hence photovoltaic efficiency. The resilience of P3HT out–of–plane ordering along [100] was studied here following concepts used in the diffuse scattering study of liquid crystalline phases. The results obtained in this thesis work clearly show that out–of–plane ordering of P3HT along [100] forms first in these films and in–plane interchain π–π P3HT ordering do not form in the initial phase of drying and P3HT: PCBM blend films behave like a liquid crystalline film having long range order in the out–of–plane direction without any ordering in the in–plane direction. In–plane P3HT interchain π–π ordering forms in the later part of drying exhibiting emergence of P3HT (020) peak only if blend ratio and processing temperature are proper. It has also been found here that nanophase mixing of P3HT and PCBM exhibiting higher mosaicity in P3HT (100) peaks and sharper in–plane P3HT (020) peaks provide the red–shift of the solid–state absorption band having vibronic side bands related to P3HT π–π interchain interaction that results in more efficient solar cell performance.

11.2 Outlook

The work embodied in a thesis is never complete — during the course of investigation, many new questions arise which pave the way to interesting studies in the near future. To list a few of the interesting issues involving the P3HT: PCBM blend that I have not been able to tackle but are very interesting to the curious mind, would be the study of the stratification of P3HT and PCBM in the blend film while it is being processed i.e. of the vertical distribution of P3HT and PCBM molecules relative to the surface normal as the solvent is drying. So the study of the air–film interface and of film–substrate interface while the P3HT: PCBM film is drying using in–situ x–ray scattering would be very interesting.

Preliminary surface potential studies on pure P3HT, pure PCBM and P3HT: PCBM films have been performed using the Kelvin Probe Microscope. Further investigation and analysis need to be conducted in order to draw any conclusion on the surface potential behavior.

The in–situ x–ray scattering studies on new polymers and fullerene–derivatives that show better solar cell efficiency can be carried out in a similar fashion as demonstrated in this thesis. Till now, most of the investigation on solar cells have been empirical — new polymers have been developed which have shown better solar cell efficiencies. However, the real nanomorphological and nanostructural reason why some polymers perform better than others have not been well investigated.

The techniques developed in this thesis can be used on any polymer/fullerene blend to study their nanostructural evolution during drying paving the way for a comprehensive study of such systems used extensively in organic polymer solar cells.

Acknowledgements

Finally, I have reached the place where I can thank all who have made it possible for me to write this thesis in the first place.

First of all, I would like to thank **Prof. Helmut Dosch** for giving me the opportunity to work in a fabulous environment. I thank **Prof. Manfred Rühle** for continuing to provide support at the end of my thesis. I thank **Prof. Jörg Wrachtrup** for being the Mitberichter and **Prof. Günter Wunner** for being the Vorsitzender. I would like to thank **Dr. Esther Barrena** for her support and guidance throughout my Phd work. I would like to acknowledge the financial support of Deutsche Forschungsgemeinschaft as this thesis was done within the priority program 1355 "Elementary processes of organic photovoltaics".

I would like to thank my former colleagues **Dr. Claudia Weiss**,**Dr. Dimas Feldermann**, **Dr. Dipak Goswami**, **Dr. Yi Zhang**, **Dr. XueNa Zhang**, **Dr. Tobias Krauss**, **Dr. Carmen Munuera**, **Dr. Ayse Turak**, **Ajay Perumal**, **Jonathan Heidkamp**, **Peter Lienerth** and **Minh Nguyen** for all the help, support and the fun times that we have had in and outside the lab. I would specially like to thank **Felix Maye**, a co-phd student in my lab and an awesome friend who was always there for support. Also, not to forget my colleagues in my department — **Navid Khorshidi**, **Dr. Alejandro Diaz-Ortiz**, **Dr. Alina Vlad**, **Dr. Melissa Delheusy**, **Dr. Janos Major** to name a few, with whom I have spent very good times. I would like to thank the wonderful friends that I made here — **Ivana Krkljus**, **Dr. Ranu Bhatt**, **Dr. Emila Panda** and **Dr. Gurneet Kaur** for making my stay in Stuttgart so very enjoyable. I would like to thank my collaborators and co–phd students **Benjamin Schmidt–Hansberg** and **Michael Klein** from the Karlsruhe Institute of Technology, working with whom was very enjoyable. During the course of many synchrotron experiments and discussions, we became very good friends. I would specially like to thank Benjamin for the wonderful discussions that we had about Science and life in general and for making the Phd time so wonderful.

I would like to thank **Mr. Ralph Weigel** at ANKA for being of immense help and support at the MPI–MF beamline in ANKA. At the same note, I would like to thank **Dr.**

Alexei Vorobiev of the ID–10B beamline at ESRF for his support and sharing of immense knowledge while we conducted experiments there. I would also like to thank **Mr. Taufan Zimmer** and **Mr. Peter Schützendübe** for all the technical help. I would profusely thank **Mrs. Claudia Süssdorff**, the department secretary, for all the administrative support that she has given me. She has always done more than expected for everyone, especially making the life of foreigners in the department very easy. Over the years that I have spent in the institute, I have become very close to her.

I am grateful to my beloved parents — **Prof. Milan Kumar Sanyal** and **Mrs. Alpana Sanyal** and sister **Madhumanti Sanyal** for their love, care and concern which made crisis situations easy for me to tide over. I would also like to thank **Kalpana Mandal** for being the good friend that she is to me. Saving the best for the last, I would like to express my gratitude to my dearest and best friend **Ankur Singh Gaur** and now my husband, who has been an unwavering support to me during the years I spent in my thesis work; he gave me strength and courage to overcome contrary situations and made me believe that bad times were not to be there forever.

Without all the love and support from everyone, this work would not have been possible.

References

[1] Nathan S. Lewis. Toward cost-effective solar energy use. *Science*, 315:798–801, 2007. doi: 10.1126/science.1137014.

[2] Susan Solomon, Gian-Kasper Plattner, Reto Knutti, and Pierre Friedlingstein. Irreversible climate change due to carbon dioxide emissions. *Proceedings of the National Academy of Sciences of the United States of America*, 106:1704–1709, 2009. doi: 10.1073/pnas.0812721106.

[3] Jianhua Zhao, Aihua Wang, Martin A. Green, and Francesca Ferrazza. Novel 19.8% efficient "honeycomb" textured multicrystalline and 24.4% monocrystalline silicon solar cell. *Applied Physics Letters*, 73:1991–1993, 1998. doi: 10.1063/1.122345.

[4] Martin A. Green, Keith Emery, Yoshihiro Hishikawa, and Wilhelm Warta. Solar cell efficiency tables (version 35). *Progess in Photovoltaics*, 18:144–150, 2010. doi: 10.1002/pip.974.

[5] Russell Gaudiana and Christoph J. Brabec. Fantastic plastic. *Nature Photonics*, 2: 287–289, 2008. doi: 10.1038/nphoton.2008.69.

[6] Frederik C. Krebs, Suren A. Gevorgyan, and Jan Alstrup. A roll–to-roll process to flexible polymer solar cells: model studies, manufacture and operational stability studies. *Journal of Materials Chemistry*, 19:5442–5451, 2009. doi: 10.1039/b823001c.

[7] Frederik C. Krebs. Fabrication and processing of polymer solar cells: A review of printing and coating techniques. *Solar Energy Materials and Solar Cells*, 93:394–412, 2009. doi: 10.1016/j.solmat.2008.10.004.

[8] Frederik C. Krebs. Polymer solar cell modules prepared using roll–to–roll methods: knife–over–edge coating, slot–die coating and screen printing. *Solar Energy Materials and Solar Cells*, 93:465–475, 2009. doi: 10.1016/j.solmat.2008.12.012.

[9] M. Jϕgensen, K. Norrman, and F.C. Krebs. Stability/degradation of polymer

solar cells. *Solar Energy Materials and Solar Cells*, 92:686–714, 2008. doi: 10.1016/j.solmat.2008.01.005.

[10] Hsiang-Yu Chen, Jianhui Hou, Shaoqing Zhang, Yongye Liang, Guanwen Yang, Yang Yang, Luping Yu, Yue Wu, and Gang Li. Polymer solar cells with enhanced open–circuit voltage and efficiency. *Nature Photonics*, 3:649–653, 2009. doi: 10.1021/jp810798z.

[11] Sung Heum Park, Anshuman Roy, Serge Beaupre, Shinuk Cho, Nelson E. Coates, Ji Sun Moon, Daniel Moses, Mario Leclerc, Kwanghee Lee, and Alan J. Heeger. Bulk heterojunction solar cells with internal quantum efficiency approaching 100%. *Nature Photonics*, 3:297–303, 2009. doi: 10.1038/nphoton.2009.69.

[12] Yongye Liang, Zheng Xu, Jiangbin Xia, Szu-Ting Tsai, Yue Wu, Gang Li, Claire Ray, and Luping Yu. For the bright future – bulk heterojunction polymer solar cells with power conversion efficiency of 7.4%. *Advanced Materials*, 22:E135–E138, 2010. doi: 10.1002/adma.200903528.

[13] Jenny Nelson. Solar cells by self-assembly? *Science*, 293:1059–1060, 2001.

[14] A. Pivrikas, N.S. Sariciftci, G. Juska, and R. Oesterbacka. A review of charge transport and recombination in polymer/fullerene organic solar cells. *Progress in Photovoltaics:Research and Applications*, 15:677–696, 2007. doi: 10.1002/pip.791.

[15] Robert F. Service. Can the upstarts top silicon? *Science*, 319:718–720, 2008.

[16] Barry C. Thompson and Jean M. J. Frechet. Polymer–fullerene composite solar cells. *Angewandte Chemie International Edition*, 47:58–77, 2008. doi: 10.1002/anie.200702506.

[17] J. J. M. Halls, C. A. Walsh, N. C. Greenham, E. A. Marseglia, R. H. Friend, S. C. Moratti, and A. B. Holmes. Efficient photodiodes from interpenetrating polymer networks. *Nature*, 376:498–500, 1995. doi: 10.1038/376498a0.

[18] G. Yu, J. Gao, J.C. Hummelen, F. Wudl, and A.J. Heeger. Polymer photovoltaic cells: Enhanced efficiencies via a network of internal donor–acceptor heterojunctions. *Science*, 270:1789–1791, 1995. doi: 10.1126/science.270.5243.1789.

[19] Arjan Pieter Zoombelt. *π–conjugated polymers for Photovoltaics*. PhD thesis, Eindhoven University of Technology, 2009.

[20] U. Croatto, S. Bezzi, and E. Bua. The crystal structure of p-dichlorobenzene. *Acta Crystallographica*, 5:825–829, 1952. doi: 10.1107/S0365110X52002203.

[21] N.S. Sariciftci, L. Smilowitz, A.J. Heeger, and F. Wudl. Photoinduced electron transfer from a conducting polymer to buckminsterfullerene. *Science*, 258:1474–1476, 1992. doi: 10.1126/science.258.5087.1474.

[22] Christoph J. Brabec, Niyazi Serdar Sariciftci, and Jan C. Hummelen. Plastic solar cells. *Advanced Functional Materials*, 11:15–26, 2001. doi: 10.1002/1616-3028(200102)11:1<15::AID-ADFM15>3.0.CO;2-A.

[23] Antoine Kahn, Norbert Koch, and Weiying Gao. Electronic structure and electrical properties of interfaces between metals and π-conjugated molecular films. *Journal of Polymer Science: Part B: Polymer Physics*, 41:2529–2548, 2003. doi: 10.1002/polb.10642.

[24] Simone Dal Zilio. *Innovative solutions in organic photovoltaic devices*. PhD thesis, UNIVERSITÀ DEGLI STUDI DI PADOVA, 2009.

[25] A.G. Brian and C.H. Mark. Comparing organic to inorganic photovoltaic cells: Theory, experimental and simulation. *Journal of Applied Physics*, 93:3605–3614, 2003. doi: 10.1063/1.1544413.

[26] Travis L. Benanti and D. Venkataraman. Review: Organic solar cells: An overview focusing on active layer morphology. *Photosynthesis Research*, 87:73–81, 2006. doi: 10.1007/s11120-005-6397-9.

[27] Brian A. Gregg. Excitonic solar cells. *The Journal of Physical Chemistry B*, 107:4688–4698, 2003. doi: 10.1021/jp022507x.

[28] V.I. Arkhipov and H. Baessler. Exciton dissociation and charge photogeneration in pristine and doped conjugated polymers. *Physics Status Solidi (a)*, 201:1152–1187, 2004. doi: 10.1002/pssa.200404339.

[29] A. Haugeneder, M. Neges, C. Kallinger, W. Spirkl, U. Lemmer, J. Feldmann, U. Scherf, E. Harth, A. Guel, and K. Muelen. Excitonic diffusion and dissociation in conjugated polymer/fullerene blends and heterostructures. *Physical Review B*, 59:15346–15351, 1999. doi: 10.1103/PhysRevB.59.15346.

[30] M. Theander, A. Yartsev, D. Zigmantas, V. Sundstroem, W. Mammo, M.R. Andersson, and O. Inganaes. Photoluminescence quenching at a polythiophene/c60 heterojunction. *Physical Review B*, 61:12957–12963, 2000. doi: 10.1103/PhysRevB.61.12957.

[31] Thomas Stübinger and Wolfgang Brütting. Exciton diffusion and optical interference in organic donor–acceptor photovoltaic cells. *Journal of Applied Physics*, 90:3632–3641, 2001. doi: 10.1063/1.1394920.

[32] B. Paci, A. Generosi, V. Rossi Albertini, R. Generosi, P. Perfetti, R. de Bettignies, and C. Sentein. Time-resolved morphological study of bulk heterojunction films for efficient organic solar devices. *Journal of Physical Chemistry C*, 112:9931–9936, 2008. doi: 10.1021/jp801674v.

[33] David Cahen and Antoine Kahn. Electron energetics at surfaces and interfaces: Concepts and experiments. *Advanced Materials*, 15:271–277, 2003. doi: 10.1002/adma.200390065.

[34] Patrick Wallace Parkinson. *Ultrafast Electronic Processes at Nanoscale Organic-Inorganic Semiconductor Interfaces*. PhD thesis, University of Oxford, 2008.

[35] Wanzhu Cai, Xiong Gong, and Yong Cao. Polymer solar cells: Recent development and possible routes for improvement in the performance. *Solar Energy Materials and Solar Cells*, 94:114–127, 2010. doi: 10.1016/j.solmat.2009.10.005.

[36] C. Winder and N.S. Sariciftci. Low bandgap polymers for photon harvesting in bulk heterojunction solar cells. *Journal of Materials Chemistry*, 14:1077–1086, 2004. doi: 10.1039/B306630D.

[37] Anthony J. Mofta, Kathy L. Rowen, Thomas H. Reilly, Manuel J. Romero, and Jao van de Lagemaat. Plasmon–enhanced solar energy conversion in organic bulk heterojunction photovoltaics. *Applied Physics Letters*, 92:013504–013506, 2008. doi: 10.1063/1.2823578.

[38] Jin Young Kim, Kwanghee Lee, Nelson E. Coates, Daniel Moses, Thuc-Quyen Nguyen, Mark Dante, and Alan J. Heeger. Efficient tandem polymer solar cells fabricated by all-solution processing. *Science*, 317:222–225, 2007. doi: 10.1126/science.1141711.

[39] A. Hadipour, B. de Boer, and P.W.M. Blom. Organic tandem and multi–junction solar cells. *Advanced Functional Materials*, 18:169–181, 2008. doi: 10.1002/adfm.200700517.

[40] M.J. Winokur, D. Spiegel, Y. Kim, S. Hotta, and A.J. Heeger. Structural and absorption studies of the thermochromic transition in poly(3-hexylthiophene). *Synthetic Metals*, 28:C419–C426, 1989. doi: 10.1016/0379-6779(89)90554-7.

[41] Mario Leclerc, Francisco Martinez Diaz, and Gerhard Wegner. Structural analysis of poly(3-alkylthiophene)s. *Macromolecular Chemistry and Physics*, 190:3105–3116, 1989. doi: 10.1002/macp.1989.021901208.

[42] Kohji Tashiro, Keiko Ono, Yasuhisa Minagawa, Masamichi Kubayashi, Tsuyoshi Kawai, and Katsumi Yoshino. Structure and thermochromic solid-state phase transition of poly(3-alkylthiophene). *Journal of Polymer Science: Part B: Polymer Physics*, 29:1223–1233, 1991. doi: 10.1016/0379-6779(93)90952-S.

[43] Sudip Malik and Arun K. Nandi. Crystallization mechanism of regioregular poly(3-alkyl thiophene)s. *Polymer Physics*, 40:2073–2085, 2002. doi: 10.1002/polb.10272.

[44] Kyo Jin Ihn, Jeff Moulton, and Paul Smith. Whiskers of poly (3-alkylthiophene)s. *Polymer Physics*, 31:735–742, 2003. doi: 10.1002/polb.1993.090310614.

[45] Youngkyoo Kim, Jenny Nelson, James R. Durrant, Donal D. C. Bradley, Kyuyoung Heo, Jinwoo Park, Hwajeong Kim, Iain McCulloch, Martin Heeney, Moonhor Ree, and Chang-Sik Ha. Polymer chain/nanocrystal ordering in thin films of regioregular poly(3- hexylthiophene) and blends with a soluble fullerene. *Soft Matter*, 3:117–121, 2007. doi: 10.1039/b610730c.

[46] Serap Guenes, Helmut Neugebauer, and Niyazi Serdar Sariciftci. Conjugated polymer-based organic solar cells. *Chemical Reviews*, 107:1324–1338, 2007. doi: 10.1021/cr050149z.

[47] Martin Brinkmann and Jean-Claude Wittmann. Orientation of regioregular poly(3-hexylthiophene) by directional solidification: A simple method to reveal the semicrystalline structure of a conjugated polymer. *Advanced Materials*, 18: 860–863, 2006. doi: 10.1002/adma.200501838.

[48] Mao-Yuan Chiu, U-Ser Jeng, Chiu-Hun Su, Keng S. Liang, and Kung-Hwa Wei. Simultaneous use of small- and wide-angle x-ray techniques to analyze nanometerscale phase separation in polymer heterojunction solar cells. *Advanced Materials*, 20:2573–2578, 2008. doi: 10.1002/adma.200703097.

[49] Martin Brinkmann and Patrice Rannou. Molecular weight dependence of chain packing and semicrystalline structure in oriented films of regioregular poly(3-hexylthiophene) revealed by high-resolution transmission electron microscopy. *Macromolecules*, 42:1125–1130, 2009. doi: 10.1021/ma8023415.

[50] Jun Zhao, Ann Swinnen, Guy Van Assche, Jean Manca, Dirk Vanderzande, and Bruno Van Mele. Phase diagram of p3ht/pcbm blends and its implication for the stability of morphologyjun zhao. *Journal of Physical Chemistry C*, 113:1587–1591, 2009. doi: 10.1021/jp804151a.

[51] Uladzimir Zhokhavets. *Composite conjugated polymer/fullerene films: structure-property relation*. PhD thesis, Technische Universitaet Illmenau, 2005.

[52] Wanli Ma, Cuiying Yang, Xiong Gong, Kwanghee Lee, and Alan J. Heeger. Thermally stable, efficient polymer solar cells with nanoscale control of the interpenetrating network morphology. *Advanced Functional Materials*, 15:1617–1622, 2005. doi: 10.1002/adfm.200500211.

[53] Gilles Dennler, Markus C. Scharber, and Christoph J. Brabec. Polymer-fullerene bulk-heterojunction solar cells. *Advanced Materials*, 21:1323–1338, 2009. doi: 10.1002/adma.200801283.

[54] Tobias Erb, Uladzimir Zhokhavets, Gerhard Gobsch, Sofiya Raleva, Bernd Stuehn, Pavel Schilinsky, Christoph Waldauf, and Christoph J. Brabec. Correlation between structural and optical properties of composite polymer/fullerene films for organic solar cells. *Advanced Functional Materials*, 15:1193–1196, 2005. doi: 10.1002/adfm.200400521.

[55] Jinsong Huang, Gang Li, and Yang Yang. Influence of composition and heat-treatment on the charge transport properties of poly(3-hexylthiophene) and [6,6]-phenyl c61-butyric acid methyl ester blends. *Applied Physics Letters*, 87:112105–112107, 2005. doi: 10.1063/1.2045554.

[56] Pavel Schilinsky, Udom Asawapirom, Ullrich Scherf, Markus Biele, and Christoph J. Brabec. Influence of the molecular weight of poly(3-hexylthiophene) on the performance of bulk heterojunction solar cells. *Chemistry of Materials*, 17:2175–2180, 2005. doi: 10.1021/cm047811c.

[57] R.J. Kline, M.D. McGehee, E.N. Kadnikova, J. Liu, and J.M.J. Frechet. Controlling the field-effect mobility of regioregular polythiophene by changing the molecular weight. *Advanced Materials*, 15:1519–1522, 2003. doi: 10.1002/adma.200305275.

[58] R. Joseph Kline, Michael D. McGehee, Ekaterina N. Kadnikova, Jinsong Liu, NewAuthor5, and Michael F. Toney. Dependence of regioregular poly(3-hexylthiophene) film morphology and field-effect mobility on molecular weight. *Macromolecules*, 38:3312–3319, 2005. doi: 10.1021/ma047415f.

[59] Jang Jo, Seok-Soon Kim, Seok-In Na, Byung-Kwan Yu, and Dong-Yu Kim. Time-dependent morphology evolution by annealing processes on polymer:fullerene blend solar cells. *Advanced Functional Materials*, 19:866–874, 2009. doi: 10.1002/adfm.200800968.

[60] Jang Jo, Seok-In Na, Seok-Soon Kim, Tae-Woo Lee, Youngsu Chung, Seok-Ju Kang, Doojin Vak, and Dong-Yu Kim. Three-dimensional bulk heterojunction morphology for achieving high internal quantum efficiency in polymer solar cells. *Advanced Functional Materials*, 19:2398–2406, 2009. doi: 10.1002/adfm.200900183.

[61] Le Huong Nguyen, Harald Hoppe, Tobias Erb, Serap Guenes, Gerhard Gobsch, and Niyazi Serdar Sariciftci. Effects of annealing on the nanomorphology and performance of poly(alkylthiophene):fullerene bulk-heterojunction solar cells. *Advanced Functional Materials*, 17:1071–1078, 2007. doi: 10.1002/adfm.200601038.

[62] Youngkyoo Kim, Steffan Cook, Sachetan M. Tuladhar, Stelios A. Choulis, Jenny Nelson, James R. Durrant, Donal D. C. Bradley, Mark Giles, Iain McCulloch, Chang-Sik Ha, and Moonhor Ree. A strong regioregularity effect in self-organizing conjugated polymer films and high-efficiency polythiophene:fullerene solar cells. *Nature Materials*, 5:197–203, 2006. doi: 10.1038/nmat1574.

[63] R.C. Hiors, R. de Bettignies de Bettignies, J. Leroy, S. Bailly, M. Firon, C. Sentein, A. Khoukh, H. Preud'homme, and C. Dagron-Lartigau. High molecular weights, polydispersities, and annealing temperatures in the optimization of bulk-heterojunction photovoltaic cells based on poly(3-hexylthiophene) or poly(3-butylthiophene). *Advanced Functional Materials*, 16:2263–2273, 2006. doi: 10.1002/adfm.200600005.

[64] Wanli Ma, Jin Young Kim, Kwanghee Lee, and Alan J. Heeger. Effect of the molecular weight of poly(3-hexylthiophene) on the morphology and performance of polymer bulk heterojunction solar cells. *Macromolecular Rapid Communications*, 28:1776–1780, 2007. doi: 10.1002/marc.200700280.

[65] H. Sirringhaus, P. J. Brown, R. H. Friend, M. M. Nielsen, K. Bechgaard, B. M. W. Langeveld-Voss, A. J. H. Spiering, R. A. J. Janssen, E.W. Meijer, P. Herwig, and D. M. De Leeuw. Two-dimensional charge transport in self-organized, high-mobility conjugated polymers. *Nature*, 401:685–688, 1999. doi: 10.1038/44359.

[66] Xiaoqing Jiang, Rahul Patil, Yutaka Harima, Joji Ohshita, and NewAuthor5. Influences of self-assembled structure on mobilities of charge carriers in π-conjugated polymers. *Journal of Physical Chemistry B*, 109:221–229, 2005. doi: 10.1021/jp0460994.

[67] T.J. Savenije, J.E. Kroeze, X. Yang, and J. Loos. The effect of thermal treatment on the morphology and charge carrier dynamics in a polythiophene-fullerene bulk

heterojunction. *Advanced Functional Materials*, 15:1260–1266, 2005. doi: 10.1002/adfm.200400559.

[68] Valentin D. Mihailetchi, Hangxing Xie, Bert de Boer, Lacramioara M. Popescu, Jan C. Hummelen, Paul W.M. Blom, and L. Jan Anton Koster. Origin of the enhanced performance in poly(3-hexylthiophene): [6,6]-phenyl c61-butyric acid methyl ester solar cells upon slow drying of the active layer. *Applied Physics Letters*, 89:012107–012109, 2006. doi: 10.1063/1.2212058.

[69] Xiaoniu Yang, Joachim Loos, Sjoerd C. Veenstra, Wiljan J. H. Verhees, Martijn M. Wienk, Jan M. Kroon, Matthias A. J. Michels, and Rene A. J. Janssen. Nanoscale morphology of high performance polymer solar cells. *NanoLetters*, 5:579–583, 2005. doi: 10.1021/n1048120i.

[70] A. Pivrikas, G. Juska, A.J. Mozer, M. Scharber, K. Arlauskas, N.S. Sariciftci, H. Stubb, and R. Oesterbacka. Bimolecular recombination coefficient as a sensitive testing parameter for low-mobility solar-cell materials. *Physical Review Letters*, 94:176806–176809, 2005. doi: 10.1103/PhysRevLett.94.176806.

[71] Xin Ai, Matthew C. Beard, Kelly P. Knutsen, Sean E. Shaheen, Garry Rumbles, and Randy J. Ellingson. Photoinduced charge carrier generation in a poly(3-hexylthiophene) and methanofullerene bulk heterojunction investigated by time-resolved terahertz spectroscopy. *Journal of Physical Chemistry B*, 110:25462–25471, 2006. doi: 10.1021/jp065212i.

[72] Wanli Ma, Cuiying Yang, Xiong Gong, and Alan J. Heeger. Thermally stable, efficient polymer solar cells with nanoscale control of the interpenetrating network morphology. *Advanced Functional Materials*, 15:1617–1622, 2005. doi: 10.1002/adfm.200500211.

[73] Yun Zhao, Zhiyuan Xie, Yao Qu, Yanhou Geng, and Lixiang Wang. Solvent-vapor treatment induced performance enhancement of poly(3-hexylthiophene):methanofullerene bulk-heterojunction photovoltaic cells. *Applied Physics Letters*, 90:043504–043506, 2007. doi: 10.1063/1.2434173.

[74] Gang Li, Vishal Shrotriya, Jinsong Huang, Yan Yao, Tom Moriarty, Keith Emery, and Yang Yang. High-efficiency solution processable polymer photovoltaic cells by self-organization of polymer blends. *Nature Materials*, 4:864–868, 2005. doi: 10.1038/nmat1500.

[75] Gang Li, Yan Yao, H. Yang, Vishal Shrotriya, G. Yang, and Yang Yang. "solvent annealing" effect in polymer solar cells based on poly(3–hexylthiophene)

and methanofullerenes. *Advanced Functional Materials*, 17:1636–1644, 2007. doi: 10.1002/adfm.200600624.

[76] Harald Hoppe, T. Glatzel, M. Niggemann, W. Schwinger, F. Schaeffler, A. Hinsch, M. Ch. Lux-Steiner, N.S. Sariciftci, NewAuthor9, and NewAuthor10. Efficiency limiting morphological factors of mdmo-ppv:pcbm plastic solar cells. *Thin Solid Films*, 511:587–592, 2006.

[77] Chih-Wei Chu, Hoichang Yang, Wei-Jen Hou, Jinsong Huang, Gang Li, and Yang Yang. Control of the nanoscale crystallinity and phase separation in polymer solar cells. *Applied Physics Letters*, 92:103306–103308, 2008. doi: 10.1063/1.2891884.

[78] Tzung-Fang Guo, Ten-Chin Wen, Georgi L'vovich Pakhomov, Xing-Guo Chin, Siou-Hong Liou, Pei-Hong Yeh, and Cheng-Hsien Yang. Effects of film treatment on the performance of poly(3-hexylthiophene)/soluble fullerene-based organic solar cells. *Thin Solid Films*, 516:3138–3142, 2008. doi: 10.1016/j.tsf.2007.08.066.

[79] A. Zen, J. Pflaum, S. Hirschmann, W. Zhuang, F. Jaiser, U. Asawapirom, J.P. Rabe, U. Scherf, and D. Neher. Effect of molecular weight and annealing of poly(3-hexylthiophene)s on the performance of organic field-effect transistors. *Advanced Functional Materials*, 14:757–764, 2004. doi: 10.1002/adfm.200400017.

[80] Christian Mueller, Toby A. M. Ferenczi, Mariano Campoy-Quiles, Jarvist M. Frost, Donald D.C. Bradley, Paul Smith, Natalie Stingelin-Stutzmann, and Jenny Nelson. Binary organic photovoltaic blends : A simple rationale for optimum conditions. *Advanced Materials*, 20:3510–3515, 2008. doi: 10.1002/adma.200800963.

[81] M.S. White, D.C. Olson, S.E. Shaheen, N. Kopidakis, and D.S. Ginley. Inverted bulk-heterojunction organic photovoltaic device using a solution-derived zno underlayer. *Applied Physics Letters*, 89:143517–143519, 2006. doi: 10.1063/1.2359579.

[82] Jeffrey Peet, Nam Sung Cho, Sang Kyu Lee, and Guillermo C. Bazan. Transition from solution to the solid state in polymer solar cells cast from mixed solvents. *Macromolecules*, 41:8655–8659, 2008. doi: 10.1021/ma801945h.

[83] Adam J. Moule and Klaus Meerholz. Morphology control in solution-processed bulk-heterojunction solar cell mixtures. *Advanced Functional Materials*, 19:1–9, 2009. doi: 10.1002/adfm.200900775.

[84] Kenji Kawano, Jun Sakai, Masayuki Yahiro, and Chihaya Adachi. Effect of solvent on fabrication of active layers in organic solar cells based on poly(3-

hexylthiophene) and fullerene derivatives. *Solar Energy Materials and Solar Cells*, 93:514–518, 2009. doi: 10.1016/j.solmat.2008.11.003.

[85] Jeffery Peet, C. Soci, R.C. Coffin, T.Q. Nguyen, A. Mikhailovsky, Daniel Moses, and Guillermo C. Bazan. Method for increasing the photoconductive response in conjugated polymer/fullerene composites. *Applied Physics Letters*, 89:252105–252107, 2006. doi: 10.1063/1.2408661.

[86] Jeffery Peet, J.Y. Kim, Nelson E. Coates, Wang Li Ma, Daniel Moses, Alan J. Heeger, and Guillermo C. Bazan. Efficiency enhancement in low bandgap polymer solar cells by processing with alkanedithiols. *Nature Materials*, 6:497–500, 2007. doi: 10.1038/nmat1928.

[87] Wenli Wang, HongBin Wu, Cuiying Yang, Chan Luo, Yong Zhang, JunWu Chen, Yong Cao, et al. High-efficiency polymer photovoltaic devices from regioregular-poly(3-hexylthiophene-2,5-diyl) and [6,6]-phenyl-c61-butyric acid methyl ester processed with oleic acid surfactant. *Applied Physics Letters*, 90:183512–183514, 2007. doi: 10.1063/1.2735937.

[88] Yan Yao, Jianhui Hou, Zheng Xu, Gang Li, and Yang Yang. Effects of solvent mixtures on the nanoscale phase separation in polymer solar cells. *Advanced Functional Materials*, 18:1783–1789, 2008. doi: 10.1002/adfm.200701459.

[89] T. Piok, S. Gamerith, C. Gadermaier, H. Plank, F.P. Wenzl, S. Patil, R. Montenegro, T. Kietzke, D. Neher, U. Scherf, K. Landfester, and E.J.W. List. Organic light-emitting devices fabricated from semiconducting nanospheres. *Advanced Materials*, 15:800–804, 2003. doi: 10.1002/adma.200304253.

[90] Katharina Landfester. Polyreactions in miniemulsions. *Macromolecular Rapid Communications*, 22:896–936, 2001. doi: 10.1002/1521-3927(20010801)22:12<896::AID-MARC896>3.0.CO;2-R.

[91] Katharina Landfester. The generation of nanoparticles in miniemulsions. *Advanced Materials*, 13:765–768, 2001. doi: 10.1002/1521-4095(200105)13:10<765::AID-ADMA765>3.0.CO;2-F.

[92] K. Landfester, R. Montenegro, U. Scherf, R. Guentner, U. Asawapirom, S. Patil, D. Neher, and T. Kietzke. Semiconducting polymer nanospheres in aqueous dispersion prepared by a miniemulsion process. *Advanced Materials*, 14:651–655, 2002. doi: 10.1002/1521-4095(20020503)14:9<651::AID-ADMA651>3.0.CO;2-V.

[93] B.E. Warren. *X–ray Diffraction*. Addison-Wesley Educational, 1968.

[94] A. Guinier. *X-Ray Diffraction: In Crystals, Imperfect Crystals, and Amorphous Bodies*. Dover Publications, 1994.

[95] Vaclav Holy, Ullrich Pietsch, and Tilo Baumbach. *High–Resolution X–ray Scattering from Thin Films and Multilayers*. Springer, 1998.

[96] Monamie Sanyal. Structure and morphology of cobalt phthalocyanine organic films on silicon dioxide. Master's thesis, Universitaet Stuttgart, 2007.

[97] L.G. Parratt. Surface studies of solids by total reflection of x-rays. *Physical Review*, 95:359–369, 1954. doi: 10.1103/PhysRev.95.359.

[98] Helmut Dosch. *Critical Phenomena at Surfaces and Interfaces Evanescent X–ray and Neutron Scattering*. Springer, 1992.

[99] H. Rhan and J. Peisl. Shift of the bragg position in grazing-incidence diffraction. *Zeitschrift fuer Physik B*, 100:365–368, 1996. doi: 10.1007/s002570050134.

[100] Y. Hu and L.J. Martinez-Miranda. Study of the buried interface behavior of liquid crystal thin films using synchrotron radiation and grazing incidence x-ray scattering mode. *Materials Research Society Symposium Proceedings*, 590:201–205, 2000.

[101] J.K. Basu and M.K. Sanyal. Ordering and growth of langmuir–blodgett films: X-ray scattering studies. *Physics Reports*, 363:1–84, 2002. doi: 10.1016/S0370-1573(01)00083-7.

[102] Christopher M. Spillmann, John H. Konnert, Jeffrey R. Deschamps, Jawad Naciri, and Banahalli R. Ratna. Molecular packing in electroclinic liquid crystal elastomer films. *Chemistry of Materials*, 20:6130–6139, 2008. doi: 10.1021/cm801335j.

[103] Masafumi Fukuto, Oleg Gang, Kyle J. Alvine, Benjamin M. Ocko, and Peter S. Pershan. Wetting of liquid-crystal surfaces and induced smectic layering at a nematic-liquid interface: An x-ray reflectivity study. *Physical Review E*, 77:031607–031617, 2008. doi: 10.1103/PhysRevE.77.031607.

[104] Metin Tolan. *X–ray scattering from Soft–Matter Thin Films*. Springer, 1998.

[105] J Daillant and M Alba. High-resolution x-ray scattering measurements: I. surfaces. *Reports on Progress in Physics*, 63:1725–1777, 2000. doi: 10.1088/0034-4885/63/10/203.

[106] M.K. Sanyal, S.K. Sinha, K.G. Huang, and B.M. Ocko. X-ray-scattering study of capillary-wave fluctuations at a liquid surface. *Physical Review Letters*, 66:628–631, 1991. doi: 10.1103/PhysRevLett.66.628.

[107] Wim H. de Jeu, Boris I. Ostrovskii, and Arcadi N. Shalaginov. Structure and fluctuations of smectic membranes. *Reviews of Modern Physics*, 75:181–235, 2003. doi: 10.1103/RevModPhys.75.181.

[108] P.M. Chaikin and T.C. Lubensky. *Principles of Condensed Matter Physics*. Cambridge University Press, 1995.

[109] A. Caille. Remarks on x-ray scattering on smectlcs. *C.R. Acad. Sci. Paris*, 274B: 891–893, 1972.

[110] J. Als-Nielsen, J. D. Litster, R. J. Birgeneau, M. Kaplan, C. R. Safinya, A. Lindegaard-Andersen, and S. Mathiesen. Observation of algebraic decay of positional order in a smectic liquid crystal. *Physical Review B*, 22:312–320, 1980. doi: 10.1103/PhysRevB.22.312.

[111] Michael L. Chabinyc, Michael F. Toney, R. Joseph Kline, Iain McCulloch, and Martin Heeney. X-ray scattering study of thin films of poly(2,5-bis(3-alkylthiophen-2-yl)thieno[3,2-b]thiophene). *Journal of American Chemical Society*, 129:3226–3237, 2007. doi: 10.1021/ja0670714.

[112] Michael L. Chabinyc. X-ray scattering from films of semiconducting polymers. *Polymer Reviews*, 48:463–492, 2008. doi: 10.1080/15583720802231734.

[113] Dag W. Breiby, Oliver Bunk, Jens W. Andreasen, Henrik T. Lemke, and Martin M. Nielsen. Simulating x-ray diffraction of textured films. *Journal of Applied Crystallography*, 41:262–271, 2008. doi: 10.1107/S0021889808001064.

[114] Paolo Samori. *Scanning Probe Microscopies Beyond Imaging: Manipulation of Molecules and Nanostructures*. Wiley-VCH, 2006.

[115] Dror Sarid. *Exploring Scanning Probe Microscopy with Mathematica, Second Edition*. Wiley-VCH, 2007.

[116] Bharat Bhushan and Harald Fuchs. *Applied Scanning Probe Methods*. Springer, 2009.

[117] Benjamin Schmidt-Hansberg, Monamie Sanyal, Michael F.G. Klein, M. Pfaff, S. Jaiser, Alexei Vorobiev, E. Mueller, Alexander Colsmann, P. Scharfer, D. Gerthsen, Uli Lemmer, Esther Barrena, and Wilhelm Schabel. Moving through the phase diagram: morphology formation in solution cast polymer-fullerene-blend films for organic solar cells. submitted to Advanced Materials, 2010.

[118] Benjamin Schmidt-Hansberg, Michael F.G. Klein, K. Peters, Felix Buss, J. Pfeifer, S. Walheim, Alexander Colsmann, Uli Lemmer, P. Scharfer, and W. Schabel. In

situ monitoring the drying kinetics of knife coated polymer-fullerene films for organic solar cells. *Journal of Applied Physics*, 106:124501–124507, 2009. doi: 10.1063/1.3270402.

[119] Masafumi Fukuto, Oleg Gang, Kyle J. Alvine, and Peter S. Pershan. Capillary wave fluctuations and intrinsic widths of coupled fluid-fluid interfaces: An x-ray scattering study of a wetting film on bulk liquid. *Physical Review E*, 74:031607–031625, 2006. doi: 10.1103/PhysRevE.74.031607.

[120] J.M. Napoles-Duarte, Marisol Reyes-Reyes, J.L. Ricardo-Chavez, R. Garibay-Alonso, and Roman Lopez-Sandoval. Effect of packing on the cohesive and electronic properties of methanofullerene crystals. *Physical Review B*, 78:035425–1–7, 2008. doi: 10.1103/PhysRevB.78.035425.

[121] X. Yang, J.K.J. van Duren, M.T. Rispens, J.C. Hummelen, R.A.J. Janssen, M.A.J. Michels, and J. Loos. Crystalline organization of a methanofullerene as used for plastic solar-cell applications. *Advanced Materials*, 16:802–806, 2004. doi: 10.1002/adma.200306372.

[122] R. Joseph Kline, Michael D. McGehee, and Michael F. Toney. Highly oriented crystals at the buried interface in polythiophene thin–film transistors. *Nature Materials*, 5:222–228, 2006. doi: 10.1038/nmat1590.

[123] T. J. Prosa, M.J. Winokur, and R. D. McCullough. Evidence of a novel side chain structure in regioregular poly(3-alkylthiophenes). *Macromolecules*, 29:3654–3656, 1996.

[124] Navaphun Kayunkid, Sureeporn Uttiya, and Martin Brinkmann. Structural model of regioregular poly(3–hexylthiophene) obtained by electron diffraction analysis. *Macromolecules*, 43:4961–4967, 2010. doi: 10.1021/ma100551m.

[125] Ching Lin, En-Yung Lin, and Feng-Yu Tsai. Enhanced thermal stability and efficiency of polymer bulk-heterojunction solar cells by low-temperature drying of the active layer. *Advanced Functional Materials*, 20:834–839, 2010. doi: 10.1002/adfm.200901807.

[126] X.M. Jiang, R. Oesterbacka, O. Korovyanko, C.P. An, B. Horovitz, R.A.J. Janssen, and Z.V. Vardeny. Spectroscopic studies of photoexcitations in regioregular and regiorandom polythiophene films. *Advanced Functional Materials*, 12:587–597, 2002. doi: 10.1002/1616-3028(20020916)12.

[127] Mariano Campoy-Quiles, Yoshihiro Kanai, Ahmed El-Basaty, Heisuke Sakai, and Hideyuki Murata. Ternary mixing: A simple method to tailor the morphology of

organic solar cells. *Organic Electronics*, 10:1120–1132, 2009. doi: 10.1016/j.orgel.2009.05.028.

[128] Jeffrey Peet, Michelle L. Senatore, and Guillermo L. Bazan. The role of processing in the fabrication and optimization of plastic solar cells. *Advanced Materials*, 21: 1521–1527, 2009. doi: 10.1002/adma.200802559.

[129] A. Baumann, J. Lorrmann, C. Deibel, and V. Dyakonov. Bipolar charge transport in poly(3-hexylthiophene)/methanofullerene blends: A ratio dependent study. *Applied Physics Letters*, 93:252104–1–3, 2008. doi: 10.1063/1.3055608.

[130] T. J. Prosa, M.J. Winokur, Jeff Moulton, Paul Smith, and A.J. Heeger. X-ray structural studies of poly(3-alkylthiophenes): an example of an inverse comb. *Macromolecules*, 25:4364–4372, 1992. doi: 10.1021/ma00043a019.

[131] Mariano Campoy-Quiles, Toby Ferenczi, Tiziano Agostinelli, Pablo G. Etchegoin, Youngkyoo Kim, Thomas D. Anthopoulos, Paul N. Stavrinou, Donal D. C. Bradley, and Jenny Nelson. Morphology evolution via self-organization and lateral and vertical diffusion in polymer:fullerene solar cell blends. *Nature Materials*, 7:158–164, 2008. doi: 10.1038/nmat2102.

[132] Youngkyoo Kim, Steffan Cook, Stelios A. Choulis, Jenny Nelson, James R. Durrant, and Donal D. C. Bradley. Organic photovoltaic devices based on blends of regioregular poly(3-hexylthiophene) and poly(9,9-dioctylfluorene-co-benzothiadiazole). *Chemistry of Materials*, 16:4812–4818, 2004. doi: 10.1021/cm049585c.

[133] Peter J. Brown, D. Steve Thomas, Anna Koehler, Joanne S. Wilson, Ji-Seon Kim, Catherine M. Ramsdale, Henning Sirringhaus, and Richard H. Friend. Effect of interchain interactions on the absorption and emission of poly(3-hexylthiophene). *Physical Review B*, 67:064203–064218, 2003. doi: 10.1103/PhysRevB.67.064203.

[134] Minze T. Rispens, Auke Meetsma, Roman Rittberger, Christoph J. Brabec, Niyazi Serdar Sariciftci, and Jan C. Hummelen. Influence of the solvent on the crystal structure of pcbm and the efficiency of mdmo-ppv: Pcbm 'plastic' solar cells. *Chemical Communications*, 47:2116–2118, 2003. doi: 10.1039/b305988j.

[135] Xiaoniu Yang, Alexander Alexeev, Matthias A. J. Michels, and Joachim Loos. Effect of spatial confinement on the morphology evolution of thin poly(p-phenylenevinylene)/methanofullerene composite films. *Macromolecules*, 38: 4289–4295, 2005. doi: 10.1021/ma047589x.

[136] Svetlana S. van Bavel, Maik Baerenklau, Gijsbertus de With, Harald Hoppe, and Joachim Loos. P3ht/pcbm bulk heterojunction solar cells: Impact of blend composition and 3d morphology on device performance. *Advanced Functional Materials*, 20:1458–1463, 2010. doi: 10.1002/adfm.200902247.

[137] Harald Hoppe and Niyazi Serdar Sariciftci. Morphology of polymer/fullerene bulk heterojunction solar cells. *Journal of Materials Chemistry*, 16:45–61, 2006. doi: 10.1039/6510618b.

[138] Roman Lopez-Sandoval, J. Arenas-Alatorre, R. Garibay-Alonso, David L. Caroll, and A. Lastras-Martinez. Methanofullerene elongated nanostructure formation for enhanced organic solar cells. *Thin Solid Films*, 516:52–57, 2007. doi: 10.1016/j.tsf.2007.04.166.

[139] Koen Vandewal, Abay Gadisa, Wibren D. Oosterbaan, Sabine Bertho, Fateme Banishoeib, Ineke Van Severen, Laurence Lutsen, Thomas J. Cleij, Dirk Vanderzande, and Jean V. Manca. The relation between open-circuit voltage and the onset of photocurrent generation by charge-transfer absorption in polymer : Fullerene bulk heterojunction solar cells. *Advanced Functional Materials*, 18:2064–2070, 2008. doi: 10.1002/adfm.200800056.

[140] Koen Vandewal, Abay Gadisa, Wibren D. Oosterbaan, Sabine Bertho, Fateme Banishoeib, Ineke Van Severen, Laurence Lutsen, Thomas J. Cleij, Dirk Vanderzande, and Jean V. Manca. The relation between open-circuit voltage and the onset of photocurrent generation by charge-transfer absorption in polymer : Fullerene bulk heterojunction solar cells. *Advanced Functional Materials*, 18:2064–2070, 2008. doi: 10.1002/adfm.200800056.

[141] Dirk Veldman, Stefan C. J. Meskers, and René A. J. Janssen. The energy of charge-transfer states in electron donor-acceptor blends: Insight into the energy losses in organic solar cells. *Advanced Functional Materials*, 19:1939–1948, 2009. doi: 10.1002/adfm.200900090.

[142] Markus Hallermann, Ilka Kriegel, Enrico Da Como, Josef M. Berger, Elizabeth von Hauff, and Jochen Feldmann. Charge transfer excitons in polymer/fullerene blends: The role of morphology and polymer chain conformation. *Advanced Functional Materials*, 19:3662–3668, 2009. doi: 10.1002/adfm.200901398.

[143] Youngkyoo Kim, Stelios A. Choulis, Jenny Nelson, Donal D. C. Bradley, Steffan Cook, and James R. Durrant. Device annealing effect in organic solar cells with blends of regioregular poly(3-hexylthiophene) and soluble fullerene. *Applied Physics Letters*, 86:063502–063504, 2005. doi: 10.1063/1.1861123.

[144] Youngkyoo Kim, Jenny Nelson, Tong Zhang, Steffan Cook, James R. Durrant, Hwajeong Kim, Jiho Park, Minjung Shin, Sungho Nam, Martin Heeney, Iain McCulloch, Chang-Sik Ha, and Donal D.C. Bradley. Distorted asymmetric cubic nanostructure of soluble fullerene crystals in efficient polymer:fullerene solar cells. *ACS Nano*, 3:2557–2562, 2009. doi: 10.1021/nn900798m.

[145] Hwajeong Kim, Minjung Shin, and Youngkyoo Kim. Distinct annealing temperature in polymer:fullerene:polymer ternary blend solar cells. *The Journal of Physical Chemistry C*, 113:1620–1623, 2009. doi: 10.1021/jp809589n.

[146] Jae Kwan Lee, Wan Li Ma, Christoph J. Brabec, Jonathan Yuen, Ji Sun Moon, Jin Young Kim, Kwanghee Lee, Guillermo C. Bazan, and Alan J. Heeger. Processing additives for improved efficiency from bulk heterojunction solar cells. *Journal of American Chemical Society*, 130:3619–3623, 2008. doi: 10.1021/ja710079w.

[147] In-Wook Hwang, Shinuk Cho, Jin Young Kim, Kwanghee Lee, Nelson E. Coates, Daniel Moses, and Alan J. Heeger. Carrier generation and transport in bulk heterojunction films processed with 1,8-octanedithiol as a processing additive. *Journal of Applied Physics*, 104:033706–033714, 2008. doi: 10.1063/1.2951957.

[148] Hsiang-Yu Chen, Hoichang Yang, Guanwen Yang, Srinivas Sista, Ruben Zadoyan, Gang Li, and Yang Yang. Fast-grown interpenetrating network in poly(3-hexylthiophene): Methanofullerenes solar cells processed with additive. *Journal of Physical Chemistry C*, 113:7946–7953, 2009. doi: 10.1021/jp810798z.

[149] Monamie Sanyal, Benjamin Schmidt-Hansberg, Carmen Munuera, Felix Buss, Alexei Vorobiev, Wilhelm Schabel, Helmut Dosch, and Esther Barrena. Real–time investigation of the crystallisation of photovoltaic polymer-fullerene blend film from solution. in preparation, 2010.

[150] Monamie Sanyal, Benjamin Schmidt-Hansberg, Michael F.G. Klein, Alexander Colsmann, Carmen Munuera, Alexei Vorobiev, Uli Lemmer, Wilhelm Schabel, Helmut Dosch, and Esther Barrena. In–situ x–ray study of drying temperature influence on the structural evolution of bulk heterojunction polymer–fullerene solar cells processed by doctor–blading. submitted to Advanced Materials, 2010.

[151] Monamie Sanyal, Benjamin Schmidt-Hansberg, Carmen Munuera, Alexei Vorobiev, Wilhelm Schabel, Helmut Dosch, and Esther Barrena. Effect of composition ratio of polymer/fullerene blends on microstructure evolution during film solidification investigated in real–time by x–ray diffraction. in preparation, 2010.

List of Figures

List of Publications

1. Monamie Sanyal, Benjamin Schmidt-Hansberg, Michael F.G. Klein, Alexander Colsmann, Carmen Munuera, Alexei Vorobiev, Uli Lemmer, Wilhelm Schabel, Helmut Dosch, and Esther Barrena. In–situ x–ray study of drying temperature influence on the structural evolution of bulk heterojunction polymer–fullerene solar cells processed by doctor–blading. *Advanced Energy Materials*, DOI: 10.1002/ aenm.201100007 (2011)

2. Monamie Sanyal, Benjamin Schmidt-Hansberg, Carmen Munuera, Alexei Vorobiev, Wilhelm Schabel, Helmut Dosch and Esther Barrena. Effect of composition ratio of polymer/fullerene blends on microstructure evolution during film solidification investigated in real–time by x–ray diffraction. *Macromolecules*, DOI: 10.1021/ ma2000338 (2011)

3. Monamie Sanyal, Benjamin Schmidt-Hansberg, Carmen Munuera, Felix Buss, Alexei Vorobiev, Wilhelm Schabel, Helmut Dosch and Esther Barrena. Real–time investigation of the crystallisation of photovoltaic polymer-fullerene blend film from solution. *in preparation*

4. Benjamin Schmidt-Hansberg, Monamie Sanyal, Michael F.G. Klein, M. Pfaff, S. Jaiser, Alexei Vorobiev, E. Müller, Alexander Colsmann, P. Scharfer, D. Gerthsen, Uli Lemmer, Esther Barrena, Wilhelm Schabel. Moving through the phase diagram: morphology formation in solution cast polymer-fullerene-blend films for organic solar cells. *submitted for publication*

5. Benjamin Schmidt-Hansberg, Monamie Sanyal, Michael F.G. Klein, Alexander Colsmann, Uli Lemmer, Esther Barrena, Wilhelm Schabel. Evaluation of non-halogenated solvent mixtures for large area fabrication of polymer/fullerene solar cells. *in preparation*

6. Felix Pasker, Michael Klein, Monamie Sanyal, Esther Barrena, Uli Lemmer and Sigurd Höger. Photovoltaic response to structural modifications on a series of conjugated polymers based on 2-aryl-2H-benzotriazoles. *submitted for publication*

List of Acronyms

Acronym	**Explanation**
AFM	Atomic Force Microscope
DCB	1,2–dichlorobenzene
GIXD	Grazing Incidence X–ray Scattering
HOMO	Highest Occupied Molecular Orbitals
ITO	Indium Tin Oxide
KPM	Kelvin Probe Microscope
LUMO	Lowest Unoccupied Molecular Orbitals
MAR–CCD	Charge Coupled Device (CCD) made by MARRESEARCH
OMBD	Organic Molecular Beam Deposition
P3HT	poly(3–hexylthiophene)
PCBM	[6,6]–phenyl–C_{61}–butyric–acid–methyl–ester
PEDOT	poly–(3,4–ethylenedioxythiophene)
PSS	poly–(styrenesulfonate)
UHV	Ultra High Vacuum